From Micro to Nano: Downsizing Self-Assembling Supramolecular Hybrid Gel Beads from the Micrometre to the Nanometre Scale for Possible Biomedical Applications.

Jordan Oliver Hill

Master of Science

University of York

Chemistry

December 2020

Abstract: The purpose of the study reported within this thesis was to fabricate multicomponent gel beads consisting of the polymer gel calcium alginate and the supramolecular gel DBS-$CONHNH_2$. This study built upon previous work in the Smith group wherein beads on the micrometre scale had been fabricated. Here, nano-scale beads are fabricated and reported. In order to achieve this, multiple combinations of parameters were tested in the same general method in order to further understand how each parameter (temperature, oil phase, pH, volume, etc.) affects the size of the beads achieved. Under certain parameters, beads below the upper injectable limit of 200 nm were produced, a significant step which opens up the possibility for biomedical applications of these beads. The beads were analysed via dynamic light scattering (DLS) and electron microscopy in order to attain measurements for size, whilst infrared spectroscopy (IR) and nuclear magnetic resonance (NMR) were used to ascertain composition and yield. Following the downsizing of these beads, magnetic iron oxide nanoparticles were introduced to the procedure with the aim of fabricating beads which will exhibit attraction to an applied magnetic field. By introducing this property, it is hoped that directed drug delivery may be possible in the future, with beads being administered intravenously and subsequently being directed to a target site under the influence of an applied magnetic field. Additional work was also conducted to investigate the effect of metal salts – specifically ferric and cupric chloride – on DBS-$CONHNH_2$. The formation of nanoparticles was observed under electron microscopy, with some iron oxide species being formed in the case of ferric chloride.

Table of Contents

List of Figures

Acknowledgements

The author acknowledges that the assistance and teaching of multiple individuals helped to make this research possible. In particular, gratitude is extended to Professor David K. Smith, the project supervisor whose ideas and suggestions were exceedingly helpful throughout the project; Doctor Carmen Piras, who provided regular assistance and training in methodology and instruments; Doctor Buthaina Albanyan, who provided training in DLS; Anna Patterson, who provided training in rheology and was always on hand to answer any one of a multitude of questions; The remaining members of the DKS group who helped to make the time spent in the lab as enjoyable as it was.

Additionally, Doctors Meg Stark and Karen Hodgkinson, who provided the electron microscopy service for all samples produced are thanked tremendously for their aid.

The contribution of Doctor David Morgan at The University of Cardiff is recognised for running the XPS service and providing analysis of the samples.

Doctor Jamie Gould is thanked for providing access to, and running a sample on, PXRD.

Declaration

I declare that this thesis is a presentation of original work and I am the sole author. This work has not previously been presented for an award at this, or any other, University. All sources are acknowledged as References.

1. Introduction

1.1. An introduction to gels

Gels are commonplace in everyday life, from shampoos and shower gels to contact lenses and thermal pastes, this class of materials is perhaps the most used in modern life. In chemistry, a gel may be defined as a colloidal 'solid-like' system which contains solvent in its pores as a 'liquid-like' phase. This 'liquid-like' phase may be water in the case of hydrogels,[1] organic solvent in organogels,[2] or air in xerogels/aerogels.[3] In hydrogels, hydrophilic groups enable the absorption and entrapment of water (see Figure 1), swelling the gel until it contains up to 99% water by weight. Gels may be produced naturally by both plants and animals, such as aloe gel produced by the aloe vera plant, mucus secreted by mucous glands, or the cartilage found in a majority of fauna. Alternatively, they may be produced synthetically from a wide range of starting molecules. This class of materials is ubiquitous, spanning areas such as pharmaceuticals,[4] cosmetics, electronics,[5] and the food industry.[6] Gels are formed through a process termed 'gelation', which may occur through the formation of chemical bonds (polymer gel) or through self-assembly driven by supramolecular interactions. Typically, polymer gels are produced from gelators with higher molecular weight, whereas supramolecular gels are typically formed from low molecular weight gelators (LMWGs). Polymer gels, owing to the nature of intermolecular interactions, are usually stiffer and less affected by external stimuli than their supramolecular counterparts.

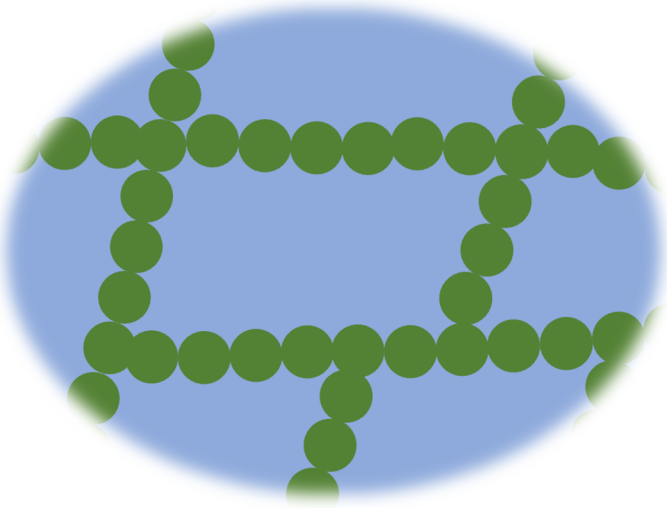

Figure 1: Diagram of the structure of a gel (green) with solvent (blue) entrapped in its pores.

Historically, naturally occurring hydrogels may have been used pharmaceutically by humans since at least 1550 BC, when medicinal uses for aloe vera were described in the Ebers Papyrus. Scientifically, hydrogels were described by Bemmelen[7] in 1896, where this specific term was first used to describe a colloidal gel formed by inorganic salts. This field of research was largely neglected until Wichterle and Lim[8] published their 1960 paper describing soft contact lenses formed from the hydrogel poly(2-hydroxyethyl methacrylate). Following this, a growth in interest around these materials was observed although routes of exploration were mainly focussed on ophthalmological applications. For example, Refojo *et al.*[9] explored the use of dehydrated glyceryl methacrylate as a possible vitreous implant to improve the outcome of cases of retinal detachment. It was not until 1982 that hydrogels were suggested as drug delivery vehicles, when Mueller *et al.*[10] described the uptake and controlled release of water-soluble drugs by poly(2-hydroxyethyl methacrylate) gel beads. This was followed by a marked

boom in research into hydrogels as drug delivery vehicles, with a vast array of gelators being explored, both polymeric and supramolecular in nature.

Polymeric gels are typically stiffer than supramolecular gels, owing to the covalent or ionic bonding present between gelator molecules. In addition, these gels tend to be unresponsive to external stimuli such as changes in temperature or pH.[11] Polymer gels are usually formed from the gelation of higher molecular weight gelators (see Figure 2), such as poly(vinyl alcohol) (PVA),[12] cellulose,[13] or poly(ethylene glycol) (PEG),[14] and are broadly non-toxic and biocompatible, thus lending themselves to biological applications. Poly(ethylene glycol), although not always a gel, was first proposed for use in drug delivery systems by Yoshida *et al.*[15] when they used delivery vehicles containing PEG for testosterone transport in rats. It was shown that the presence of PEG increased testosterone levels in the rats at a level 3.2 times greater than in the absence of PEG. Senior *et al.*[16] further explored the efficacy of PEG for drug delivery, and it was found that PEG-coated liposomes were cleared from blood circulation at a rate 30% slower than liposomes without a PEG coating, suggesting that the use of PEG would aid sustained drug release. This strategy of adding PEG to drug delivery vehicles has since become known as PEGylation,[17] and is a widely employed strategy for improving drug delivery efficacy. In general, the combination of different polymer gels in one composite gel has become more common as a method to combine properties of two or more gels.[18] PVA, for example, has been combined with chitosan and cellulose by Fan *et al.*[19] to improve the wound healing properties of PVA by imparting the antiseptic properties of chitosan. Alternatively, polymer gels have also been combined with supramolecular gels in order to combine the properties of both of these classes of gel.

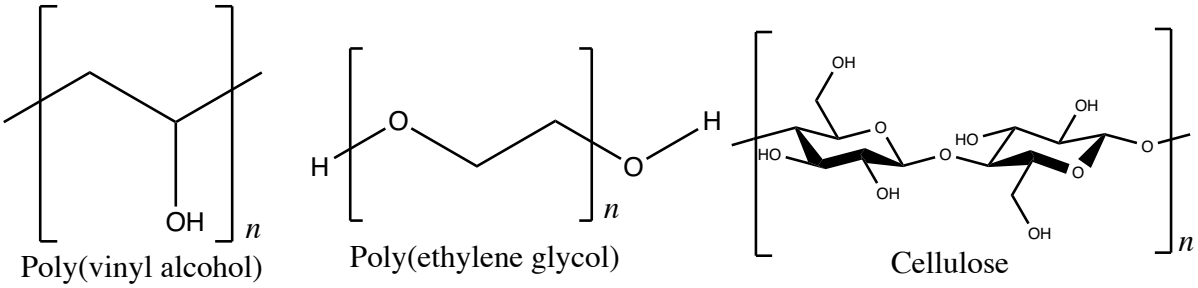

Figure 2: Structures of three different polymer gelators.

Supramolecular gels were first described in 1841,[20] though they were mostly ignored in an academic setting until 1997, when Terech and Weiss[21] published a landmark review on supramolecular organogels and their unique properties. These gels are primarily formed through non-covalent interactions such as van der Waals forces, hydrogen bonding, or π-π stacking between monomeric units.[22] *N,N'*-dibenzoyl-*L*-cystine, for example, self-assembles through π-π stacking interactions between aromatic rings and hydrogen bonding between amide and carboxyl groups.[23] Owing to the inherent weakness and reversibility of these individual forces, supramolecular gels are likely to be less stiff than polymeric gels formed through covalent or ionic bonding. However, these gels are commonly responsive to external stimuli, exhibiting reversible thermally- or pH-triggered gelation.[24] It should be noted that stimuli responsiveness may still be present in chemically linked polymer gels, such as poly(*N*-isopropylacrylamide) (PNIPAAm),[25] but this mainly affects the swelling behaviour in these chemically crosslinked gels and typically does not reverse the gelation as in supramolecular gels and physically linked polymer gels. In a similar fashion to polymer gels, supramolecular

gels are also being explored for biomedical applications. Supramolecular gelators derived from natural materials, such as *N,N'*-dibenzoyl-*L*-cystine, have been explored for drug release by Friggeri *et al.*,[26] who reported that the rate of drug release may be dependent on the strength of the interactions between drug and gelator. This observation was key in the development of supramolecular gels as it provided evidence that different gels could be designed to improve control over drug release *in vivo*. Gelator molecules have since been designed with tailored groups for the control of drug release. Supramolecular hydrogelators based on amino acids,[27] carbohydrates,[28] and nucleosides[29] have all been synthesised (see Figure 3), resulting in the formation of one of the most diverse and versatile classes of materials to date.

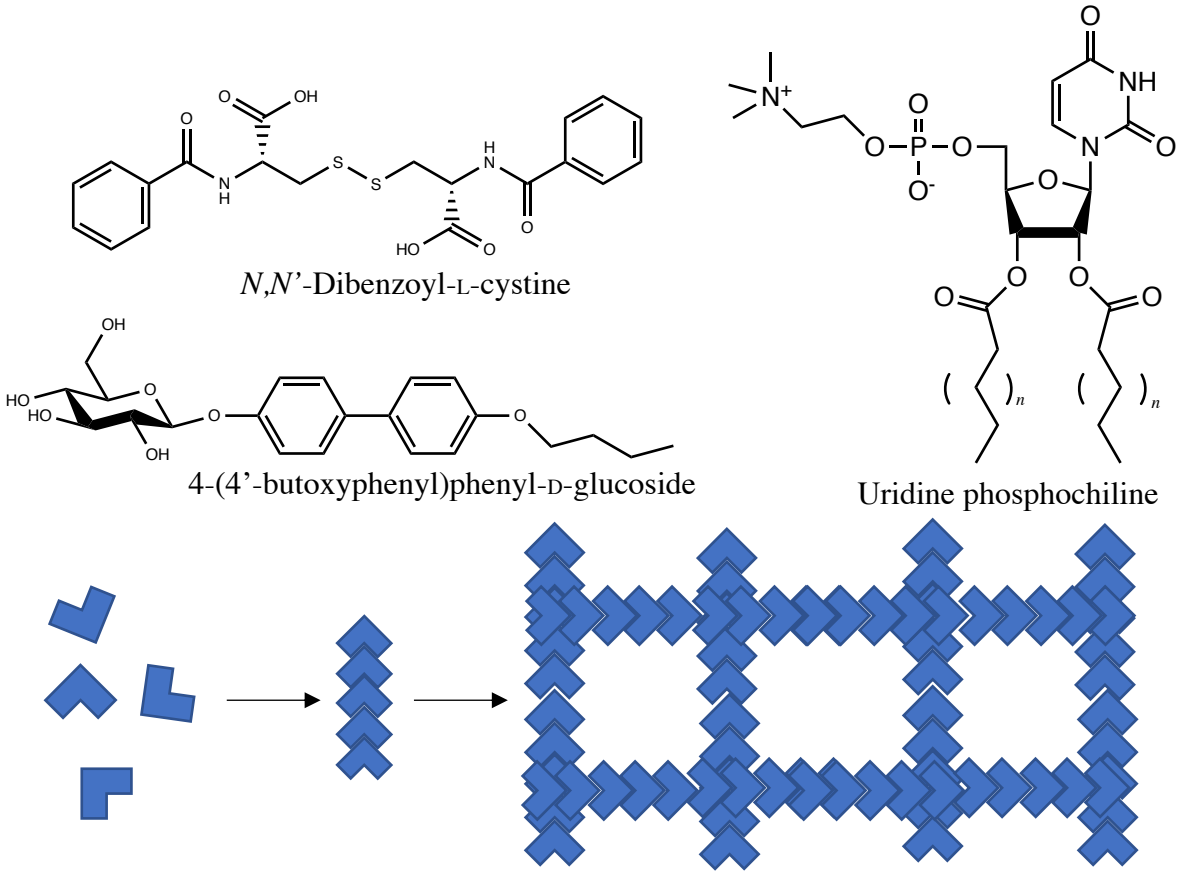

Figure 3: (Upper) Examples of supramolecular gelators. (Lower) Schematic diagram of self-assembly from single molecules to fibrils to gel network.

Evidently, gels as a class of material are vast. They are composed of myriad different compounds, each with different physiochemical properties. Many of these gels are non-toxic, biocompatible, and produced through simple synthetic steps. As a consequence of their properties, they have become widely employed across many different sectors and have shown great promise in the field of biomedicine. The importance of gels cannot, therefore, be understated.

1.2 Alginate gels and drug delivery

Naturally sourced polymer gels may be recovered from a multitude of biota, for example cellulose and agarose may both be isolated from the cell walls of green plants and red seaweed, respectively.[30, 31] Chitosan is produced via the deacetylation of chitin, a natural

polysaccharide which is abundant in marine crustaceans such as shrimp and crabs.[32] These natural polymers, beyond being so common, are biocompatible and non-toxic as a result of their biotic origin. These attributes open up potential applications in pharmaceuticals and medicinal chemistry, with gelators such as chitosan possessing antimicrobial properties as a result of its primary amino groups.[33] One natural hydrogelator which has emerged as a popular option is calcium alginate, the calcium salt of alginic acid.

Alginic acid is a hydrophilic linear polysaccharide which naturally occurs in some bacteria and the walls of brown seaweed, accounting for up to 40 % w/w dry weight of some seaweed species.[34] When hydrated, alginic acid forms a viscous fluid which is responsible for the rigidity of the seaweed. Commercially, this product has found use as a stabiliser in items such as ice creams, preserves, and marshmallows.[35] This compound is a copolymer consisting of repeating units of β-D-mannuronate (M) and α-L-guluronate (G), forming either heterogenous MM or GG blocks, or heterogenous MG units (see Figure 4).[36] Metal salts of alginic acid, such as sodium alginate, are able to form hydrogels in water upon the introduction of a divalent cation such as Ca^{2+} (with the exception of Mg^{2+}). Gelation occurs through coordination about the Ca^{2+} cation by the G units, which propagates along the polymer to form a gel via lateral association of polymeric units, resulting in what is termed the 'egg-box' model.[37] As this gelation occurs purely through the G units of alginate, the G:M ratio determines the stiffness of the hydrogel: a greater G content will result in a stiffer gel. The use of mannuronan C-5 epimerases allows for the design of alginate polymers with desired levels of G through the enzyme-facilitated conversion of M units.[38] Furthermore, alginates high in heterogenous blocks (MG units) are water soluble at low pH, whereas highly homogenous alginates (MM or GG units) are insoluble in the same conditions.[39]

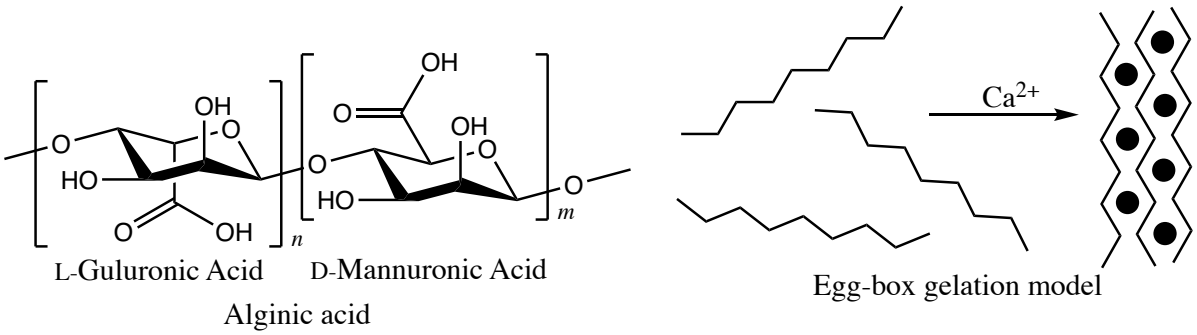

Figure 4: Structure of alginic acid showing both M and G units (left), egg-box gelation model (right).

The biosynthesis of alginic acid in brown algae (see Figure 5) was first investigated by Lin and Hassid.[40] A series of enzymic activities were discovered in *Fucus Gardneri* Silva which are necessary for the synthesis of mannuronan. A biosynthetic pathway was proposed starting with α-D-mannose-1-phosphate which is then converted to guanosine diphosphate (GDP)-D-mannose by the enzyme guanylyltransferase. The enzymatic activity of GDP-D-mannose dehydrogenase then converts this compound to GDP-D-mannuronic acid. The phosphate groups are then removed by glucosyl transferase to yield mannuronan, which is then acetylated and subsequently epimerised by acetyl transferase and C-5-epimerase respectively to yield alginic acid. This pathway has also been observed in *Azotobacter vinelandii* by Pindar and Bucke.[41]

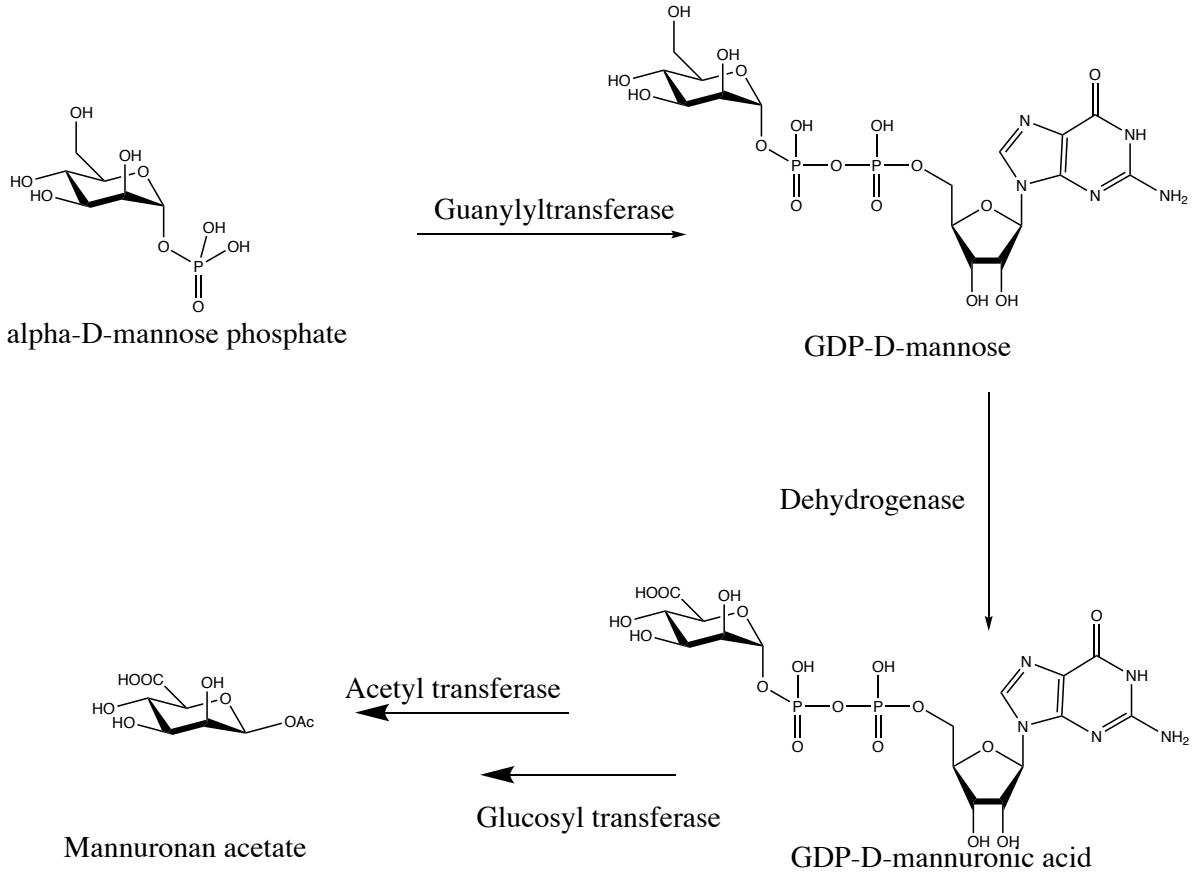

Figure 5: Biosynthetic route for mannuronan acetate. This compound is then epimerised by C-5-epimerase to form Guluronan acetate and subsequently alginic acid.

There are disadvantages associated with alginate being a naturally occurring polymer. The main disadvantage is the presence of unwanted impurities such as polyphenols, which may affect the overall biocompatibility of the gels. This was shown in part by Torres *et al.,*[42] who reported that cell proliferation by purified alginates is greater than that by untreated alginates. The implication of this is that the impurities naturally found within alginates do have an impact on the health of cells and should ideally be removed prior to any biomedical application.

Biological applications for alginate gels have been proposed since at least 1950, when Slavin[43] described the use of calcium alginate as an 'antigen depot' for the slow release of antigens in rabbits, stimulating the prolonged production of antibodies and eliminating the need for repeated antigen injections. After this report, however, calcium alginate was – like most gels – largely ignored. This was in part due to Slavin's observation that the gel was not injectable and required gelation *in vivo* via intraperitoneal injection of sodium alginate and calcium chloride. For the following two decades, calcium alginate was mostly used for the immobilisation and study of cells, having suitable physiochemical properties for this application, as reported by Kierstan and Bucke[44], and Cheetham *et al*.[45] In terms of biomedical applications, alginate gel was generally investigated as a wound dressing for cutaneous administration. Gilchrist *et al.*[46] reported that Sorbsan, an alginate dressing, is effective as a haemostatic and at mitigating microbial infection. This haemostatic property arises from ion exchange between calcium alginate and free sodium in the fluid from the wound. The resultant free calcium aids in the clotting of blood. Separately, Moroz *et al.*[47] investigated

alginate dressings loaded with antibiotics for the sterilisation of pharmaceutical packaging, reporting significant antimicrobial effects of drug-loaded alginate film.

It was not until 1985 that calcium alginate was proposed as a drug delivery system, when Badwan *et al.*[48] reported the uptake and release of the antibiotic sulfamethoxazole by calcium alginate beads (see Figure 6). This bead formulation had the potential to overcome the problems encountered with alginate as an injectable system. By forming discrete beads, the overall size of the gel is reduced, while the physiochemical characteristics are retained. The beads formed in this study were 1.25 mm in diameter, which is too large for injection, but was a marked improvement on the first report of alginate beads by Seely *et al*.[49] where beads 4 mm in diameter were formed. The method for bead formation generally followed the same basic principle wherein sodium alginate solution is added dropwise to a solution of calcium chloride, forming beads upon contact.

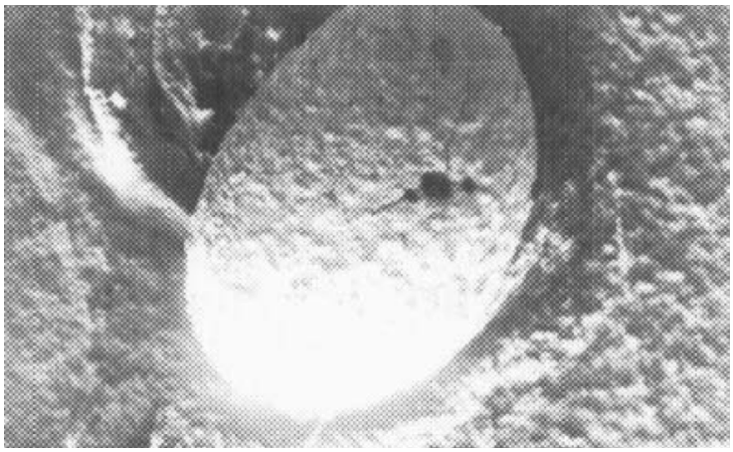

Figure 6: SEM image of the alginate bead formulated by Badwan et al. Image reproduced from Ref. 48.

The advent of alginate beads as potential drug delivery systems did not, however, result in an immediate inundation of injectable alginate formulations. For the most part, alginate was used in oral dosage forms, such as a binder or dispersant in tablets.[50] Oral administration does, of course, have its advantages such as increased stability of formulations, with tablets being more stable than injectable suspensions, and improved patient willingness.[51] Furthermore, using alginate beads these beads introduces buoyancy to the formulation, improving drug release in the stomach, mitigating issues with poor bioavailability at other areas of the digestive tract. Nakamura *et al,*.[52] for example, loaded calcium alginate gel beads with theophylline, a phosphodiesterase inhibitor, for possible oral administration. The use of alginate beads for oral drug delivery may also aid in the pharmacokinetics of drugs, with Murata *et al*.[53] reporting prolonged delivery of the antibiotic metronidazole and improved gastroretention times, suggesting that the use of these beads will aid in improving drug efficacy. Calcium alginate gel was also used as a coating for amiprilose hydrochloride tablets by Kaneko *et al.*[54] and found to mask the unpleasant taste of this drug, improving the oral administration process. Other drugs which have been combined with alginate for improved oral delivery include insulin,[55] indomethacin,[56] and irinotecan.[57] Probiotics have also been encapsulated within alginate beads for oral administration, with improvements in viability observed as the bacteria are protected from the acidic pH of the stomach and the saline conditions of the intestine. Mandal *et al*.,[58] for example, reported the improved survival of *Lactobacillus casei* when encapsulated in alginate beads. A more commercial application of

oral formulations of alginate is the antacid Gaviscon.[59] Here, calcium carbonate and sodium alginate are utilised synergistically, with the carbonate neutralising stomach acid before alginate forms a gel by binding to the calcium.

Evidently, calcium alginate gel is a popular option for oral administration of drugs given the multitude of active pharmaceutical ingredients (APIs) which have been incorporated into the gel. The results are largely positive, with improved drug release profiles and efficacy being observed. Similar results were observed with probiotics, including bolstered survival rates of the bacteria. Once oral formulations began to rise in popularity, consideration was given to achieving alginate drug delivery vehicles which are suitable for subcutaneous and intravenous administration. Delivering drugs to a target site via the bloodstream is arguably much more efficient than other routes of administration, bypassing the gastrointestinal tract entirely and minimising drug degradation. However, there may be considerable off-target effects when drugs are administered intravenously and, especially in the case of severely cytotoxic anticancer agents, this can result in serious side effects such as hypertension and cardiotoxicity.[60] These off-target effects are a result of the pharmacokinetics of drugs in the bloodstream – they diffuse throughout the body rather than congregate at a target site. This also results in reduced efficacy and subsequently poor attrition rates with only 11% of novel drug molecules receiving regulatory approval.[61]

By encapsulating drugs within nanoparticle vehicles, their circulation time can be increased, an observation in line with what is seen via oral administration. This effect, however, is of particular importance in the case of intravenous administration. A landmark paper by Maeda *et al*.[62] described the enhanced permeability and retention (EPR) effect, in which large macromolecules are observed to exhibit tumouritropic behaviour and accumulate within solid tumours. This effect may be explained through the defective growth of tumours, resulting in deformities in both the cells and vascular structure, in addition to poor lymphatic filtration and drainage around the tumour. This means that macromolecular structures are not filtered out of the tumour region and may therefore accumulate. A 100% increase in drug delivery to a tumour site was observed in certain cases.[63] The discovery of the EPR effect has, understandably, resulted in a swathe of research into liposomal and macromolecular drug delivery. However, the EPR effect may not be universally applied across all tumours, and some clinical trials have failed to show improved drug delivery when using a drug carrier compared to the free drug.[64] It is believed that the animal cancer models which may be used to study the EPR effect are more sensitive to EPR than clinical tumours in humans. The effect is likely present in human tumours, but it is not functional as frequently as in animal models. The effect should therefore be invoked on a case-by-case basis.

Calcium alginate gel is a prime candidate for intravenous drug delivery, having been shown to be biocompatible, non-toxic, and effective in prolonging drug release. One barrier to its adoption for this use, however, was the need to reduce the size of alginate beads to an injectable level. Typically, vehicles synthesised for injection are below 200 nm in diameter, such as the PEGylated liposomes developed by Najlah *et al*.[65] for the delivery of disulfiram, or the poloxamer 407 liposomes reported by Paavola *et al*.[66] for ibuprofen delivery. Efforts were therefore needed to improve upon the alginate bead sizes observed by simply adding sodium alginate solution dropwise to calcium chloride solution. Lee *et al*.[67] reported alginate poly-*L*-lysine microparticles fabricated by spraying sodium alginate solution via an air atomiser onto

a bath of calcium chloride solution, with a size range from 80 to 130 μm. The introduction of poly-*L*-lysine has been shown to be effective in further reducing the size of alginate particles, with Rajaonarivony *et al*.[68] reporting the first alginate particles in the nanometre size range through the addition of poly-*L*-lysine to a calcium alginate pregel. The pregel was formed by use of sodium alginate and calcium chloride concentrations below that required for gel formation. The beads in this case were reported to be as small as 250 nm. However, poly-*L*-lysine is unsuitable for biomedical application due to its toxicity and should therefore be avoided. Other methods of bead size reduction should be sought. Chitosan has been explored as a replacement for this molecule by Robinson *et al*.,[69] but this produced larger spheres of around 567 nm in diameter. A modification of this method was reported by Zahoor *et al*.[70] to produce alginate nanoparticles of 236 nm in diameter, and intranasal administration of these particles owing to the mucoadhesive properties of alginate has been explored. Microfluidic routes have also been explored for producing alginate microgels. Zhang *et al*.[71] used microfluidics to explore internal and external gelation methods to form alginate microbeads.

Other methods have been created in attempts to produce alginate beads below 200 nm in diameter. A complexation method, wherein alginate capsules form around oil droplets in a solvent, was shown by Lertsutthiwong *et al*.[72] to result in sizes as low as 263 nm. However, this method will likely only be useful for encapsulating lipophilic compounds, owing to the need of the alginate to complex around an oil droplet. In this case, the oil droplet was turmeric oil at a 1% w/v concentration. A layer-by-layer method was reported by Chen *et al*.,[73] in which an oil-in-water emulsion is formed prior to the addition of a chitosan layer and then an alginate layer. The resultant particle size was 806 nm, though this was for the encapsulation of crystals which were 766 nm in diameter. Much more recently, a double emulsion method was attempted using an oil-in-water-in-oil system by Guo *et al*..[74] In this method, an oil-in-water emulsion containing alginate is formed, and this is then added dropwise to a second oil phase, forming water droplets which contain alginate nanocapsules formed around an oil core. The hydrogel particles here, however, were 7.73 μm in diameter. This set of methods, therefore, can be said to have been largely unsuccessful in producing injectable alginate nanoparticles.

Noticeable improvements were observed when Yi *et al*.[75] reported the use of an emulsion method for the preparation of alginate-bovine serum albumen (BSA) nanoparticles with an average size of 166 $\pm$ 34 nm. The emulsion method, or more accurately the reverse emulsion method, has since become an immensely popular method for the fabrication of alginate nanoparticles below 200 nm in diameter. A reverse emulsion, otherwise called a water-in-oil emulsion, involves the addition of a surfactant to an oil phase (see Figure 7), followed by the addition of gelling components. The surfactant forms surfactant-stabilised water droplets within the oil which are usually in the nanometre size range, and gelation occurs inside these droplets, resulting in nanogels. The radius of water droplets in the oil may be estimated through the use of the equation:

$$R = 3I_s \frac{\phi_W}{\phi_{STotal} - \phi_{SOil}}$$

Where R is the radius, l_s is the thickness of the surfactant layer, ϕ_W is volume fraction of water, ϕ_{STotal} is the volume fraction of the surfactant, ϕ_{SOil} is the volume fraction of surfactant which may be dissolved in oil.[76]

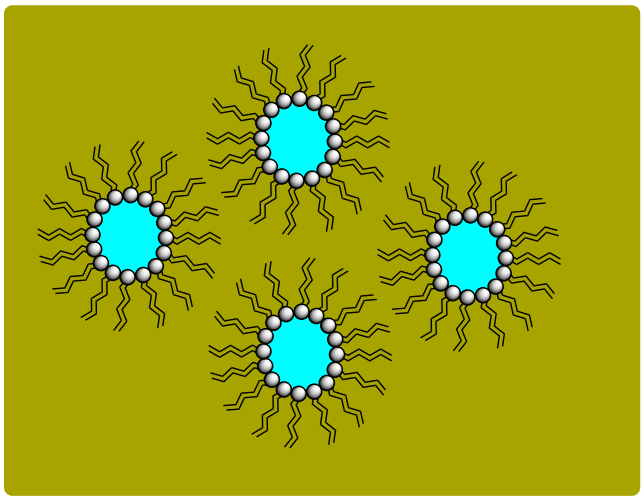

Figure 7: Diagram of a water-in-oil emulsion. Formation and stabilisation of water droplets is facilitated by the nonionic surfactant.

Pure alginate nanogels, however, are less common than hybrid gels. Alginate-chitosan nanoparticles are particularly successful, with You *et al*.[77] reporting an average diameter of 64 nm when gelling alginate around a chitosan nanodroplet core in a reverse emulsion, and Wang *et al*.[78] reporting a nanogel diameter of 136 nm when using oligochitosan and alginate in combination. Reports do exist of pure calcium alginate nanoparticles formed via the reverse emulsion method. You *et al*.[79] reported alginate nanoparticles of 80 nm in diameter formed when using toluene as the oil phase. While this result was promising, toluene is highly toxic and its possible presence in the final product was not discussed. Should any toluene be present in the alginate beads, they would not be suitable for the biomedical purposes proposed in the study. As toluene is slightly soluble in water, it is likely that there may be some residual toluene in the hydrogel. More recently, Machado *et al*.[76] produced alginate nanoparticles with a diameter below 100 nm using decane as the oil phase. In this study, residual decane was suggested to be present in the final product by higher-than-expected integrals for terminal methyl groups in NMR spectroscopic analysis. Given the slight solubility of most oil phases in water, complete avoidance of this contamination may be impossible. Considerations should therefore be taken to mitigate the volume of oil phase in the product.

1.3 Magnetic Nanoparticles and Targeted Drug Delivery in Hydrogels

Having solved the size issue with alginate nanoparticles, intravenous drug delivery applications could now be developed. Several different drugs have already been shown to be effectively loaded into the beads and slowly released over time, with a number of these drugs being anticancer in nature. However, while the EPR effect increases the total portion of a dose which reaches a solid tumour, a median value of only 0.7% of a nanoparticle dose reaches the solid tumour.[80] There is both the scope and necessity for improvement on this statistic. Increasing the efficacy of a drug against a target site will lower the required dose and this in turn will lower off-target effects and the overall cost of treatment. To this end, advancements have been made in improving the targeting of drugs to a specific site.

Drug targeting can either be passive, in which the formulation results in increased accumulation at the target site by increasing circulation time, or active, whereby drug release is made more specific to the target site or nanoparticles are directed towards the site. PEGylation is an example of passive targeting by way of its 'stealth' properties, which delays opsonisation of the nanoparticles and uptake by the mononuclear phagocytic system through the presence of a hydrophilic layer on the nanoparticle.[81] This improves circulation time, and therefore increases accumulation in a solid tumour through the EPR effect. While it does not possess the same 'stealth' abilities as PEG, calcium alginate could be said to possess some passive targeting abilities in that it is slightly anionic, possessing a slightly negative surface charge.[82] This is beneficial as neutral, zwitterionic, and slightly negatively charged nanoparticles have been shown to exhibit favourable pharmacokinetics with increased circulation time in the body.[83] An example of active targeting would be making the nanoparticle responsive to stimuli such as pH. The environment around a tumour is more acidic than in normal tissue as a result of aerobic glycolysis caused by hypoxia in the tumour.[84] Na *et al*.[85] fabricated pH-responsive nanoparticles from pullulan acetate and sulfadimethoxine loaded with doxorubicin which exhibited heightened cytotoxicity at pH 6.8 and low cytotoxicity at pH 7.4. Calcium alginate, however, does not exhibit the 'stealth' abilities of PEG, nor is it stimuli responsive. A different strategy, therefore, is needed to introduce tumour-targeting properties to nanoparticles of this gel. One method which has been explored is the introduction of magnetic nanoparticles, a structure between 1-100 nm in diameter which exhibits attraction to an applied magnetic field.

In general, magnetism arises from the presence of an unpaired electron. Electrons possess a property called spin magnetic moment, μ_s, a fundamental magnetic moment which arises from the spin of the electron. In the case of paired electrons, which must have opposite spins (+1/2, -1/2) as a result of the Pauli exclusion principle, these spin magnetic moments cancel out, and there is a net zero magnetic moment in the material. Where unpaired electrons are present, there is a spin magnetic moment which is not cancelled out and there is a magnetic moment in the material. In a ferromagnet, these magnetic moments align parallel to an applied magnetic field to give a bulk magnetisation. This bulk magnetisation remains in the material after the magnetic field is removed as remnant magnetisation, a property termed magnetic hysteresis. Magnetic hysteresis arises from the presence of magnetic domains in a magnetic material. Magnetic moments are aligned within domains, but not between them. The magnetic moments at the walls of these domains may be changed to align with a magnetic field, thus changing the size and ordering of domains, and energy input is required in the form of a magnetic field to reverse this effect and remove the bulk magnetisation. A magnetic nanoparticle, however, does not possess different magnetic domains due to its small size. Therefore, when an applied magnetic field is removed, magnetic hysteresis is not observed and there is no remnant magnetisation should the nanoparticle be of an adequately small diameter. Iron oxide, nanoparticles, for example, are superparamagnetic at room temperature below 10 nm.[86] This property is termed superparamagnetism, as paramagnets do not exhibit magnetic hysteresis but the magnetic susceptibility, χ, is greater in nanoparticles of ferromagnetic materials than in paramagnetic materials, and it is a vital concept in the biomedical uses of magnetic nanoparticles.

Superparamagnetic nanoparticles may be formed from ferromagnetic materials such as iron oxide, cobalt, and nickel. Cobalt and nickel nanoparticles have been shown to be toxic to

aquatic life by Griffitt *et al*.[87] and should therefore be avoided for biomedical use. Nanoparticles of iron oxide are relatively non-toxic which, in combination with good size-control and ease of synthesis, makes them prime candidates for biomedical use. They have found use as contrast agents in MRI imaging for non-invasive cancer diagnosis, with Kim *et al*.[88] showing that a ferrofluid formed from iron oxide nanoparticles and chitosan result in improved contrast in MRI compared to commercial imaging agents. Magnetic hyperthermia has also been explored as an application for iron oxide nanoparticles, though this remains experimental due to poor control over the final temperature and possible ablation of healthy tissue. Jin *et al*.[89] showed that a heating effect is observed in Fe_3O_4 (magnetite) nanoparticles when they are exposed to an alternating magnetic field. Johannsen *et al*.[90] presented the first clinical application of magnetic hyperthermia for the treatment of prostate cancer, finding that temperatures in the tumour could be raised to 48.5 ℃, more than sufficient to ablate tumour cells. Liao *et al*.[91] functionalised magnetic nanoparticles with alginate gel for hyperthermia treatment, showing a 40% reduction in cancer cell viability after *in vitro* trials.

It is the potential for targeted drug delivery with superparamagnetic nanoparticles which may draw the most attention. In principle, a liposome or nanogel may be fabricated containing magnetic nanoparticles, and a magnetic field may be applied to guide these formulations through the body and direct it toward the target site (see Figure 8).[92] To give rise to movement from a distance, as would be the case with internal nanoparticles and an external magnet, a magnetic field gradient is required as a uniform magnetic field does not produce lateral movement.[93]

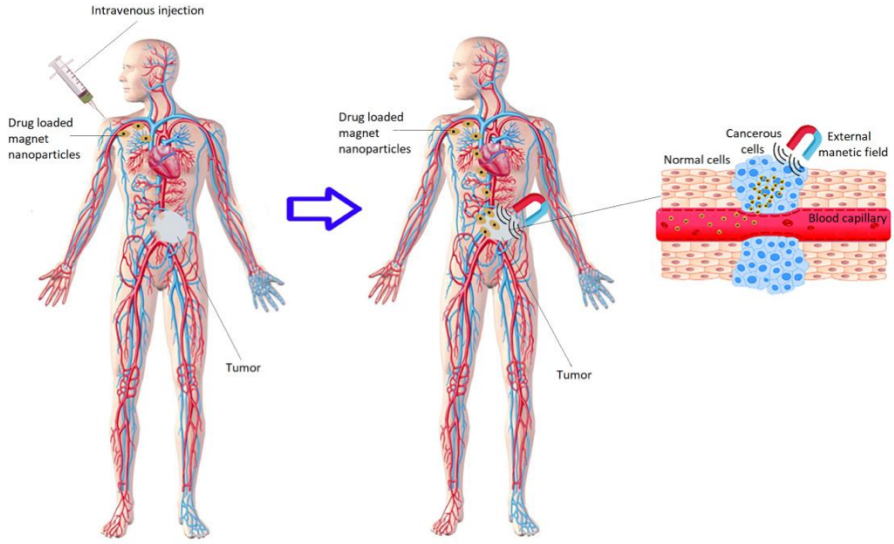

Figure 8: Schematic of targeted drug delivery using magnetic nanoparticles. Image reproduced from Ref. 91.

Several magnetic formulations utilising hydrogels other than alginate have been developed for targeted drug delivery. Nerantzaki *et al*.[94] have recently fabricated doxorubicin-loaded magnetic silica nanoparticles which exhibit cytotoxicity only in the presence of an applied magnetic field, indicating possible dual-action drug delivery with both hyperthermia and drug release inducing cell death within the tumour. Cell viability was reduced up to 50% in this study. Dual-action drug delivery may be vital in overcoming resistances which may be arise in tumours. Both hyperthermia and drug resistance have been observed in cancer cells.[95, 96] Combining these two therapies may increase the efficacy of treatment. Mancarella *et al*.[97]

formed hydrogel functionalised magnetic nanoparticles using layer-by-layer deposition of dextran and poly-*L*-lysine about a magnetite core which were loaded with curcumin. A 70% reduction in cell viability was observed compared to a control. This has since been built upon with alginate gels by Song *et al*.[98] by formulating curcumin-loaded alginate/chitosan nanoparticles in a rather complex layer-by-layer method. The nanoparticles were reported to be up to 189 nm in diameter after the addition of 9 polymer layers, and cell viability was reduced by over 80% in *in vitro* studies. Ciofani *et al*.[99] reported the formation of magnetic alginate nanoparticles through the reverse emulsion method, although these hydrogel nanoparticles were 401 nm in diameter. Importantly, however, internalisation of the nanoparticles by cells was much greater in the presence of a permanent magnet, making this an important proof-of-concept study showing that drug uptake by cells may be improved using these formulations. The reverse emulsion method was demonstrated to be effective in producing magnetic, drug-loaded alginate nanospheres by Chen *et al*..[100] Here, hexane was used as the oil phase and the nanoparticles were shown to have a mean diameter of 185 nm and a circulation time of 15 days.

Naturally, there are toxicity concerns around the introduction of nanoparticles to biological systems. As their use in biomedical applications is relatively novel, minimal data exists on delayed effects, though studies on acute toxicity are promising.[101] Slow release of free nanoparticles from a hydrogel matrix may occur during circulation in the body, and there may be mechanism through which cytotoxicity can occur. Carbon nanoparticles have been shown to accelerate platelet aggregation in the bloodstream of rats, causing thrombosis.[102] Mild toxicity of iron oxide nanoparticles has been observed *in vitro* in human macrophages by Pawelczyk *et al*.,[103] with only 20% cell viability after 7 days of exposure. The concentration of iron within the cells was 34.75 pg per cell. However, much of the possible toxicity of iron oxide nanoparticles appears to be based upon the size of the particle. Most *in vivo* studies, however, do not report any toxicity of iron oxide nanoparticles. Yang *et al*.[104] studied the biodistribution of a range of sizes of iron oxide nanoparticles (10, 20, 30, and 40 nm) and found no acute toxicity, though did note that smaller nanoparticles (10 nm) readily cross the blood-brain barrier to enter the brain. No behavioural changes were observed, suggesting brain function is not affected, but the study was concluded after just 7 days. Nonetheless, a majority of studies do not report any acute toxicity or impairment of normal function following the administration of iron oxide nanoparticles, suggesting they are safe for biomedical use. Moreover, they are likely to be far less cytotoxic than the anticancer agents being delivered within the formulation, and the release over time from the formulation is likely to be too low to cause any unwanted toxicity. Their use in combination with hydrogel formulations for targeted drug delivery should therefore be explored further and the promising results should be built upon.

1.4 Dibenzylidene-D-Sorbitol (DBS)-$CONHNH_2$

Supramolecular hydrogelators have recently emerged as alternatives to polymer gels for drug delivery formulations. Supramolecular interactions are commonplace in nature, from the forces which allow geckos to ‘stick’ to surfaces, to the hydrogen bonding between nucleobases to form the double helix in DNA. Supramolecular gelators, therefore, are mostly derived from natural materials, making them highly biocompatible. The ability to design gelator molecules to specifically tailor interactions has led to the creation of a large library of possible gels. One route of exploration has led to the use of open-chain sugars as a backbone

for gelators, with D-sorbitol – a reduced form of glucose – finding wide employment in this field. One supramolecular gelator based on D-sorbitol which has attracted attention is 1,3:2,4-dibenzylidene-D-sorbitol (DBS) (see Figure 9).

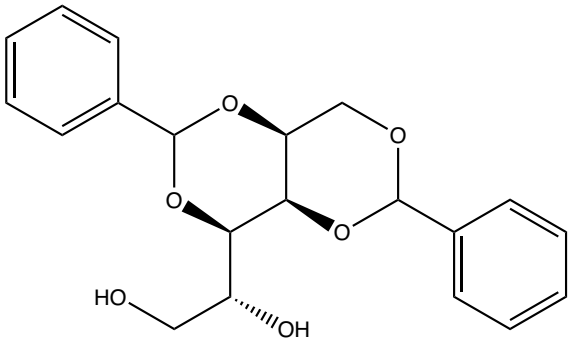

1,3:2,4-Dibenzylidene-d-sorbitol

Figure 9: Structure of DBS, a chiral, amphiphilic 'butterfly' gelator with a D-sorbitol 'backbone' and two benzaldehyde 'wings'.

DBS is one of the earliest supramolecular gelators to be reported in literature, with Meunier[105] first describing the synthesis and gelling properties of this compound in 1891. It is formed via a condensation reaction between D-sorbitol and benzaldehyde in a 1:2 molar ratio under acidic conditions. This molecule has found use in polyolefin plastic compositions, offering improved transparency.[106] It is also the base gel in Rightguard deodorant gel sticks. However, much like a majority of hydrogels, the importance of this material was not realised until decades had passed since its discovery. In 1942, Wolfe *et al*.[107] explored the structure of DBS, characterising the presence of a glycol group and thus narrowing down the exact structure to either 1,2,3,4- or 3,4,5,6- functionalised D-sorbitol. This was built upon in 1944 by Angyal *et al*.,[108] who were able to isolate 2,4-monobenzylidene-D-sorbitol through hydrolysis of DBS with acetic acid in ethanol. The presence of this molecule after hydrolysis confirmed the structure of DBS as 1,3:2,4-dibenzylidene-D-sorbitol. No other isomer was encountered in this study. Following the confirmation of the structure, efforts began to functionalise either the benzaldehyde wings or the sorbitol body to produce derivatives of DBS. Several derivatives were described by Feng *et al*.[109] with *para*-substituted phenyl groups functionalised by methyl-, methoxy-, cyano-, fluoro-, chloro-, or nitro- groups. Raluca *et al*.[110] also exhibited the synthesis of an amino- derivative through the reduction of the nitro group, and subsequent alkylation to form N-alkylated derivatives of DBS. More recently, 3,4-dichloro functionalised phenyl groups in DBS have been synthesised by Li *et al*.[111] Smith and co-workers[112, 113] further expanded on the scope of possible DBS derivatives by first synthesising an ester functionalised DBS (DBS-CO_2Me) , and then both a carboxylic acid functionalised DBS (DBS-COOH) and an acyl hydrazide functionalised DBS (DBS-$CONHNH_2$) (see Figure 10).

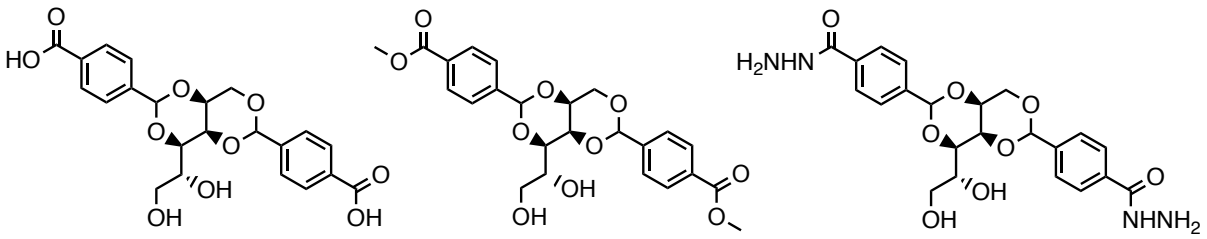

1,3:2,4-Dibenzylidene-D-sorbitol CO_2H | 1,3:2,4-Dibenzylidene-D-sorbitol CO_2Me | 1,3:2,4-Dibenzylidene-D-sorbitol $CONHNH_2$

Figure 10: Structures of three novel DBS derivatives developed by the Smith group.

DBS-CO_2H was shown to be a pH-dependent gelator. In basic pH, the carboxyl group is deprotonated, increasing solvation and forming a solution. In acidic pH, the inverse of this process is observed whereby the carboxyl group is protonated and solvation is decreased. In this case, the molecule self-assembles into a gel. Conversely, DBS-$CONHNH_2$ was found to be pH-independent. This observation suggested that unwanted pH responsiveness may be mitigated in supramolecular gels through the replacement of carboxyl groups with acyl hydrazides. The ability to tailor pH responsiveness in supramolecular gels is an important step towards broadening their applications in biological settings, as well as aiding in their adoption due to the ease of preparation, requiring less extreme gelation conditions.

Initially, potential environmental applications of DBS-$CONHNH_2$ were explored. In the same paper where the synthesis of DBS-$CONHNH_2$ was first described, Smith and co-workers[113] reported that this gelator could selectively absorb dyes from solution depending on the pH. Here, the dyes methylene blue (MB), acid blue 25 (AB25), and naphthol blue black (NBB) were shown to be absorbed to different extents at different pH levels due to their protonation and subsequent differing interactions with the gel. For example, AB25 showed a dye absorption value of 1050 mg g^{-1} at pH 2, but less than 200 mg g^{-1} at pH 12. For MB, the highest observed uptake was 800 mg g^{-1}, which is competitive with the previously reported highest uptake of this dye of 1000 mg g^{-1}.[114] Additionally, the dyes AB25 and NBB were shown to be desorbed from the gel when exposed to a basic NaOH (0.1 M) solution, indicating the potential to reuse the gel multiple times for continuous dye removal.

The selective uptake ability of DBS-$CONHNH_2$ has also been explored with the use of precious metals. Smith and co-workers[115] reported the palladium-scavenging abilities of this gelator. Here, a DBS-$CONHNH_2$/agarose hybrid gel was immersed in a solution of $PdCl_2$ over a period of 3 days. UV-vis spectroscopy measured an uptake of 8 μmmol of palladium, indicative of a 2:1 palladium:DBS ratio in the gel, suggesting that each acyl hydrazide may reduce a single palladium ion. Atomic absorption spectroscopy suggested a superb uptake of palladium, with over 99.97% of palladium from a palladium solution (0.83 mM, 3.6 mL) becoming embedded within the gel. In this process, DBS-$CONHNH_2$ actively reduced palladium(II) to palladium(0) nanoparticles. This palladium-loaded hybrid hydrogel was then shown to be an effective catalyst for a series of Suzuki coupling reactions, reporting yields of up to 100% (see Figure 11). Additionally, no loss of catalytic activity was observed until after the 11th use of the same palladium-loaded hybrid hydrogel. This was later built upon by the same group,[116] with the palladium-loaded gels exhibiting catalysis of Sonogashira coupling with yields as high as 99% reported. The catalytic activity was retained for five consecutive runs. This method removes the requirement for a copper co-catalyst, allowing for less harsh reaction conditions, while also improving the environmental profile of the reaction by allowing it to be performed in more environmentally friendly solvents (EtOH/H_2O). Heck coupling was also explored here, with efficient catalysis observed when using the electron-deficient 4-iodonitrobenzene. In this same study, gold was also explored as a possible catalyst, with the formation of gold nanoparticles in the gel. However, no catalytic activity of gold was observed.

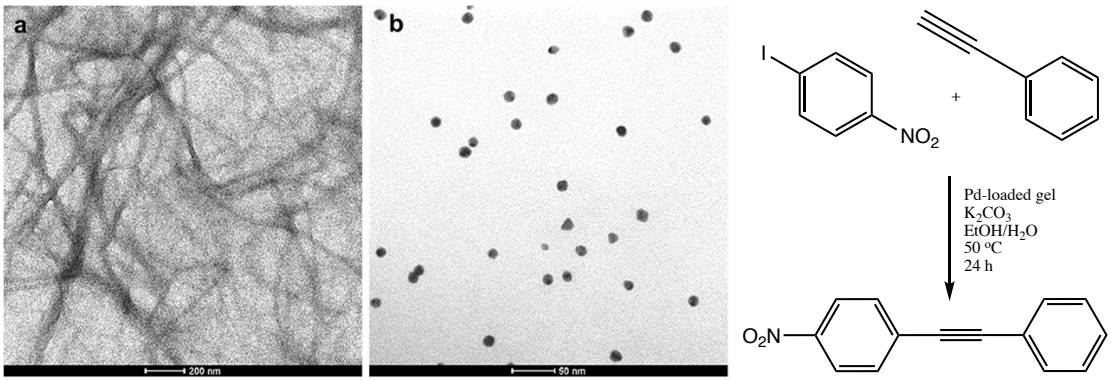

Figure 11: (Left) TEM images of Pd nanoparticles formed in the hybrid hydrogel. Image adapted from Ref. 115. (Right) Sonogashira coupling of 4-iodonitrobenzene and phenylacetylene.

Smith and co-workers[117] have also explored the use of DBS-$CONHNH_2$ as a cell growth medium. Here, DBS-$CONHNH_2$ was combined with the polymer gel agarose, the biopolymer heparin, and heparin-binding C_{16}-DAPMA micelles. Promising cell growth was observed at lower (25 μg) concentrations of heparin, with an increase in metabolic activity of the cells over the course of 7 days. A cell migration assay confirmed that cells were adhering to the surface of DBS-$CONHNH_2$. Additionally, cell growth was observed on pure DBS-$CONHNH_2$ whilst none was observed on agarose, indicating that the cell adhesion and growth is purely due to the presence of DBS-$CONHNH_2$. Agarose, however, provides DBS-$CONHNH_2$ with the required stiffness to act as a cell growth scaffold.

The reactivity of the acyl hydrazide functional groups on the phenyl wings of DBS-$CONHNH_2$ has also been explored. Smith and co-workers[118] further reacted these peripheral groups with the aldehydes vanillin, benzaldehyde, cinnamaldehyde, furfural, hexanal, and butanal, reporting that the gel structure was not disrupted and all hydrogels remained stable upon the formation of acylhydrazones. This work could provide the foundation for further functionalisation of DBS-$CONHNH_2$ and exploration of more applications for this unique gelator.

One further possible application of DBS-$CONHNH_2$ is in the realm of drug delivery. The gelator's previously explored tendency to interact and uptake dye molecules at a certain pH before releasing them at another may have the potential to be exploited with pharmaceuticals. To this end, Smith and co-workers[119] explored the pH-mediated release of three anti-inflammatory drugs from DBS-$CONHNH_2$: mesalazine (MSZ), naproxen (NPX), and ibuprofen (IBU). Initially, only MSZ could be loaded into the gel with the other two showing poor loading due to their hydrophobicity. This barrier was bypassed by mixing dry powder of the gelator and drug at a 1:1 molar ratio and then forming the gel. At 2:1 drug:gel molar ratio, excess drug precipitated out, indicating interaction between the two molecules interact similar to that observed with dyes. pH-mediated release was observed with NPX, with 33% of the loaded drug released over 24 hours at pH 7, compared to 100% released over the same time period at pH 8. This would make this formulation suitable for oral delivery, as the gel would pass through the stomach before reaching the intestine at pH 8 and releasing the drug. This is specifically important in the case of NPX, which has been shown to cause stomach ulcers.[120]

This work was then built upon by the same group.[121] In this study, DBS-$CONHNH_2$ was used in conjunction with PEG dimethacrylate (PEGDM) to form a hybrid gel. PEGDM was introduced to enhance the mechanical stiffness of the supramolecular DBS-$CONHNH_2$. PEGDM is a photo-activated hydrogel,[122] enabling the photo-patterning of this hybrid hydrogel. The hybrid hydrogel was prepared by adding PEGDM and a photoinitiator (2-hydroxy-4'-(2-hydroxyethoxy)-2-methylpropiophenone) on top of a NPX-loaded DBS-$CONHNH_2$ hydrogel prepared as in the previous report, followed by photopolymerisation. These gels were found to be free-standing and able to be handled, unlike pure DBS-$CONHNH_2$. Drug release at pH 7 and 8 was found to be 80-90% over a period of 24 hours. At pH 4, this was reduced to 25-30% over the same time period.

Recently, the potential for multicomponent gel formulations for DBS-$CONHNH_2$ and calcium alginate for drug delivery has been explored. Smith and co-workers[123] have described the fabrication of self-assembled supramolecular hybrid gel beads with a core-shell structure (see Figure 12). Here, the LMWG phase is contained entirely within a polymer gel sphere, the first formulation of its kind. Here, a hot mixture of DBS-$CONHNH_2$ and sodium alginate was added dropwise to a calcium chloride solution, and beads as small as 750 μm were formed with over 90% incorporation of DBS-$CONHNH_2$ into the core of the bead. The core-shell structure was confirmed through optical microscopy. These gels were then loaded with palladium in a similar fashion to the DBS-$CONHNH_2$/agarose hybrid gels. The loading was significantly poorer in the case of the core-shell beads, with only 33% of palladium uptake observed compared to the DBS-$CONHNH_2$/agarose hybrid gel. This indicates interaction between the LMWG and alginate which may limit interactions with added molecules of interest and may have implications for drug loading in a pharmaceutical application. The palladium-loaded core-shell hybrid gel beads were then used for the catalysis of Suzuki coupling reactions, exhibiting similar catalytic performance as the palladium-loaded DBS-$CONHNH_2$/agarose hybrid gel, with full conversion observed in the first two reactions. However, this catalytic activity drops much faster than observed in the previous gel formulation, with only consecutive reactions being possible compared to eleven. Regardless, this was a promising initial study into the formulation and application of DBS-$CONHNH_2$/alginate core-shell beads.

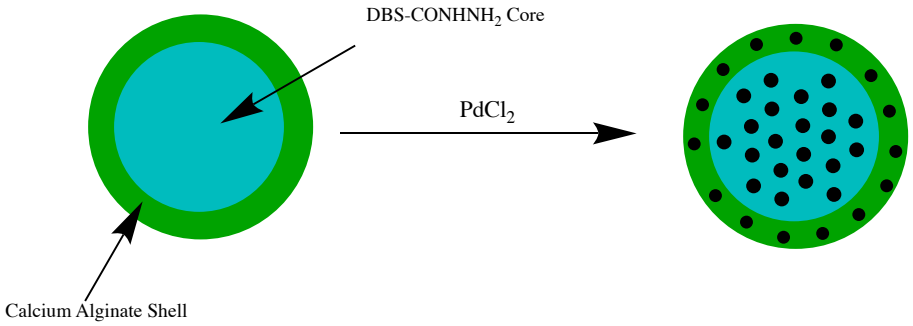

Figure 12: Formation of palladium-nanoparticle-loaded LMWG/alginate core-shell beads.

DBS-$CONHNH_2$/alginate beads may also be formulated for use in biomedical applications. Smith and co-workers[124] recently reported the use of these beads to reduce silver *in situ* to form silver nanoparticles with antimicrobial properties. Here, gel beads (c. 3 mm diameter) were immersed in silver nitrate and allowed to interact for 3 days. A colour change indicated the formation of silver nanoparticles within the gel. The silver-loaded hybrid gel exhibited good antimicrobial properties, inhibiting the growth of the Gram-positive *Enterococcus*

faecium and the Gram-negative *Pseudomonas aeruginosa*, while gels without silver nanoparticles did not exhibit any bacterial inhibition. This antimicrobial property, coupled with the ease of handling and mechanical stiffness, makes these beads excellent candidates for wound-healing applications.

2. Aims and Objectives

In the present body of work, it was planned to combine the aforementioned concepts in order to formulate multicomponent gel beads on the nanometre scale. Ideally, these beads will be below 200 nm in diameter, so as to benefit from the EPR effect where it is present and improve the targeted delivery of an anti-tumour payload. The knowledge of hybrid gel nanoparticles formed through the reverse emulsion method will be built upon, working with the LMWG DBS-$CONHNH_2$ to help limit the size of the alginate beads instead of using two different polymer gels to do so. The previous work of the Smith group will be built upon, specifically the fabrication of core-shell hybrid gel beads. It is hoped that, by altering the experimental parameters for this formulation, a reduction in bead diameter will be achieved. The parameters which will be altered are oil phase volume, temperature, stirring time, sonication, and the oil phase itself.

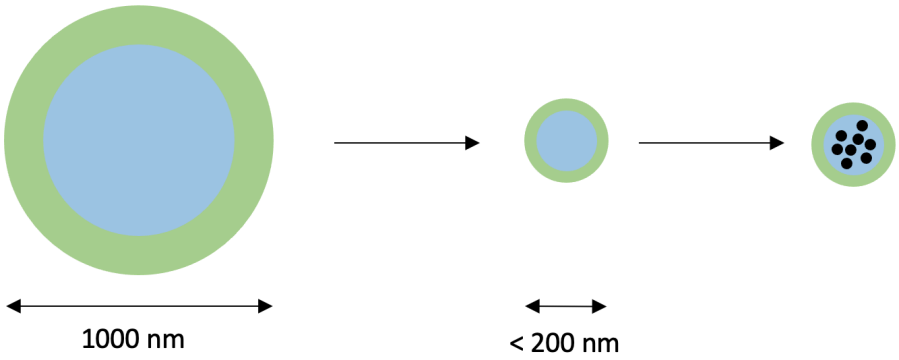

Figure 13: Schematic illustrating the main aims of the study. Briefly, a method to form microbeads of roughly 1000 nm in diameter will be built upon in order to fabricate beads of <200 nm diameter. These beads will then be functionalised with magnetic nanoparticles (black dots) with the aim of adding magnetic properties to the beads.

The incorporation of superparamagnetic iron oxide nanoparticles into the bead will also be explored. These nanoparticles will be synthesised using the co-precipitation method and will be added to the gelator mixture with the goal of forming beads with magnetic properties. It is hoped that these beads will exhibit attraction to an applied magnetic field, with the ultimate goal of use in targeted drug delivery. The possibility of *in situ* magnetic nanoparticle formation will also be explored by doping the LMWG and alginate with ferric chloride. The proposed *in situ* nanoparticle formation aims to bypass the requirement of synthesising iron oxide nanoparticles separately, simplifying the formulation of magnetic nanogels.

It is then hoped that the drug uptake and release properties of the nanogels will be explored. DBS-$CONHNH_2$ has already been shown to be effective for pH-mediated uptake and release of anti-inflammatory drugs and it is theorised that this property may be exploited for pH-mediated release of anti-cancer drugs. This hypothesis combines the possibility of exploiting the EPR effect where present and the knowledge of the slightly acidic tumour microenvironment in the hope of improving the dose of a drug which reaches a solid tumour. By adding superparamagnetic functionality to the beads, the potential for active drug targeting may be realised, further improving the efficacy of the formulation.

The ability of the LMWG to form nanoparticles through the *in situ* reduction of metal salts will be further explored through the introduction of copper chloride. It is proposed that DBS-$CONHNH_2$ will form copper-containing nanoparticles. An application of the copper

nanoparticles will then be chosen, utilising either their catalytic or antimicrobial properties. As silver has already been investigated by the group for its antimicrobial properties, it is likely that catalysis will be the chosen application of the copper nanoparticles. In this case, a copper-catalysed azide-alkyne cycloaddition (CuAAC) reaction will be chosen.

3. Results and Discussion

3.1 Synthesis of 1,3:2,4-dibenzylidene-*D*-sorbitol (DBS) $CONHNH_2$

DBS $CONHNH_2$ and its precursor DBS CO_2Me were successfully synthesised via previously reported literature methods (see Schemes 1 and 2).[112, 113] Briefly, D-sorbitol and 4-methylcarboxybenzaldehyde were mixed in a 1:2 ratio in acidic conditions at 70 ℃ using Dean-Stark apparatus to synthesise DBS-CO_2Me. Hydrazine was then added to a suspension of DBS-CO_2Me, and this mixture was left under reflux conditions overnight for the conversion to DBS-$CONHNH_2$. The products were characterised by ^1H NMR, ESI MS, and IR spectroscopy.

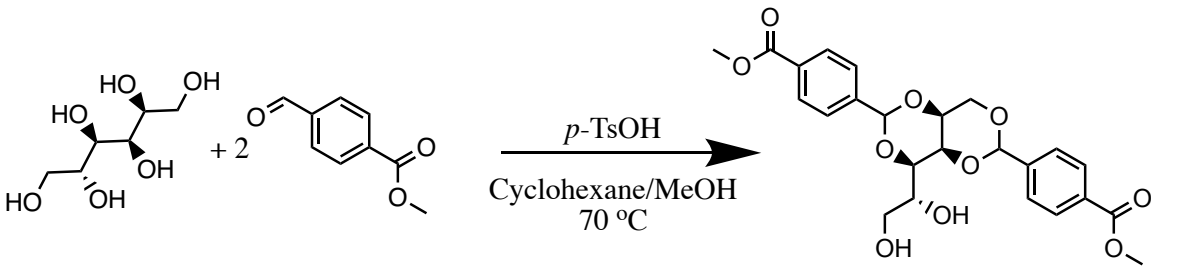

D-Sorbitol 4-Methylcarboxybenzaldehyde 1,3:2,4-Dibenzylidene-D-sorbitol CO_2Me (28% yield)

Scheme 1: Synthetic scheme for DBS-CO_2Me

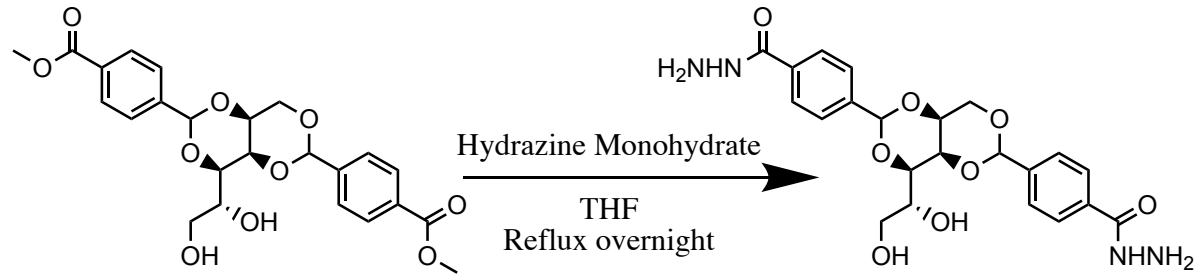

1,3:2,4-Dibenzylidene-D-sorbitol CO_2Me 1,3:2,4-Dibenzylidene-D-sorbitol $NHNH_2$ (64% yield)

Scheme 2: Conversion of DBS-CO_2Me to DBS-$CONHNH_2$ using hydrazine monohydrate

The ^1H NMR spectra of both DBS-CO_2Me and DBS-$CONHNH_2$ (see Appendices 1 & 2) were in accordance with previous literature findings.[112, 113]

The ^1H NMR spectrum of DBS-CO_2Me depicts both aromatic resonances attributed to protons and a complex set of resonances arising from the sugar backbone of the molecule. The complexity of the sugar backbone region may be due to the presence of several diastereotopic protons. Upon conversion to the hydrazide, a resonance corresponding to the NH protons was observed at δ = 9.76 while the methyl peak corresponding to the -CO_2Me group, previously observed at δ = 3.82, was no longer evident. This indicates successful conversion from DBS-CO_2Me to DBS-$CONHNH_2$. Mass spectrometry of the products showed mass ions corresponding to the mass of DBS-CO_2Me and DBS-$CONHNH_2$, both at m/z 475.2.

In summary, the principal synthetic procedure was performed successfully and a uniform white powder of the supramolecular gelator DBS-$CONHNH_2$ was yielded which exhibited

thermally triggered hydrogelation. The characterisation data obtained was in accordance with previous literature data.[113]

3.2 Synthesis of Iron Oxide Nanoparticles

Magnetite nanoparticles were synthesised following an adapted literature method.[125] In brief, ferric and ferrous chloride were mixed in a 2:1 ratio in aqueous conditions under an inert atmosphere. A capping agent, 0.226 g of sodium *n*-dodecyl sulfate, was added concurrently with ammonium hydroxide to trigger the precipitation of the iron oxide nanoparticles. The reaction proceeds as:

$$2Fe^{3+} + Fe^{2+} + 8OH^{-} \rightarrow Fe_3O_4 + 4H_2O$$

A dry, black powder was obtained in this experiment (Figure 14). This powder exhibited attraction to an applied magnetic field from a neodymium magnet, indicating the successful formation of a superparamagnetic iron oxide species. The strong IR absorbance bands observed at 554 cm^{-1} in the infrared spectrum is characteristic of Fe-O bond vibrations.[126] The series of small, almost unnoticeable IR absorbance bands in the fingerprint region are likely a result of the capping agent - sodium *n*-dodecyl sulfate - present on the surface of the nanoparticles.

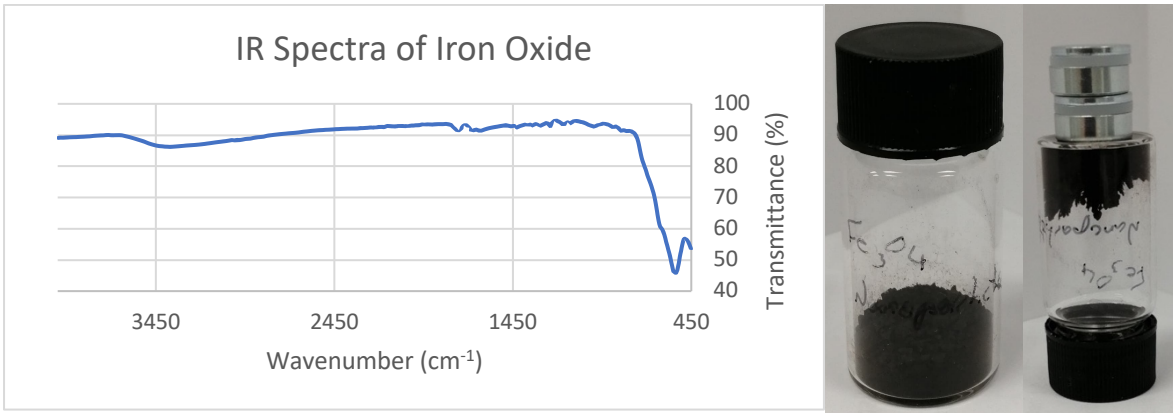

Figure 14: IR Spectrum of the obtained product (left). Black powder indicating the formation of magnetite (right). Product exhibiting attraction to applied magnetic field shown through the use of two neodymium magnets (right).

Initially, poly(ethylene glycol) was used as a capping agent, but this was found to be a poor capping agent and considerable aggregation of the nanoparticles was indicated by sedimentation and the cessation of Brownian motion. This was unexpected due to the success with this capping agent shown by Ajitha *et al*.[127] Subsequently, sodium *n*-dodecyl sulfate was used as the capping agent, as was reported to be possible by Karunakaran *et al*.,[128] resulting in more satisfactory nanoparticle formation and stability. In a preliminary experiment, sodium *n*-dodecyl sulfate was shown to not interfere with the gelation of DBS-$CONHNH_2$ at or below a 1:1 molar ratio, so it was deemed suitable for future experiments involving the combination of the nanoparticles and the multicomponent gel beads.

Evidence of magnetite formation is shown through the IR spectrum (Figure 14) of the sample, with the resonance observed at 538 cm^{-1} being indicative of iron-oxygen bond formation. When stored as a suspension in water, brown discoloration of the black nanoparticles was

observed over time. Oxidation of magnetite nanoparticles in water between 24 and 80 ℃ has been shown by Tang *et al.*[129] This indicates oxidation from magnetite to maghemite and, although not entirely ideal, is fine as maghemite retains the superparamagnetic properties observed in magnetite and exhibits bulk ferromagnetic behaviour. When imaged using TEM, a spherical morphology was observed, and the nanoparticles were seen to be around 10 nm in diameter (see Figure 15). At this size, they are small enough to yield single-domain magnets and exhibit superparamagnetic properties. The aggregation observed in the TEM images is most likely a result of the sample preparation process for TEM analysis and not a result of poor synthetic technique. This is evident through the dispersion of nanoparticles in the solvent, indicating an absence of excessive aggregation. There is the possibility that partial aggregation occurred in the sample, though not to the extent to which excessive sedimentation would occur.

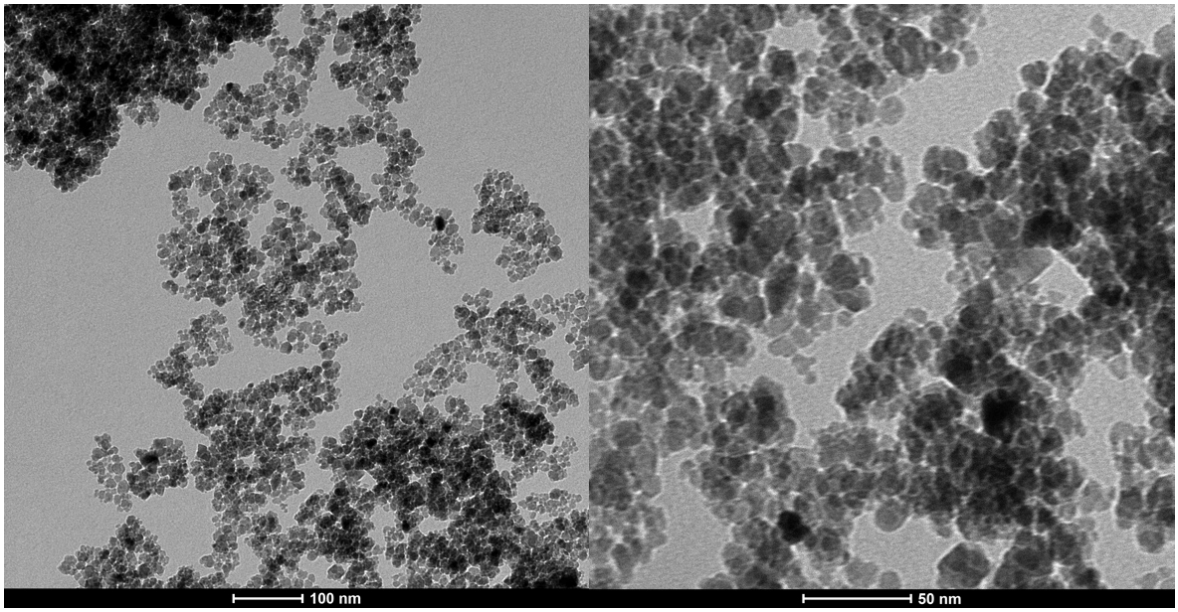

Figure 15: TEM images of iron oxide nanoparticles at 49,000 x (left) and 150,000 x (right) magnification.

Overall, magnetite nanoparticles were synthesised successfully for the purpose of integration into the multicomponent gel beads. These nanoparticles were characterised by IR spectroscopic analysis and simple magnetic attraction. When imaged with TEM, the size of the iron oxide nanoparticle was confirmed to be suitable for use in the multicomponent gel beads.

3.3 Fabrication of Multicomponent Gel Beads

3.3.1 Fabrication of Multicomponent Gel Beads

The main body of work in this project revolved around the fabrication of multicomponent gel beads, consisting of the polymer gel calcium alginate and the supramolecular gel DBS-$CONHNH_2$. The beads had previously been developed at the micrometre scale.[123] The main aim here was to investigate a manner in which the beads could be fabricated at smaller diameters. In particular, it was hoped that beads could be fabricated below the injection threshold, which is usually considered to be around 200 nm for optimal exploitation of the EPR effect.[130] The rationale behind this is that the beads would ideally act as a biocompatible drug delivery vehicle and, when combined with magnetic nanoparticles, could potentially exhibit directed, dual-action anti-tumour activity.

Gel beads were fabricated using adaptations of a previously reported method.[123] Briefly, a non-polar organic solvent (either paraffin oil, ethyl acetate, amyl acetate, *n*-butyl acetate, heptane, or hexane) was used as an oil phase into which a non-ionic surfactant (Span80) was dispersed. The aqueous phase, containing the both the polymer gelator (sodium alginate) and the supramolecular gelator (DBS-$CONHNH_2$), was then heated and dropped (20 μL/drop) over a 2-minute period into the oil phase under vigorous stirring. Calcium chloride then added to initiate the gelation of alginate. The product was then separated from the oil phase through centrifugation and washed in this manner multiple times. Finally, the product was stored in distilled water. Here, the DBS-$CONHNH_2$ is forming a gel as it cools while alginate gelation is initiated through the introduction of Ca^{2+} ions.

Between 6 and 10 centrifugation steps were performed in this procedure (10 when using paraffin oil, 6 when using any of the other oil phases) in order to achieve sufficient washing. In the case of paraffin, the paraffin itself was centrifuged before the supernatant was discarded. The obtained pellet was then dispersed in ethyl acetate and centrifuged again. The supernatant was then discarded, and this process was repeated twice more with ethyl acetate, three times with ethanol, and three times with water. This was always performed at 4990 rpm, as this was the maximum setting which could be achieved with the available equipment. This number of centrifugation steps may affect the yield of the beads, as not all beads will be collected through centrifugation and will remain suspended in the supernatant when it is discarded. According to the Stokes-Einstein equation, there is likely to be a greater distribution of smaller beads left in the supernatant and subsequently lost.

Using Stokes' Law of Centrifugation, it can be predicted that it would take around 5 days of constant centrifugation at 4,990 rpm to achieve 100% yield in paraffin wax. Larger particles are sedimented faster as they are more affected by the gravitational force exerted by the centrifuge. It could therefore be said that the results seen in the DLS are not an accurate representation of the beads formed in paraffin oil, as the smallest beads may simply not be collected.

$$v = \frac{2r^2(p - L)g}{9\eta} \qquad\qquad t = \frac{h}{v}$$

Equation 1: Stokes' Law of centrifugation. The equation on the left states how the velocity of the sphere is calculated, whilst the equation on the right states how the time to settle is calculated.
v = velocity of sphere. r = radius of sphere. p= density of sphere. L = density of medium. g = gravitational force. η = viscosity of medium. t = time to settle. h = height.

Stokes' Law states that the velocity of the sphere is largely dependent on the gravitational force enacted upon it. Therefore, the yield here could most simply be improved by increasing the rpm on the centrifuge. Unfortunately, the centrifuge available experienced rotor errors whenever an attempt was made to exceed 5,000 rpm. In future, other isolation methods could be attempted, such as dialysis.

Due to the low mass of materials being handled in this process, the yield was calculated using quantitative NMR spectroscopy. Briefly, the product was dissolved in deuterated DMSO. This destroys the gel structure and thus the gel beads themselves, nullifying the problems encountered with attempting to perform an NMR spectroscopic measurement on a gel. To

this solution, a known amount of dry acetonitrile (2 μL, 0.0383 mmol) was injected immediately before transferral to a capped tube to prevent evaporation, and used as a standard against which the integrals of the DBS-$CONHNH_2$ peaks would be compared in order to ascertain the yield.

Species	Integral	Relative Quantity	Concentration (mM)
CH_3CN	30.00	1	28.6
DBS-$CONHNH_2$ Unfiltered	0.98	0.024	0.69
DBS-$CONHNH_2$ Filtered	0.23	0.0058	0.16

Table 1: Quantitative NMR yields for DBS-$CONHNH_2$ beads in paraffin oil.

$$\frac{0.23}{4} = 0.0575\ M$$

$$\frac{0.0575}{10} \times 0.0286 = 1.64 \times 10^{-4}\ mM = 0.075\ mg/mL$$

Equation 2: Calculation of mass of sub-400 nm DBS-$CONHNH_2$ beads

$$\frac{0.98}{4} = 0.245\ M$$

$$\frac{0.245}{10} \times 0.0286 = 7 \times 10^{-4}\ mM = 0.33\ mg\ 400\ \mu L^{-1} = 0.83\ mg\ mL^{-1}$$

Equation 3: Calculation of total yield of DBS-$CONHNH_2$ beads

Firstly, the integral for acetonitrile is normalised to 30.00, meaning the per-proton integral is 10. The per-proton integral for the amine group of DBS-$CONHNH_2$ in each sample is then calculated. DBS-$CONHNH_2$ contains 4 -NH_2 protons, so the per-proton integral is calculated as $\frac{\text{integral}}{4}$. The relative quantity of DBS-$CONHNH_2$ is then calculated by dividing the per-proton integral of DBS-$CONHNH_2$ by the per-proton integral of acetonitrile. The relative quantity of DBS is then multiplied by the concentration of acetonitrile (0.0286 M) to give the concentration of DBS-$CONHNH_2$ in the final product and thus the yield.

When using paraffin oil, the yield was 28%, with 9% of these beads being present after the product was passed through a 400 nm filter. While this yield is not terrible, it is not ideal. The yield is likely due to both the number of centrifugation steps – increasing the likelihood of product loss during transfer – and the centrifugation itself.

Dynamic light scattering (DLS) was used to assess the size of each set of samples. DLS is an important technique in this process as it is useful in determining the distribution of sizes of particles in suspension, allowing for the assessment of the success in reducing the size of the beads. DLS works by directing a monochromatic beam of light into a suspension of particles. These particles, in Brownian motion, scatter the light when it hits. The pattern of scattered light detected by the equipment is related to the speed of diffusion in suspension, which is in turn related to the hydrodynamic radius of the particle, assuming the particles are spherical, through the Stokes-Einstein equation:

$$D = \frac{kT}{3\pi\eta D_H}$$

Equation 4: Stokes-Einstein equation relating hydrodynamic radius to diffusion speed. D = diffusion speed, k = Boltzmann constant, T = temperature, η = viscosity, D_H = hydrodynamic radius.

The particle size can be reported in terms of an intensity distribution or a volume distribution. In this case, results are reported in terms of volume of particles, rather than the intensity of scattering, at each size. This is because a small number of larger particles may scatter light much more than a large number of smaller particles. This would result in a distribution suggesting the average particle diameter is much larger than it is in reality. Therefore, the volume of particles at each size is used, as the area of the peak will correspond to the number of particles, allowing for the determination of the bulk size. Additionally, Z-average is not used in this investigation when analysing samples that have not been filtered. This is because, when not filtered, there may be artifacts in suspension larger than the scope of DLS, but which still scatter light and subsequently skew the results to a larger Z-average. The reason filters are not used initially is because the size of the beads in each case will not be known unless the entire sample is analysed. Should a sample show promise, then it will be filtered using a 450 nm filter and subsequently analysed. In this case, Z-average will be used as the measure for particle size.

One of the limitations of DLS analysis is that it becomes less accurate with increasing particle size. With particles greater than 1000 nm in diameter, the results cannot be considered accurate. Fortunately, for the purposes of this experiment, simply knowing that the particles are greater than 1000 nm in diameter is enough, as the ultimate aim is to achieve particles far smaller than this. A further limitation of DLS analysis may be that the sample may sediment during analysis, resulting in inaccurate results. This may be mitigated by decreasing the density of the sample, which is performed in this case by diluting the sample in 1 mL of water before analysis.

3.3.2 Effects of Changing Experimental Parameters on Bead Size

In order to ascertain which experimental parameter affected the ultimate diameter of the gel beads, individual parameters were changed until a change in diameter was noticed. Initially, the volume of the oil phase was altered from 40 mL to 200 mL. It was hypothesised that, by increasing the area into which droplets of the surfactant can disperse, these droplets would break up into smaller, more numerous micelles. This would subsequently result in a smaller bead size. Unfortunately, this was not the case and the bead diameter appeared to be independent of the oil phase volume.

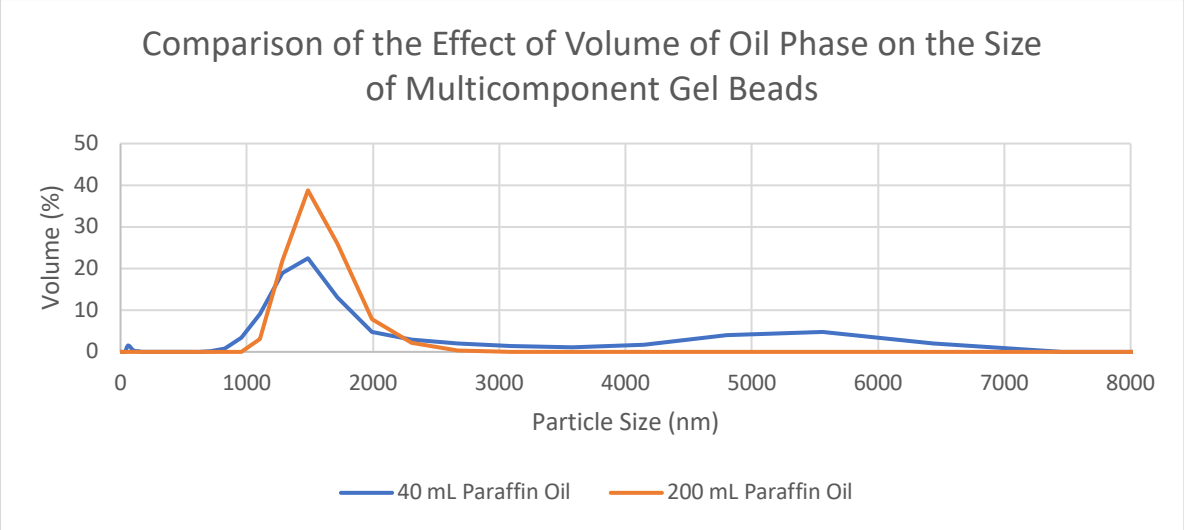

Figure 16: DLS results exhibiting the effect of increased volume on gel bead size.

At both 40 mL and 200 mL of paraffin oil, the beads were observed to be around 1500 nm in diameter, indicating there is no correlation between bead diameter and the volume of the oil phase (see Figure 16). Of course, while one of the limitations of DLS analysis is that it is not accurate above 1000 nm, these results may still be accepted as beads were not observed below 1000 nm, indicating no reduction in bead size regardless of the accuracy of DLS analysis in this case.

Interestingly, a more uniform size distribution is observed at a higher volume of oil, with the peak at 5560 nm observed at 40 mL not being observed in the analysis of the sample prepared in 200 mL paraffin oil. This may suggest that the idea of surfactant-stabilised microdroplets being able to disperse more uniformly at higher volumes may hold some merit. However, in terms of industrial application, increasing the volume of the oil phase five-fold simply to double the volume of beads at the desired size may not be economically or environmentally viable. On a more positive note, however, the fact that bead size is unaffected by oil phase volume is promising for any industrial scaling-up of the procedure, perhaps allowing for large-scale fabrication of beads in large quantities of oil-phase.

The next parameter to be investigated was the temperature at which the procedure was carried out. Here, it was believed that increasing the temperature and thus decreasing the viscosity of the oil phase may aid in the dispersion of the non-ionic surfactant, and also allow for the DBS-$CONHNH_2$ to disperse into smaller droplets before it gelates. As DBS-$CONHNH_2$ is a thermally triggered gelator, dropping it into a hot oil phase would delay gelation until the mixture is cooled. Therefore, the initially-formed water droplets may be able to break up into smaller droplets before gelation is initiated than when a room temperature mixture is used. However, it was observed that the increase in temperature did not affect the bead size, with near-identical DLS results.

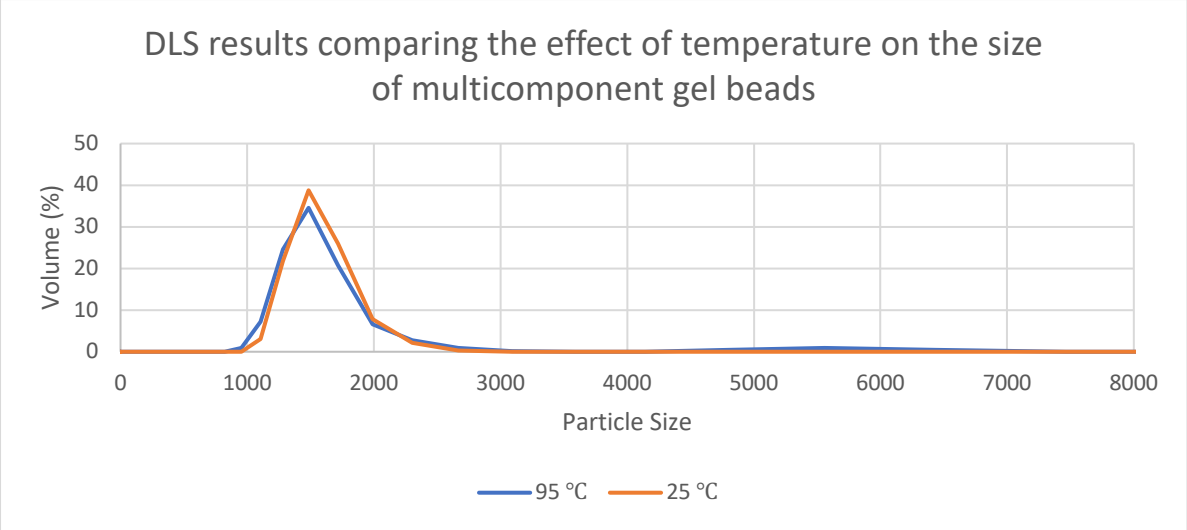

Figure 17: DLS results comparing the effect of temperature on gel bead size

The bead size observed in both conditions was around 1500 nm (see Figure 17). It may be the case that the dispersion of the non-ionic surfactant is unaffected by the temperature of the reaction mixture, and the subsequent size of the surfactant-stabilised water droplet, is the determining factor in the bead size. Furthermore, the viscosity of paraffin oil is orders of magnitude greater than the viscosity of other oil phases available, and therefore the difference in viscosity between 25 ℃ and 95 ℃ may not be significant enough to induce noticeable change in the size of the beads.

Interestingly, increasing the temperature should reverse the order of gelation in this procedure. DBS-$CONHNH_2$ is a thermally triggered gelator. Once heated above its gelation temperature, it will form a gel upon cooling. At 25 ℃, DBS-$CONHNH_2$ will gelate rapidly upon addition to the oil phase, followed by the gelation of alginate on addition of calcium chloride. At 95 ℃, however, the DBS-$CONHNH_2$ will not form a gel until the mixture is cooled after the addition of calcium chloride. This may have the effect of altering the physical makeup of the beads. It is likely that, at 95 ℃, the gelation of alginate will occur at the outermost zone of the droplet, forming a solid-like shell inside which the DBS-$CONHNH_2$ will subsequently gelate, resulting in an ideal core-shell bead. At a lower temperature, however, it is more likely that a bead with no distinct core-shell structure is formed.

Another parameter which was adjusted was the stirring time. The 20-minute stirring step after the addition of calcium chloride was changed to 10 minutes and 1 hour. It was predicted that, by increasing the stirring time, the droplets may be dispersed to a greater degree and divided into smaller beads, resulting in smaller bead size. To a certain degree, this is what was observed (see Figure 18).

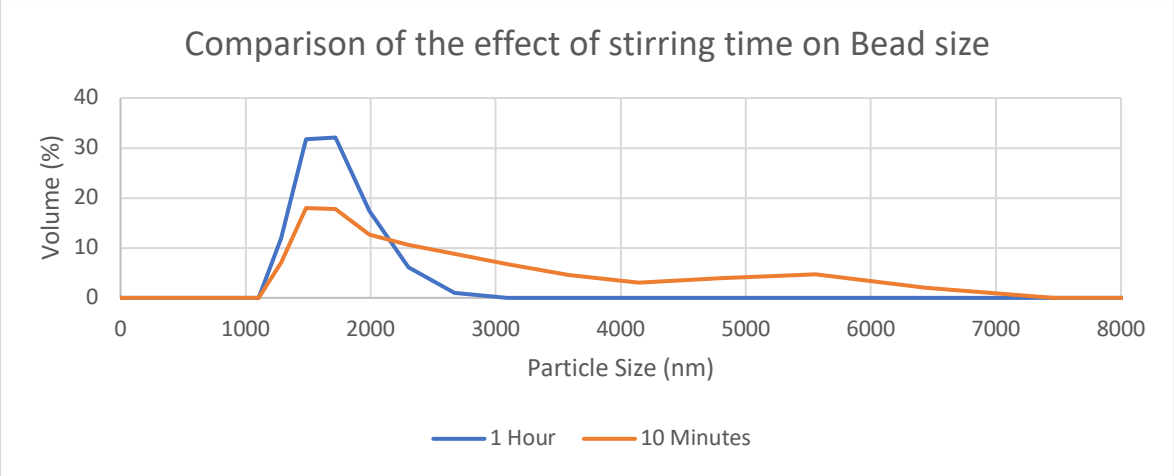

Figure 18: DLS results showing a comparison of the effect of stirring time on bead size.

There does seem to be a correlation between stirring time and average bead size. Whilst the main peak for both is observed at *ca*. 1500 nm, a larger volume of beads was observed at this size after 1 hour of stirring compared to just 10 minutes of stirring. With shorter stirring times, there was a greater contribution from large size particles. However, the bead size appeared to be limited to *ca*. 1500 nm by a different parameter. Regardless, it is important to know that an increased stirring time does aid in increasing the volume of the smallest possible beads, in line with what was hypothesized. This also helps to overcome the problem observed with large beads being present when 40 mL of the oil phase was used. By increasing the stirring time, the need to increase the volume is eliminated. However, industrially, this would introduce additional time into the procedure, reducing efficiency. Nonetheless, the importance of stirring time is highlighted here, and the correlation between stirring time and the polydispersity of the final product. The use of an industrial-grade overhead stirrer may yield greater control over the final product size, with greater control over the rate of stirring. However, the overhead stirrer which was available for this experiment was not able to reach the stirring rates achieved by a magnetic stirrer. The overhead stirrer was therefore not used for the fabrication of beads in this case.

The method of dispersing the reagents was also altered from magnetic stirring to sonication. Here, it was hoped that the ultrasonic vibrations may fragment the droplets in the oil phase to a greater degree than stirring can achieve. Briefly, the reaction vessel was suspended in an ultrasound bath and the procedure was carried out in its entirety while being sonicated. The resulting product was significantly poorer in quality than when stirring is used as the dispersion method. Such was the poor quality of the product, that DLS analysis was not required to measure the diameter, as it was in the millimetre size range. Clearly, significant aggregation occurs under the sonication conditions used (see Figure 19).

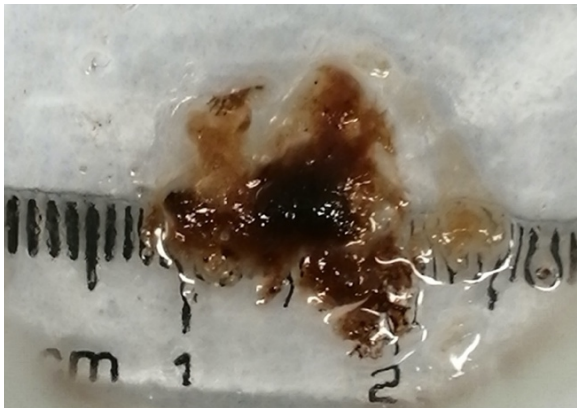

Figure 19: Gel clump obtained from conducting the procedure under sonication. Note that the brown colouration is due to the presence of iron oxide nanoparticles.

After exhausting our exploration of physical parameters, the oil phase itself was changed. When selecting an oil phase, several factors were considered. The oil phase would, of course, need to be non-polar and immiscible with water to allow for the formation of a surfactant-stabilised water-in-oil emulsion. Secondly, the viscosity would ideally be far lower than the viscosity of paraffin oil. A lower viscosity should, ideally, allow for faster dispersion of the reagents and faster breakup into smaller droplets, resulting in smaller bead size. Thirdly, the oil phase would ideally be non-toxic, or of low toxicity. As the beads are being fabricated with biomedical applications in mind, any toxic compounds which may be present in the final product are unacceptable. This issue may, however, be mitigated with thorough washing of the product to remove unwanted oil phase. With these considerations in mind, the oil phases chosen for screening were ethyl acetate, *n*-butyl acetate, amyl acetate, heptane, and hexane.

Ethyl acetate was chosen as it had previously been shown to be an effective organic phase for the preparation of alginate nanocapsules.[131] Heptane was chosen because of its low polarity, low viscosity, high boiling point for potential hot synthesis, and relatively low toxicity. Furthermore, unlike ethyl acetate, it will not have issues arising from possible hydrolysis in contact with water. Hexane was used because it has lower polarity and lower viscosity than heptane and should therefore yield better results. Toxicity concerns were taken into account with hexane, and the washing stages were increased to maximise removal of the oil phase.

Initially, the procedure was conducted in the same manner as with paraffin oil. The experimental parameters were not changed except the nature of the oil phase. It was observed that beads were not formed under these conditions, and instead a clump of gel was forming as with sonication (see Figure 20). It was decided that a stabiliser should be added to support the formation of the gel beads.

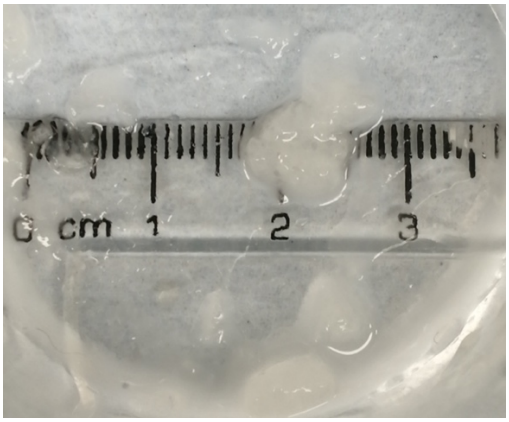

Figure 20: Clumps of gel observed when a less viscous oil phase (heptane) was used.

Glycerol was chosen to act as a stabiliser in this procedure – its non-toxicity and high viscosity made it an ideal candidate for this role. Glycerol is a humectant, and its hygroscopic properties should help to facilitate the water-in-oil emulsion. After adding 1 mL of glycerol, clumps were not observed, and beads were formed successfully. These beads were significantly smaller than those observed when using paraffin oil, reaching the nanometre scale and, when using hexane or heptane, dropping below the 200 nm target. Furthermore, the introduction of glycerol resulted in the formation of two layers in the mixture due to its immiscibility with these new oil phases. This glycerol layer was believed to contain the majority of the product, as any product not in the glycerol layer would theoretically have precipitated in the same manner as in the absence of glycerol. The glycerol was removed from the product using ethanol and water washing steps. The oil phase, therefore, was not present in the washing steps in this case.

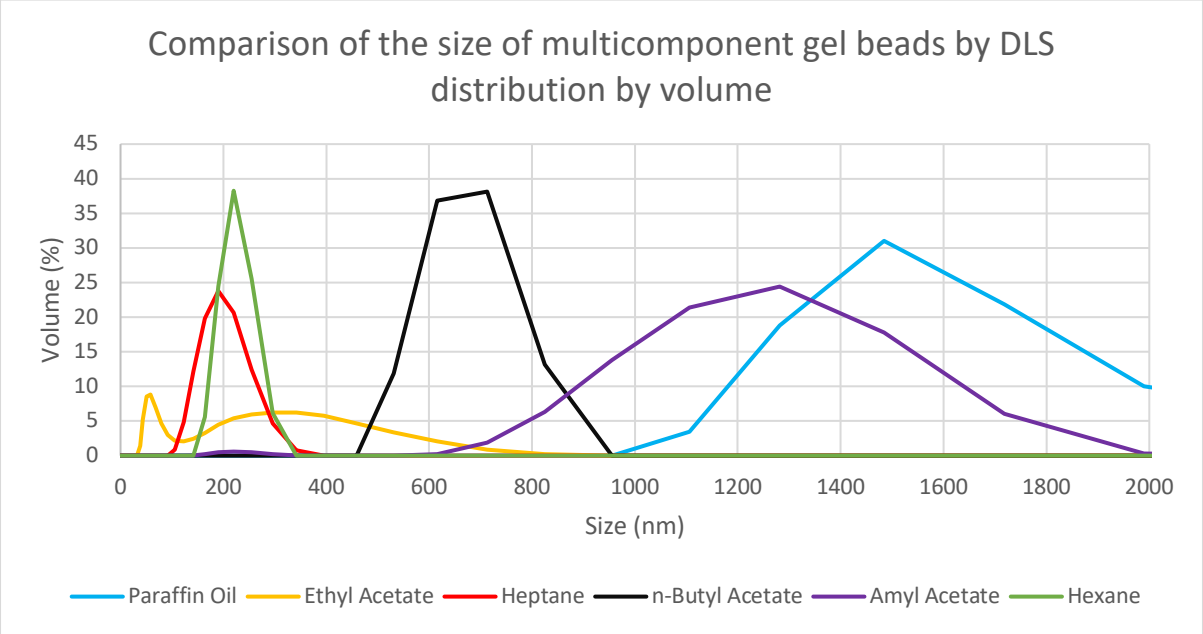

Figure 21: Comparison of the DLS results showing bead size when changing the oil phase.

Altering the oil phase was seen to have the most profound effect on the size of the beads (see Figure 21). Paraffin oil produced beads with a diameter mainly around 1500 nm, while this was reduced to 615 nm with *n*-butyl acetate and then to 190 nm with heptane. When passed through a 400 nm filter, the hexane sample had a Z-average size of 175 nm. The lowering of

bead sizes is probably a result of the lowered viscosity of these oil phases. This allows droplets of gel to be broken up faster upon addition to the stirring oil phase, resulting in smaller nanobeads before gelation occurs. Heptane, for example, has a viscosity of 0.389 cP while ethyl acetate has a viscosity of 0.426 cP. The lower viscosity of heptane here appears to have resulted in smaller bead size. It is also possible that the far lower dipole moment of heptane compared to ethyl acetate has an effect on the bead size, perhaps effecting more greater hydrophobicity and thus smaller beads. To determine which factor was more important, multiple solvents were tested. Comparison between the oil-phases (Figure 22) suggests there is a clear correlation between viscosity and particle size. This correlation is near-linear in nature, though more data points are perhaps needed at intermediate viscosities.

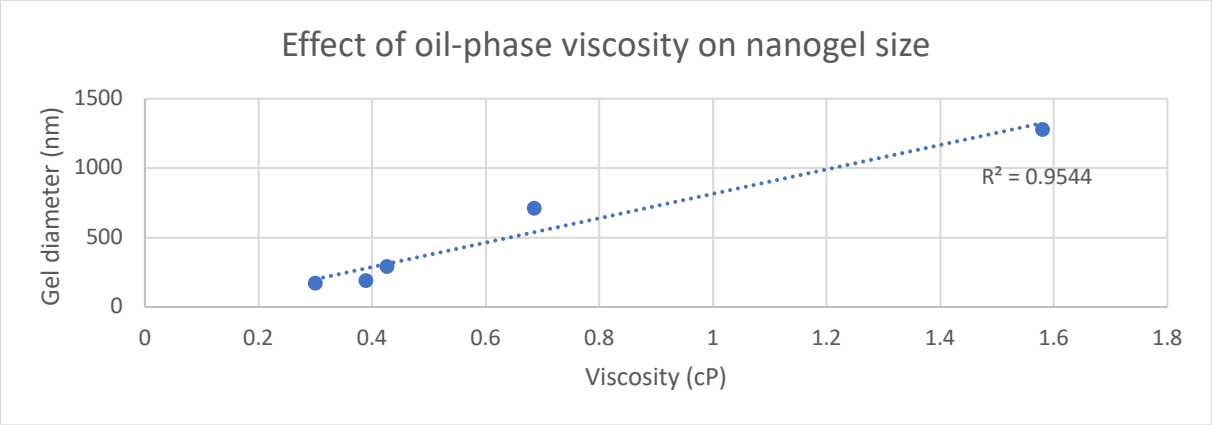

Figure 22: Graph showing the correlation between oil phase viscosity and bead size.

The ability to fabricate beads below 200 nm is an exciting revelation, allowing for the development of these beads with a biomedical goal in mind. Below this diameter, gel beads are an acceptable size for intravenous injection and can be considered for drug loading. Additionally, the correlation between oil phase viscosity and bead size may allow for the preparation of tailor-made beads of specific sizes for applications outside of intravenous drug delivery. Between 200 – 1000 nm, for example, the beads could be used for oral drug delivery. Prior to this, of course, the efficacy of the method in terms of purity of product and yield must be evaluated. Initially, IR spectroscopic analysis revealed that none of the non-ionic surfactant (Span80) is present in the product (Figure 23), which is promising as it indicates thorough washing of the product and therefore reduces the likelihood of any toxic oil phase in the final product.

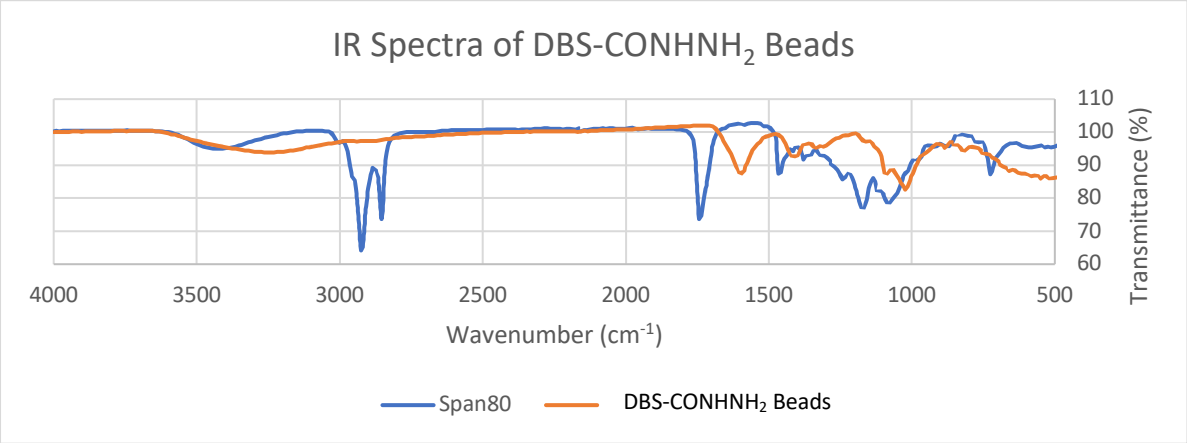

Figure 23: IR spectra showing the absence of Span80 in the final beads.

Unfortunately, the yield when using either hexane or heptane as the oil phase was too low to be detected by NMR spectroscopic analysis under standard parameters. Again, this could be explained by Stokes' Law: DLS analysis shows that the beads are mostly around 200 nm in diameter, therefore they will take even longer to settle than the beads formed in paraffin oil. The substantial decrease in size is enough to offset the increase in velocity which would be observed through the absence of the oil phase in washing. Again, in order to increase the yield here, greater gravitational force will need to be exerted on the beads in order for them to settle and collect as a pellet at the base of the centrifuge tube. A smaller volume of oil phase could also be used to reduce the distance the bead needs to travel, *h*, to settle. Summarily, it appears that the centrifugation step is the main barrier to achieving greater yield, and that increasing the gravitational force is the simplest way to improve.

Another effect of using either heptane or hexane which was taken into consideration was the potential environmental impact of these compounds. Both are serious environmental hazards and, while 40 mL at a time is a relatively small quantity, the amount used adds up over time, especially if the process were to be used on an industrial scale. Increasing concerns around environmental pollution and climate change mean that new processes should, ideally, be developed with environmentalism in mind. To this end, it was proposed that no beads would remain in the oil phase in the process involving glycerol – all beads would be in the glycerol layer. This would result in the oil phase retaining its purity throughout the procedure, allowing it to be reused and eliminating environmentally hazardous waste. To investigate this, the oil phase was separated from the glycerol layer and analysed using NMR spectroscopy. The spectrum obtained for heptane was relatively pure, indicating the potential for reusing this oil phase and reducing environmental waste. However, the spectrum obtained for hexane contained some impurities and shows that this procedure would not have as much green potential as when using heptane (see Figure 24).

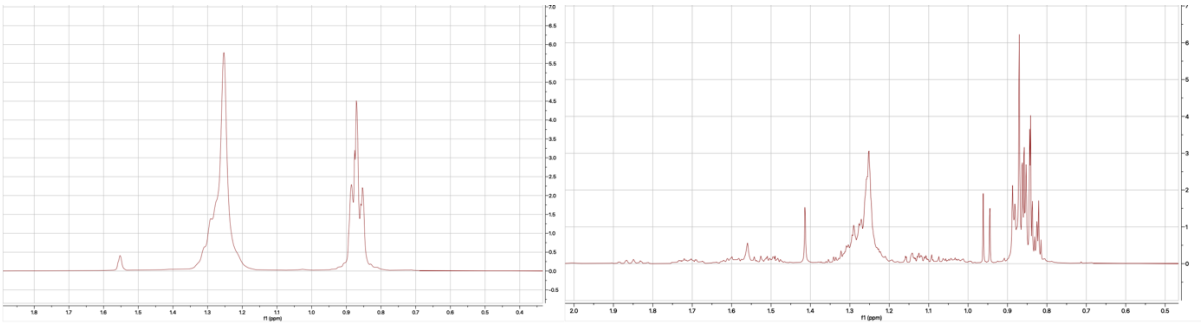

Figure 24: NMR spectra for used heptane (left) and hexane (right)

While this is not ideal as hexane yielded the smallest beads, it may be preferable to turn to heptane as an alternative. It is not as toxic as hexane and so its use in the fabrication of biomedical materials is not as concerning. It yields similar bead sizes to hexane, and these may be further improved upon by altering physical parameters such as increased stirring speed. Furthermore, heptane has a far higher boiling point than hexane, allowing for the fabrication of multicomponent gel beads at a higher temperature which, as previously mentioned, would be more likely to result in a core-shell structure. This would simply not be possible using hexane with its boiling point of 69 °C when compared to that of heptane (98 °C). From this conclusion, hot fabrication was attempted in heptane. It was hoped that, in accordance with the temperature-independent size observed in paraffin oil, the beads formed would remain at the 190 nm diameter observed at room temperature.

Unfortunately, the beads formed were *ca*. 1300 nm in diameter, more than five times larger than the diameter observed in room temperature (see Figure 25). This is not ideal, as a successful fabrication of sub-200 nm beads at this temperature would have been an important step forward. However, this can likely be explained through the differences in physical setup, rather than an odd temperature-dependence occurring when using heptane. At room temperature, a cross-bar stirrer was used in a 100 mL beaker, whereas when performing the procedure in an oil bath a rounded stirrer was used in a 100 mL round-bottom flask. The cross-bar stirrer has the effect of inducing a greater and more vigorous vortex in this procedure, inducing greater fragmentation of droplets and therefore smaller bead size. Should the procedure be replicated exactly, with a beaker suspended in an oil bath using this stirrer, smaller beads should be observed. The procedure would have been repeated using a cross-bar stirrer had there been more time remaining for the project.

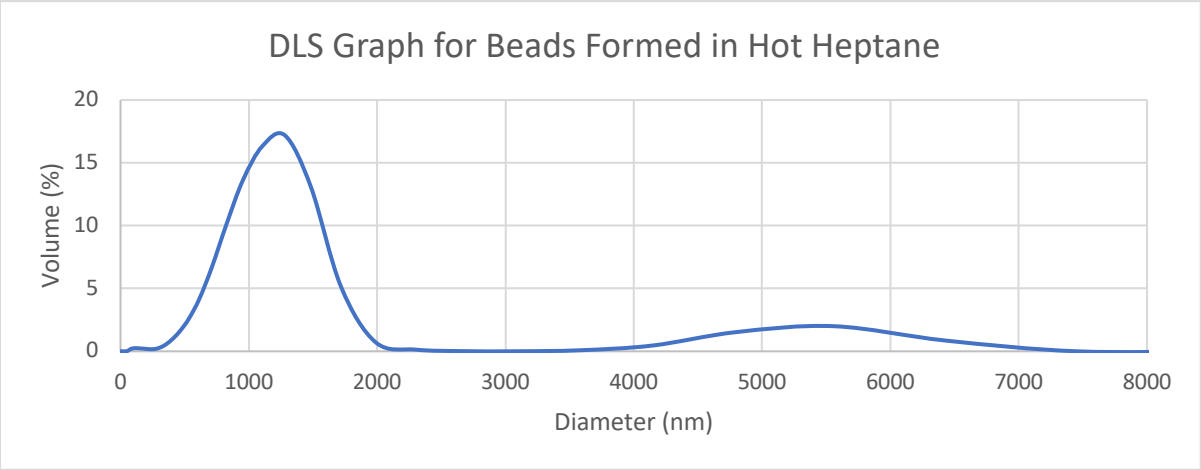

Figure 25: DLS graph for beads formed in hot heptane.

3.3.3 Addition of Magnetic Nanoparticles to Gel Beads

The possibility of adding magnetic nanoparticles to the beads was then explored. This was done with the intention of adding ferromagnetic properties to the beads so that they could be directed in solution using an applied magnetic field. This would be a key step towards realising a dual-action drug delivery vehicle which can be directed towards a target site using an applied magnetic field. These nanoparticles, previously synthesised and presented as a 1 mg/mL suspension, were added to the gel mixture at the beginning of the procedure in the hope that the gel would form with the nanoparticles present within the gel. As a proof-of-concept experiment, this was first performed with millimetre-sized multicomponent beads, and it was observed that gelation was not impeded by the presence of iron oxide nanoparticles. Furthermore, these beads exhibited attraction to an applied magnetic field.

Following this, the effect of iron oxide nanoparticles on the size of the beads was investigated. It was hoped that these nanoparticles would not affect the bead size, and beads in the nanometre size range would still be formed. This was investigated using amyl acetate as an oil phase, and the results were in line with the hypothesised scenario. The beads formed were 295 nm in diameter (see Figure 26), exactly the same as the observed diameter in the absence

of iron oxide nanoparticles. This is an ideal result, as it shows that the incorporation of iron oxide nanoparticles is not a barrier to achieving injectable multicomponent gel beads.

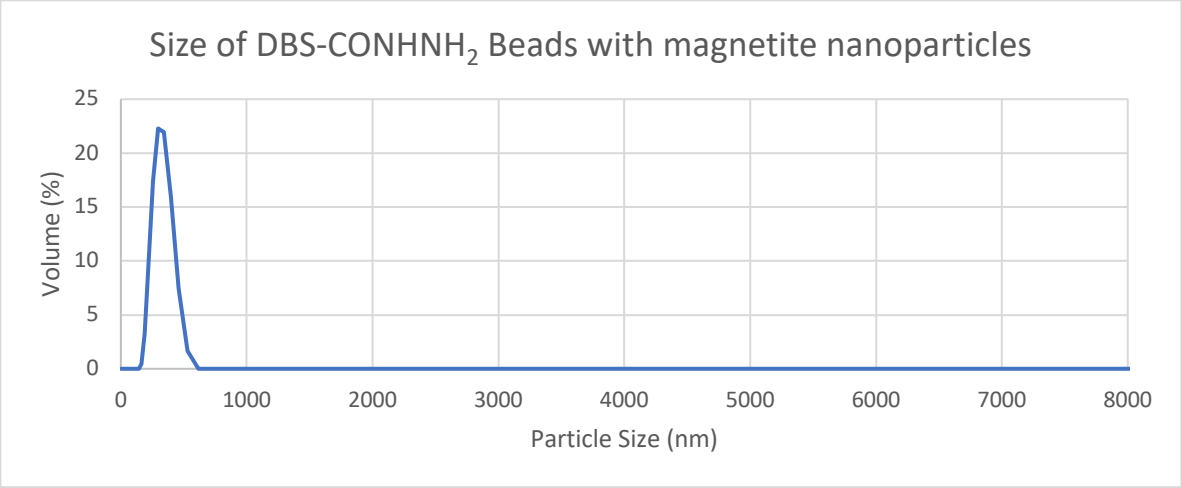

Figure 26: DLS Graph showing the size of gel beads formed in the presence of iron oxide nanoparticles.

While the product displayed a light brown colouration, indicating the presence of iron oxide nanoparticles, this is not sufficient evidence to show the nanoparticles are in the beads. These iron oxide nanoparticles could be suspended freely in the final product, completely separate to the beads. In order to determine incorporation into the beads, TEM microscopy was used to image the gels (see Figure 27). While the sample preparation procedure results in the aggregation and destruction of the beads, the iron oxide nanoparticles should still be observed in the gel structure rather than external to it.

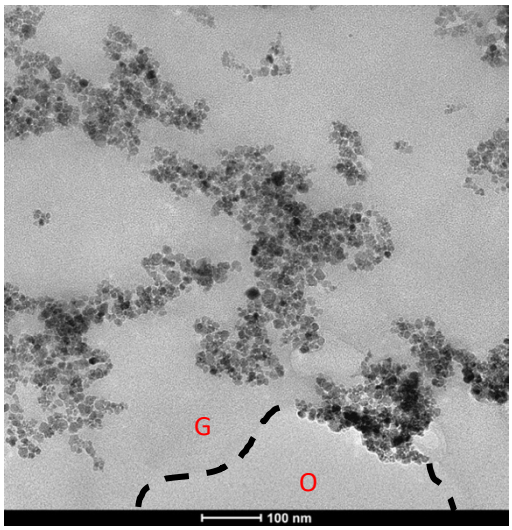

Figure 27: TEM image of iron oxide nanoparticles within the gel structure. Imaged at 49,000x. The gel (G) and outer region (O) are separated by the highlighted membrane.

While difficult to see due to the poor contrast obtained with a gel in TEM, it can be seen that the iron oxide nanoparticles are contained within the gel, rather than external to it. This is an important observation, as it indicates the success of this procedure in fabricating multicomponent gel beads with ferromagnetic properties. These beads should exhibit attraction to an applied magnetic field and, depending on the strength of this field, should be able to move through a liquid medium in a manner similar to that observed by Rocher *et al*.[132]

Overall, this section of research can be considered a success. According to DLS results, beads are being fabricated below the injectable limit of 200 nm and, moreover, there is scope to develop custom-made beads of predetermined sizes by selecting different oil phases. The final product is clean, as shown by IR spectroscopy, and does not contain traces of the oil phase or the non-ionic surfactant. This means that the beads should retain the biocompatibility and non-toxicity which is characteristic of calcium alginate and DBS-$CONHNH_2$, allowing them to be used for possible biomedical purposes. Furthermore, the new process has green potential when using heptane, as the oil phase is left clean after separating it from the glycerol layer, allowing it to be reused and preventing environmentally hazardous waste from being discarded. Industrially, this would also improve the economic viability of the process, reducing the volume of oil phase required to repeat the process. Additionally, iron oxide nanoparticles have been added successfully to the beads, imparting ferromagnetic properties unto them without affecting their size. The main failure of the novel method is the poor yield, but this can be explained by way of insufficient centrifugation and can be rectified through an increase in gravitational force in order to achieve a greater yield.

3.4 Doping gels with metal salts

Following this, it was proposed that there may be a way to form iron oxide nanoparticles *in situ* – that is, formed within the gel beads rather than being synthesised separately and added during the fabrication process. Typically, to form iron oxide nanoparticles, a base is added to a mixture of ferrous and ferric ions. DBS-$CONHNH_2$ is both basic and has been shown to act as a reducing agent to reduce palladium for catalysis. While iron has a lower reduction potential than palladium, there remained the possibility that DBS-$CONHNH_2$ would be able to form iron oxide nanoparticles *in situ*. Furthermore, it has previously been shown to be possible to form iron oxide nanoparticles starting from only ferric ions, as opposed to a mixture of ferric and ferrous ions. It was also speculated that this approach could be multifaceted, and the DBS-$CONHNH_2$ could be used to adsorb ferric ions from water, perhaps as an environmental application. This was explored first, and the uptake of ferric ions by the gel was investigated prior to determining the fate of the ions within the gel.

3.4.1 Iron Chloride and DBS-$CONHNH_2$

This was initially tested using a bulk sample of the gel, rather than the gel nanobeads, in order to facilitate the analysis. Briefly, a method was devised wherein 1 mL of a 0.1 M metal salt solution was layered on top of a 1 mL 0.4% wt/vol DBS-$CONHNH_2$ gel in a vial and the uptake of metal ions was measured via UV-vis spectroscopy over a period of three days. The solution in which the gel was stored was measured, rather than destroying the gel itself, and so a reduction in the intensity of the absorbance max was expected. Ferric ions possess no useful UV-vis properties, and so this method would be unsuccessful without treatment of the solution once it had been removed from the gel. In this case, the solution was treated with potassium thiocyanate, which forms a blood-red, UV-active solution when introduced to ferric ions (Equation 5). The complex strongly absorbs at 450 nm and can therefore be measured via UV-vis spectroscopy. The amount of this complex which forms in solution is dependent upon the amount of ferric ions present. The more ferric ions that are present, the more iron thiocyanate complex forms, the more intense the UV absorbance. This therefore allows for the quantification of ferric ions remaining in the solution over time.

$$[Fe(H_2O)_6]^{3+} + SCN^- \rightleftharpoons [Fe(SCN)(H_2O)_5]^{2+} + H_2O$$

Equation 5: Equilibrium of iron thiocyanate

This is exactly what was observed over a 3-day period. Rapid diffusion into the gel was initially observed, before uptake began to plateau after around 120 minutes (see Figure 28). The concentration of ferric ions in the solution decreased from 0.1 M to 0.052 M. However, it has to be remembered that on addition to the gel, the effective volume of the 1 mL of solution is doubled to 2 mL, with the solvent in the gel. So a reduction in Fe(III) concentration by 50% would be fully expected based on passive partitioning of the metal ion across all the liquid-like phase. While this is disappointing for any possible environmental applications, it does not signal failure for the formation of iron oxide nanoparticles within the gel.

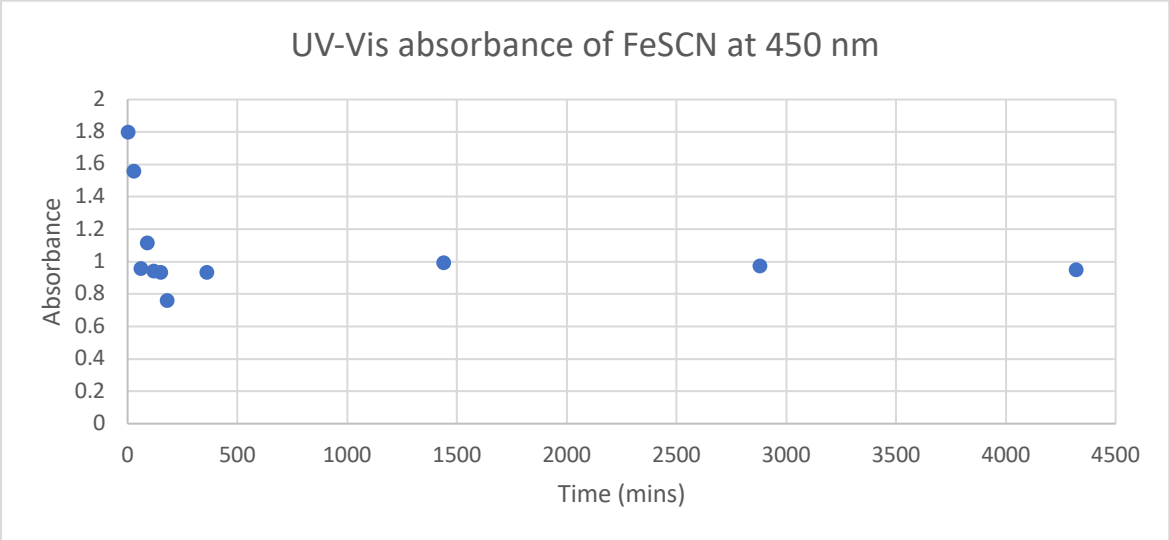

Figure 28: Plot of UV-Vis absorbance values of FeSCN solution over time after being introduced to DBS-CONHNH$_2$ gel.

Following the diffusion of ferric ions into the gel, the fate of these ions needed to be ascertained. The formation of nanoparticles in the gel was explored by TEM analysis, as any nanoparticles would be clearly visible as black dots within the gel. To prepare these gels, in short, ferric chloride solutions of concentrations ranging from 1.0 M to 0.005 M were prepared. An aliquot of each of these solutions (1 mL) was added to a separate vial containing 1 mL of 0.4% w/v DBS-CONHNH$_2$ gel. These were wrapped in foil and left for 48 hours before being submitted for TEM analysis. As a control, a sample of 1 mL alginate gel was also prepared and doped with iron chloride at these concentrations. A multicomponent gel was also formed for comparison by heating a 1 mL mixture of DBS-CONHNH$_2$ and sodium alginate in a vial, allowing it to cool to form DBS-CONHNH$_2$ gel, and then adding calcium chloride to gelate alginate. This multicomponent gel was then doped with ferric chloride in the same manner as the other two gels.

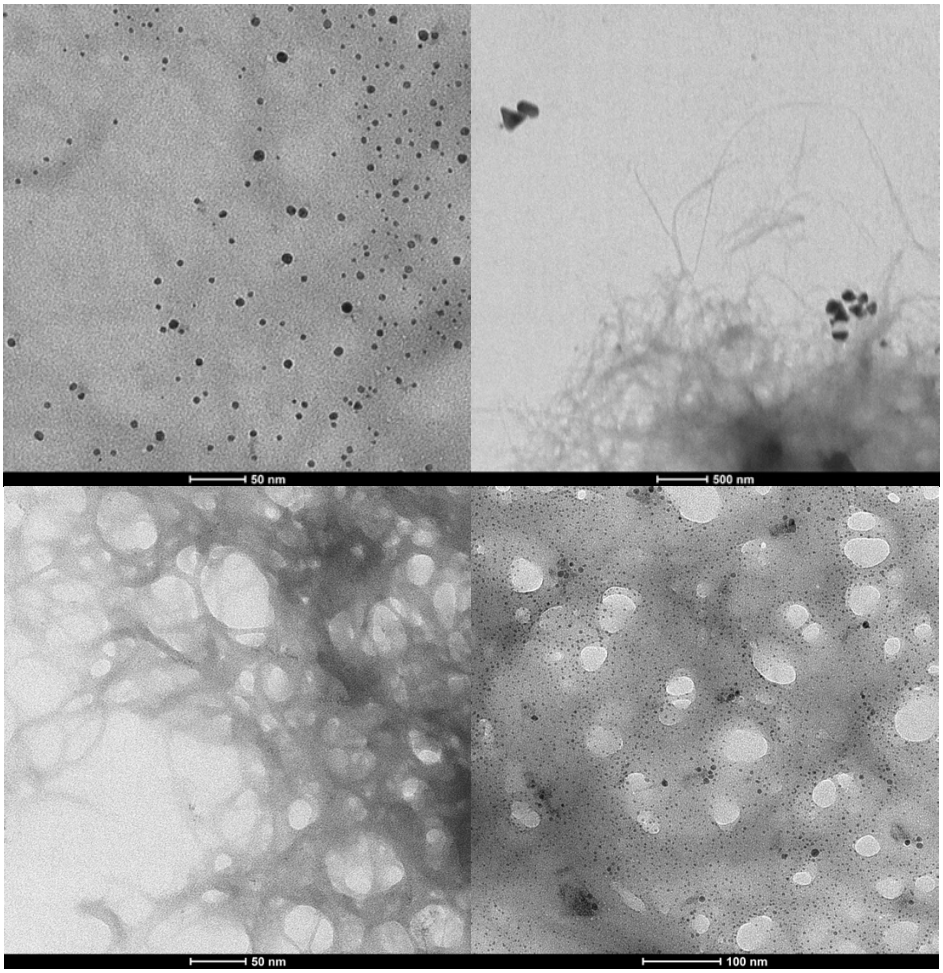

Figure 29: TEM images of iron nanoparticles formed in DBS-CONHNH$_2$ gels.
Upper Left: Iron oxide nanoparticles formed at 0.05 M imaged at 98,000x magnification.
Upper Right: Iron nanoclusters formed at 0.1 M at 9,300x magnification.
Lower Left: TEM image of calcium alginate gel after being doped with iron chloride. The image shows the lack of formation of nanoparticles. 98,000x magnification.
Lower right: TEM image showing formation of nanoparticles in a multicomponent gel. 68,000x magnification.

It was observed that nanoparticles formed successfully within the gel (see Figure 29). When using a 0.05 M solution of ferric chloride, spherical nanoparticles of noticeable polydisperse size were formed while larger nanoclusters were formed at the higher concentration of 0.1 M. In the case that nanoparticles formed successfully, it was expected that nanoclusters rather than nanoparticles would be more likely to form at a higher concentration. This is acceptable, as it shows an upper limit for concentration when forming these nanoparticles. The nanoparticles which were formed when using a 0.05 M solution of ferric chloride were likely formed by hydrolysis. The basicity of DBS-CONHNH$_2$ has seemingly removed the need for a base such as ammonium hydroxide in the formation of iron oxide nanoparticles in this procedure. This is beneficial as it potentially removes components such as ammonium hydroxide from a process which aims to fabricate materials for biomedical purposes. In order to accurately quantify the magnetic susceptibility of these gels, magnetometry would need to be employed. Furthermore, the action of DBS-CONHNH$_2$ is evidenced through the lack of nanoparticle formation in alginate gel.

In the absence of magnetometry, magnetic properties could be predicted by determining the identity and oxidation state of the nanoparticles which were formed. As these nanoparticles

are embedded in the gel, they cannot be isolated for analysis by IR spectroscopy to find an iron oxide absorbance band, for example. Therefore, a more probing method which can detect heavy ions in an organic network was needed. X-ray photoelectron spectroscopy (XPS) was chosen as the ideal method to this end. Samples of ferric chloride-laden DBS-$CONHNH_2$ were prepared and dried under vacuum to form a dry powder for XPS analysis.

XPS analysis is an excellent technique for identifying the composition of metal within the gel. It reveals not only the chemical composition of the material, but also the oxidation states and bonds between chemicals. It was reasoned this would be useful in identifying Fe-O bonds in the material, which will indicate the formation of iron oxide nanoparticles. This technique works by directing a beam of electrons in the X-ray wavelength from a source, through a monochromator, onto the surface of a sample. These electrons collide with electrons within the sample, causing the electrons within the sample to be emitted as photoelectrons. This is known as the photoelectric effect. The kinetic energy (KE) of this photoelectron is measured by the equipment. KE is determined by the incident radiation energy (hυ) and the binding energy (BE).

$$\mathrm{KE} = \mathrm{h}\upsilon - \mathrm{BE}$$

Equation 6: Photoelectric effect equation for the determination of kinetic energy of a photoelectron.

The binding energy is dependent upon the element and orbital from which it is emitted and the chemical environment of the atom from which it is emitted. BE is characteristic of different elements in different oxidation states and chemical environments, allowing for the precise identification of elements present on the surface of a sample. Additionally, this technique is quantitative, as the number of electrons emitted at each binding energy is measured as intensity. An XPS plot will therefore display the number of electrons detected at each binding energy as sharp peaks, allowing for both qualitative and quantitative measurement of a sample.

There are, however, a number of limitations of XPS analysis which must be considered when analysing the results. Firstly, this technique is not overly sensitive. Detection limits may be as low as 100 ppm when analysing heavy metals, becoming less sensitive with decreasing atomic weight.[133] When working with DBS-$CONHNH_2$ doped with ferric ions, the final concentration within the gel was 0.048 M, or 268 ppm. It was undesirable to increase the concentration, as this was shown to affect the fate of the iron nanoparticles, which would instead form large nanoclusters at higher concentrations. Therefore, it was hoped that increasing the total volume of sample by preparing a larger number of vials of DBS-$CONHNH_2$ doped with ferric ions, coupled with increased measurement times, would allow for the detection of and analysis of iron within the gel. Secondly, there is the potential for the sample to be degraded by the X-ray during measurement. However, this is unlikely to affect the iron within the sample as it is not degraded by X-rays. The DBS-$CONHNH_2$, however, is likely to be degraded by incident X-rays. Fortunately, the main focus of this experiment is the characterisation of iron.

The XPS spectrum for ferric chloride-doped DBS-$CONHNH_2$ (see Figure 30) revealed much about the nature of the nanoparticles which were formed in the gel. The formation of metal-oxygen bonds was observed, as well as some reduced species of iron. This indicates that these nanoparticles may be the desired iron oxide nanoparticles. The binding energy of Cl 2p was

observed to be 199 e.V., which is in agreement with the value obtained for $FeCl_3$ by Usha *et al*.,[134] indicating the presence of iron-chlorine bonds within the gel, and the intensity indicates that this may be the dominant iron compound in the gel. However, it is also indicated that DBS-$CONHNH_2$ is capable of acting as both a base and a reducing agent in this process in order to form iron oxide nanoparticles. This result indicates that it is possible to develop *in situ* formation of iron oxide nanoparticles to impart bulk ferromagnetic properties onto the gel beads, but the overall amount of iron oxide nanoparticles may be too small to achieve this bulk characteristic.

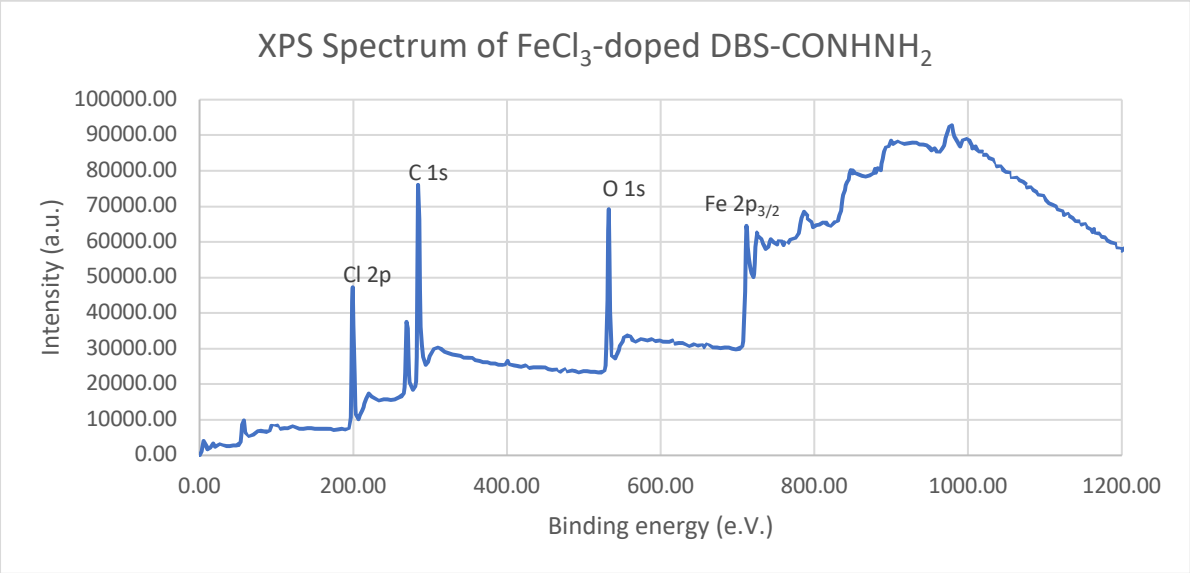

Figure 30: XPS Spectrum of $FeCl_3$-doped DBS-$CONHNH_2$

When observing the oxygen 1s region on the XPS spectrum (see Figure 31), a small peak characteristic of oxygen 1s in an oxygen-metal bond is observed as a shoulder on the main peak. While this peak is small in comparison to organic oxygen, this is likely due to the oxygen content of DBS-$CONHNH_2$ being more present than the amount of oxygen present in iron oxide; there is far more DBS-$CONHNH_2$ than Fe-O, therefore there will be more organic oxygen. Nevertheless, the presence of this peak confirms the formation of some iron oxide species, as no other metal was detected in the analysis. However, the intensity of this peak for Cl 2p is far greater than this, indicating that much more iron is present as iron chloride than iron oxide.

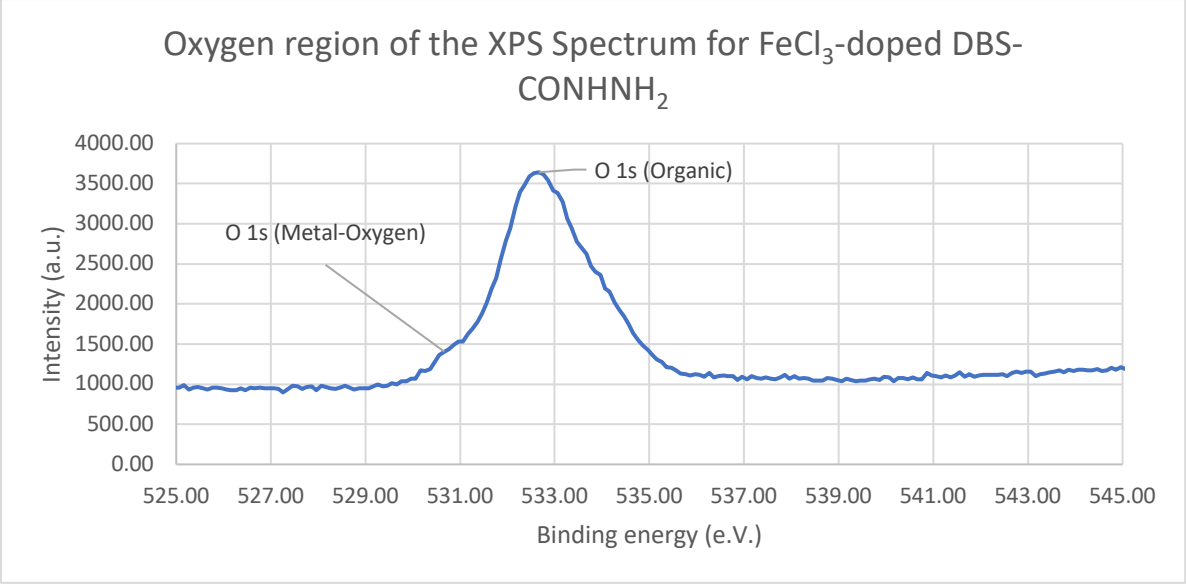

Figure 31: Oxygen region of the XPS spectrum for ferric chloride-doped DBS-CONHNH$_2$.

In the iron region of this XPS spectrum (see Figure 32), two peaks are observed for the iron 2p orbital. Unfortunately, these peaks are similar across multiple oxidation states of iron making it difficult to decipher exactly in which oxidation state the iron in the sample resides. The intensity of the peak for the iron 2p$_{1/2}$ closely matches the data reported by Radu *et al.*[135] for magnetite nanoparticles. Furthermore, the full-width at half-maximum (FWHM) value for the Fe 2p$_{3/2}$ peak observed here is around 4 e.V., which is again in agreement with the FWHM data reported by the same group for magnetite. This indicates that iron oxide nanoparticles may be present within the DBS-CONHNH$_2$ gel. The binding energies observed here also resemble those observed by Zhou *et al.*[136] for Fe in FeCl$_2$, also indicating the presence of an iron chloride species in the sample. XPS here has provided evidence of the presence of iron chloride bound to the gel, while the slight discolouration of the gel suggests some level of hydrolysis of iron chloride resulting in the formation of iron oxide nanoparticles

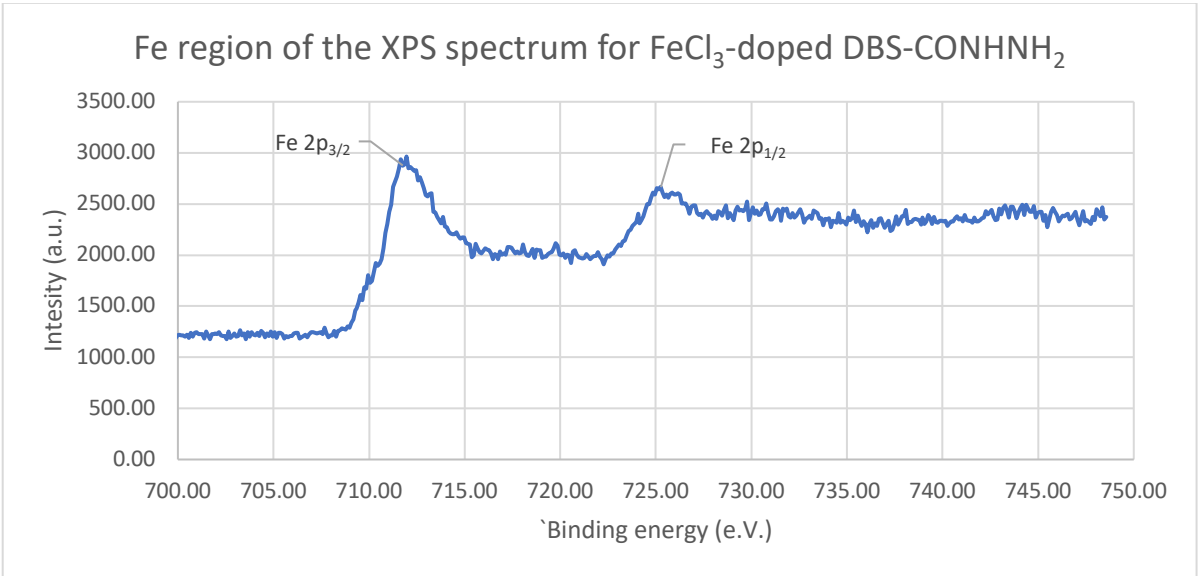

Figure 32: Iron region of the XPS spectrum for ferric chloride-doped DBS-CONHNH$_2$.

Following XPS analysis, powder x-ray diffraction (PXRD) analysis was performed on a sample of dried ferric chloride-doped DBS-$CONHNH_2$. This was done in an attempt to decipher the phase of the iron oxide structure and complement the information provided by XPS. In this technique, X-rays are incident on a powder sample. Provided the sample is crystalline, the X-ray will diffract from the sample in a characteristic pattern which can be compared against a database in order to determine the crystal structure. Amorphous solids, such as DBS-$CONHNH_2$, do not appear in PXRD diffraction patterns, and so the only observed peak should be that of the iron oxide nanoparticles. As X-rays interact with the surface of a crystal, some are diffracted and some pass through to the next layer where, again, some are diffracted and some pass to the next layer. This is repeated to form a diffraction pattern which is unique to a crystal structure. In the measurement process, the sample and the X-ray beam are both rotated to span different incident angles of X-rays, and the intensity of X-ray reflection from the sample is measured. Peaks will only be observed when there is constructive interference, which occurs as a result of Bragg's Law (Equation 7) being satisfied:

$$sin\theta = \frac{n\lambda}{2d}$$

Equation 7: Bragg's Law of X-ray diffraction. θ is the angle of incidence, λ is the x-ray wavelength, d is the crystalline spacing between layers.

Briefly, the sample was prepared in the same manner as for XPS but was then dissolved in acetone and deposited on a sample holder. The acetone was allowed to evaporate before the sample was analysed. A peak was observed at 2θ = 50 ° (see Figure 33), but this is likely a result of spectral contamination from Cu K_{beta} radiation. Outside of this peak, no other peak was observed. This may be due to extremely low concentration of iron nanoparticles in the sample but may also be due to the formation of amorphous iron oxide with no crystalline order. The most likely explanation is concentration below the detection limit of PXRD.

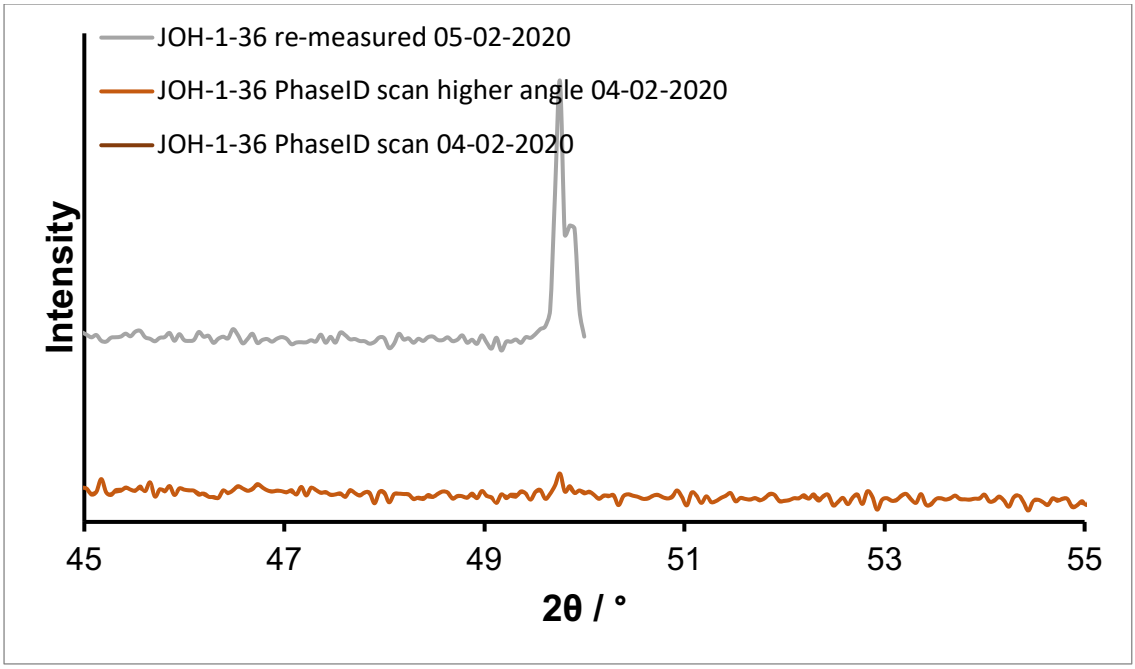

Figure 33: PXRD graph for ferric chloride-doped DBS-$CONHNH_2$.

In summary, there is insufficient data the *in situ* formation of iron oxide nanoparticles. Iron is incorporated into the gel and nanoparticles are formed, but the identity of these

nanoparticles is not fully elucidated. It is possible that there is molecular iron chloride bound to the gel while some iron oxide nanoparticles formed through hydrolysis. The ability of DBS-$CONHNH_2$ to play a role in the formation of iron oxide nanoparticles is supported by the formation of nanoparticles in this gel and not in calcium alginate.

3.4.2 Copper Chloride and DBS-$CONHNH_2$

The possibility of forming nanoparticles *in situ* with other metals was also explored. Namely, copper was chosen to run as an analogue to the iron study. Copper nanoparticles have previously found use in antimicrobials, conductive nanoinks, and as catalysts. With these potential applications in mind, a similar route of investigation was embarked upon as that which was taken with iron, and an application was to be explored once the nature of the nanoparticles was elucidated. In short, 1 mL of 0.1 M cupric chloride solution was layered on top of 1 mL of 0.4% w/v DBS-$CONHNH_2$ gel and left for 48 hours. The uptake of cupric ions was measured using UV-vis spectroscopy, and the fate of these ions within the gel was explored using TEM and XPS analyses.

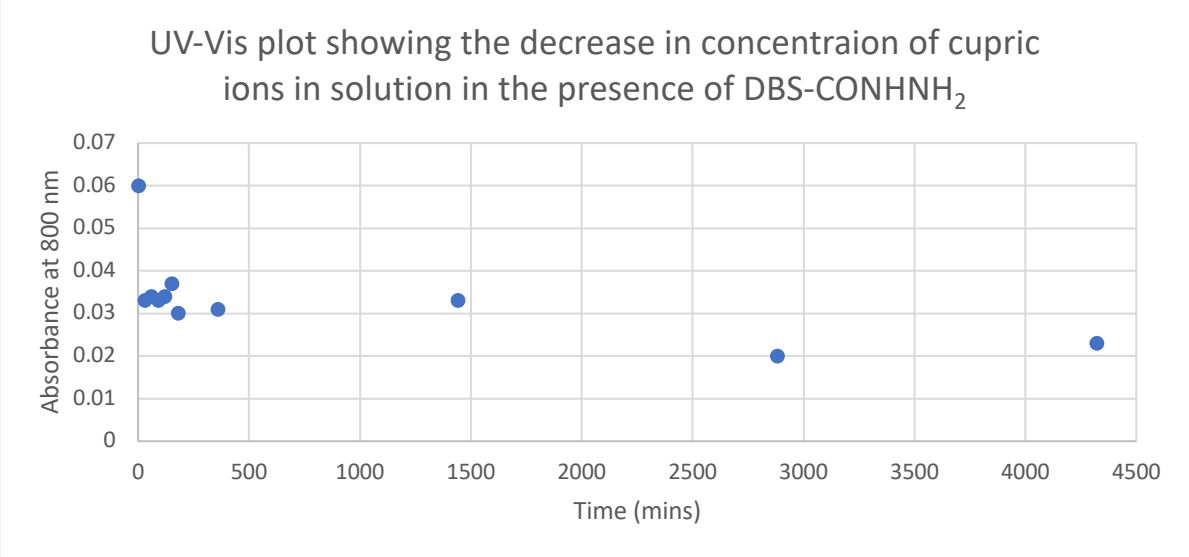

Figure 34: UV-vis Plot of the decrease in concentration of cupric ions in solution as determined by UV-vis spectroscopy.

UV-vis spectroscopic analysis of the uptake of cupric ions revealed a similar pattern to that observed with ferric ions; a sharp uptake over the first 120 minutes followed by a plateau (see Figure 34). In this case, absorbance was measured at 800 nm and a decrease in the intensity at the absorbance maximum from 0.060 to 0.023 was observed, which equates to a decrease from 0.1 M to 0.038 M cupric ions in the solution when the results are plotted against a calibration curve. This is interesting, as it shows the formation of a concentration gradient, where the concentration of cupric ions is higher in the DBS-$CONHNH_2$ than it is in the surrounding solution. This indicates that there is some active uptake into the gel, rather than just the passive diffusion observed with ferric ions. There is some affinity between cupric ions and DBS-$CONHNH_2$ which was not observed with ferric ions, and this affinity may be occurring at the hydrazide groups on either end of the DBS-$CONHNH_2$ molecule, perhaps complexing around the copper (see Figure 35) as has been observed with benzyl hydrazide groups.[137] In this case the complexation is purely speculative, and was later disproved by the XPS spectrum.

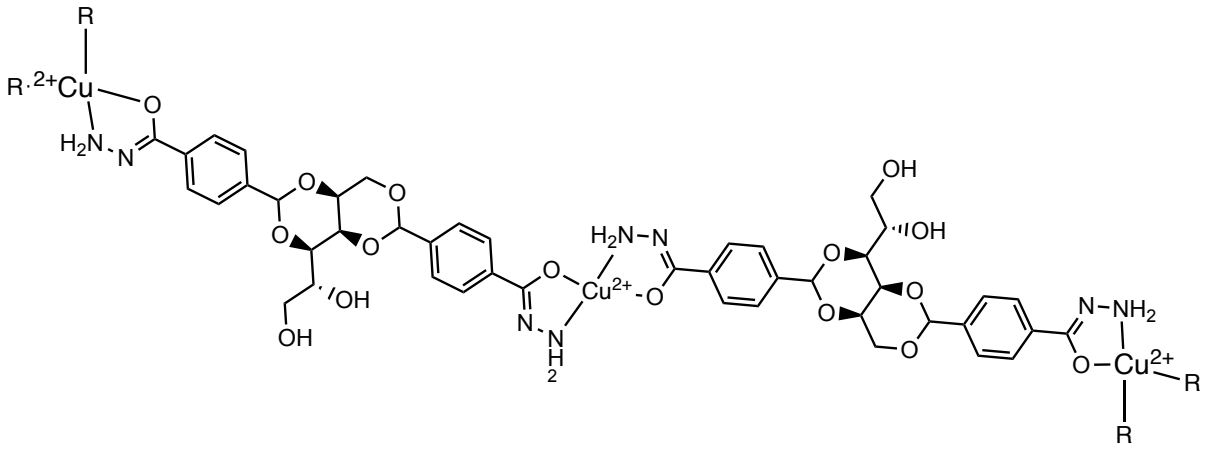

Figure 35: Speculative complex of DBS-CONHNH$_2$ and cupric ions.

The proposed complex would form about the hydrazide group in the DBS-CONHNH$_2$. Dative bonds from the primary nitrogen coordinate to the copper while keto-enol tautomerisation allows for bonding to the copper from the oxygen in its enolic form. This would result in the loss of a proton from the secondary nitrogen. DBS-CONHNH$_2$ would act as a bidentate ligand on each end of the molecule, resulting in the formation of possible 2-dimensional chains of molecules in a manner similar to that observed in 3-dimensional metal-organic frameworks. It is unlikely that one molecule of DBS-CONHNH$_2$ would bend to coordinate about a single cupric ion due to the significant angle strain which would be introduced in this scenario, making it energetically unfavourable.

The formation of this complex would explain a couple of experimental observations when cupric ions were introduced to DBS-CONHNH$_2$ gel. Firstly, the gel was weakened. This was not observed when ferric ions were used. The formation of a complex with the cupric ions would disrupt the supramolecular interactions within the gel. Secondly, a colour change was observed from blue to brown. While this may be indicative of the reduction of the cupric ions to metallic copper, it would also occur in the case of the formation of anhydrous cupric complexes – anhydrous cupric compounds are brown in colour. Additionally, evidence from UV-vis absorbance shows that, of the 0.1 mmol of cupric ions present in the solution, 0.062 mmol moved into the gel. Passive diffusion would account for 0.050 mmol of this total. The remaining 0.012 mmol of cupric ions would have been actively taken into the gel. In 1 mL of 0.4% w/v DBS-CONHNH$_2$ gel, 0.008 mmol of DBS-CONHNH$_2$ is present. According to these results, the complex would have a 1.5:1 Cu:DBS-CONHNH$_2$ ratio. However, when working with concentrations and volumes on this scale, experimental error may lead to slight variations in the results and the true result may be closer to a 1:1 ratio. The experiment should, admittedly, have been repeated twice more in order to achieve concordant results and mitigate human error.

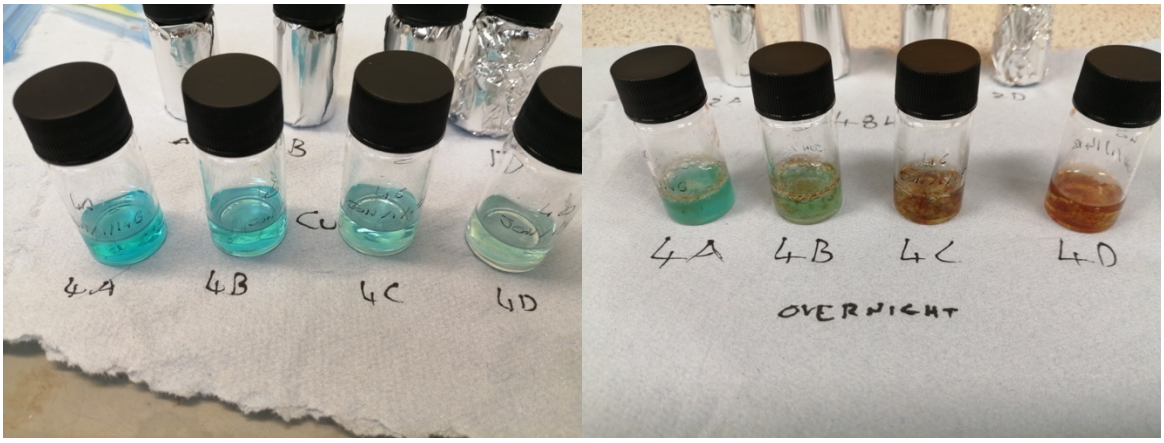

Figure 36: Brown colouration of copper chloride solution when introduced to DBS-CONHNH$_2$ and left for 24 hours. Copper chloride concentrations from left to right in each image: 1.0 M, 0.5 M, 0.25 M, 0.1 M.

The potential formation of nanoparticles was investigated by TEM (see Figure 37). 1 mL of 0.4% w/v DBS-CONHNH$_2$ gels were layered with copper chloride solution and left for 2 days before being submitted for microscopy. It was observed that nanoparticles formed in the gel similarly to the formation of nanoparticles when using ferric chloride. The nanoparticles here were homogenous in shape, all of them being spherical, and polydisperse in size. A control experiment was performed concurrently using 1 mL of alginate gel in place of DBS-CONHNH$_2$, and a multicomponent gel was also prepared. No colour change was observed in alginate, but nanoparticles were observed under TEM analysis.

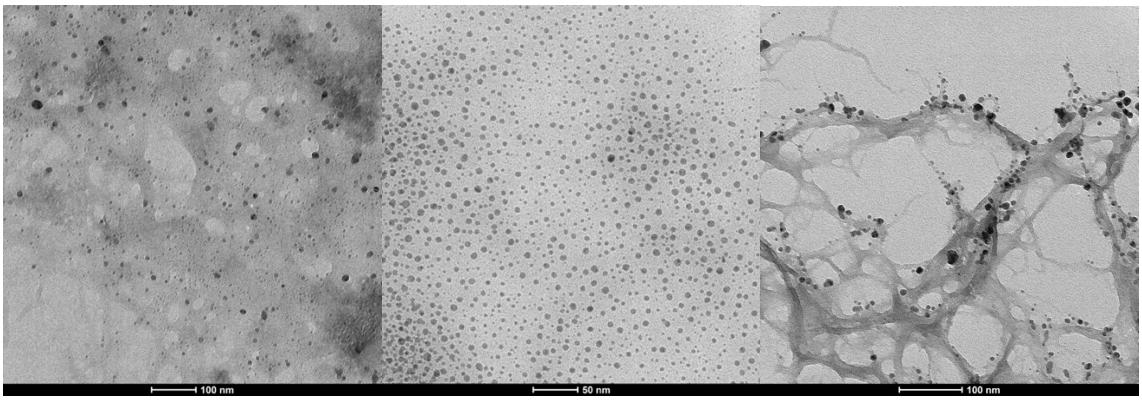

Figure 37: (Left): Image of nanoparticles formed when 1 mL of 0.1 M copper chloride was introduced to 1 mL 0.4 % w/v DBS-CONHNH$_2$. 49,000 x magnification
(Middle): Nanoparticles observed in TEM imaging in copper chloride-doped alginate gel. 98,000 x magnification.
(Right): TEM image of nanoparticles formed in copper-chloride doped multicomponent gel. 68,000 x magnification.

The imaging of nanoparticles is promising, but it does not reveal much about the identity of the nanoparticles. These may be nanosized precipitate clusters of the proposed complex, or they may be metallic copper nanoparticles. Both scenarios are possible if the brown colouration of the mixture after a 48-hour period is taken into consideration. In order to conclusively show the oxidation state of the copper, a sample was prepared for and analysed via XPS in the same manner as the ferric chloride-doped DBS-CONHNH$_2$. Analysis by XPS (see Figure 38) revealed that copper was present exclusively in its cupric state, therefore no reduction had occurred, and the nanoparticles were not metallic copper. The only metallic copper peak observed in the XPS spectrum was a result of X-ray reduction. However, it was also observed that metal-oxygen bonds were not present in the sample, with the only oxygen being organic oxygen. This may, however, be a result of the relatively low amount of copper

compared to the gelator. Any shoulder which may have been observed in the XPS spectrum may simply be too small to be observed.

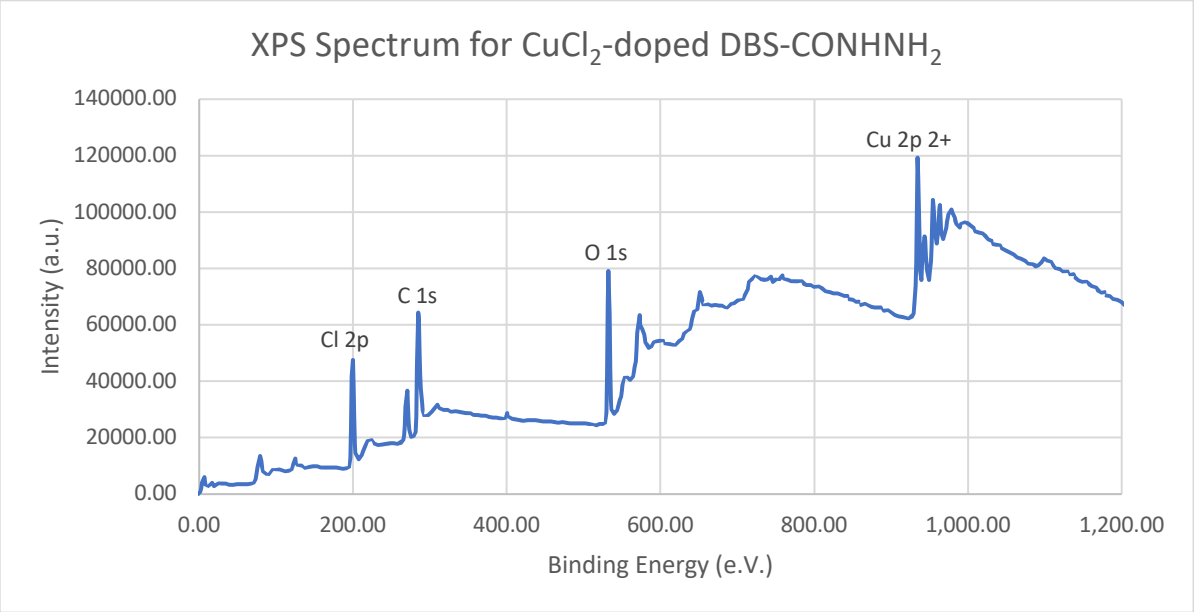

Figure 38: XPS Spectrum for cupric chloride-doped DBS-CONHNH$_2$.

The XPS results indicate that the nanoparticles formed in DBS-CONHNH$_2$ may be copper oxide nanoparticles. The binding energy for Cl 2p is similar to that observed in ferric chloride-doped DBS-CONHNH$_2$, indicating that metal-chlorine bonds may be present here. The formation of nanoparticles in both DBS-CONHNH$_2$ and calcium alginate indicate that DBS-CONHNH$_2$ may not play a specific role in the formation of these nanoparticles. As with ferric chloride-doped DBS-CONHNH$_2$, the exact nature of the nanoparticles is inconclusive, with evidence pointing towards the formation of copper oxide nanoparticles.

Before any applications could be considered, the stability of the nanoparticle-loaded gel needed to be assessed. To this end, rheological studies were conducted to determine to what extent DBS-CONHNH$_2$ is affected and whether multicomponent gel beads can be expected to maintain their stiffness when cupric chloride is introduced. This would be an important step in determining whether using copper-loaded gels in any application is viable; if the gel does not retain its stiffness, then it will be useless in most applications. Therefore, it is hoped that, in a multicomponent gel, alginate will act to retain the stiffness of the gel while DBS-CONHNH$_2$ will interact with the cupric ions. This hypothesis is based upon the experimental findings that alginate is not destroyed by the presence of copper and that DBS-CONHNH$_2$ was shown to interact in some way with the cupric ions.

For the rheological studies, each sample was performed in triplicate in order to achieve concordant results. Therefore, each sample was prepared three times. In short, samples of DBS-CONHNH$_2$ gel, calcium alginate gel, and DBS-CONHNH$_2$ and calcium alginate multicomponent gel were prepared both with and without cupric chloride present. The gels were prepared in bottomless vials which were adjoined to a petri dish using silicone sealant, which is inert to the reagents present. The sealant and bottomless vial could be removed to allow for gel transfer with minimal disturbance of the gel. Therefore, the rheology results

should be accurate representations of the effect of cupric ions and not be affected by damage to the gel during transfer.

For rheological measurements, both amplitude and frequency sweeps were performed. The amplitude sweep applies a range of strains to the gel in stepped amplitude and determines the linear viscoelastic region of the gel; that is, the range of strain which can be applied to a gel without destroying it. The strain is plotted along the x-axis, whilst the storage modulus (G') and the loss modulus (G'') are plotted on the y-axis. The axes are both plotted on a logarithmic scale. A larger storage modulus indicates that more energy is required to be input in order to distort the sample – simply, a stiffer gel will have a larger G' value. In the case where G' > G'' in the linear viscoelastic region, the sample is gel-like in nature whereas if G'' > G' in the linear viscoelastic region, the sample is fluid-like. At a certain strain, a crossover region is observed where, in a gel-like structure, both G' and G'' will drop, but G'' will become greater than G' indicating the structure is destroyed above this strain. A steep drop indicates a brittle break, whereas a smooth drop indicates a more gradual breakdown. Based on the experimental observations, it was believed that DBS-$CONHNH_2$ gel will be much less stiff once it has been exposed to cupric ions due to the breakdown of supramolecular interactions within the gel, whereas alginate gel will retain its gel-like structure because the ionic gelation is unaffected by the cupric ions.

The determination of the linear viscoelastic region by amplitude testing also allows for a frequency sweep to be carried out in this region. A strain value is selected from the linear viscoelastic region and used for subsequent measurements. G' and G'' are measured at a constant strain as a function of frequency (S^{-1}). A low frequency simulates minimal motion whereas a high frequency simulates fast motion. The more frequency dependent G' is, the more fluid-like the material. As with the frequency sweep, it was expected that DBS-$CONHNH_2$ would behave more like a fluid after it had been doped with cupric ions. Alginate gel would be largely unaffected by the presence of the cupric ions.

Initial rheology results indicate that DBS-$CONHNH_2$ is a fairly weak gel with low stiffness (see Figure 39), in line with literature findings.[118] After leaving the linear viscoelastic region, the G' function displays a continuous, steady breakdown which indicates a non-brittle gel which is destroyed homogenously across the structure under strain. A small upturn in the values for G'' after exiting the linear viscoelastic region indicates the point at which the structure begins to rupture, and micro cracks began to appear. Energy is lost around the micro cracks as the fragments are free to move and convert the deformation energy into heat energy as a result of the internal viscous friction. Following this upturn, the crossover region is observed where G'' > G', the point at which the structure ruptures and can be described as a viscoelastic fluid. It should be stated that the error bars on all rheological graphs are calculated as the standard error of each data point from three separate samples.

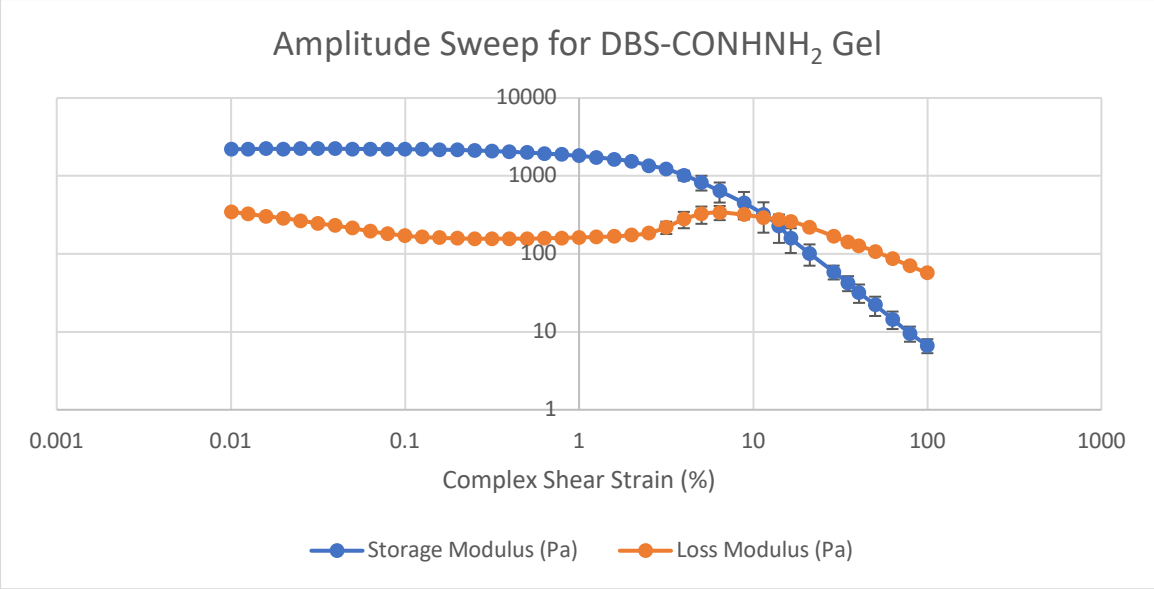

Figure 39: Rheology graph for DBS-CONHNH$_2$ gel.

From the frequency sweep (see Figure 40), it can be seen that G' is independent of frequency across the range investigated, thus DBS-CONHNH$_2$ gel is behaving as a gel. Good concordance of results has generated error bars of minimal size. The results for both the amplitude sweep and the frequency sweep for DBS-CONHNH$_2$ were expected, and the tests were mainly performed as a baseline for comparison after the addition of cupric ions.

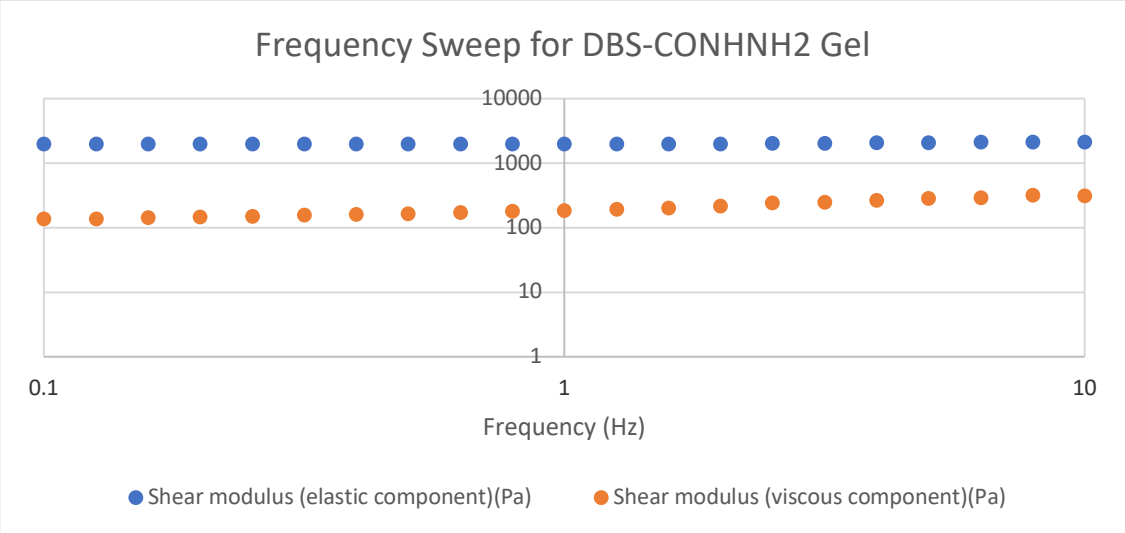

Figure 40: Frequency Sweep for DBS-CONHNH$_2$ Gel.

After being doped with cupric ions, DBS-CONHNH$_2$ is a notably weaker gel (see Figure 41), with G' being much lower than in pure DBS-CONHNH$_2$ gel. Once exiting the linear viscoelastic region, the breakdown here is much less steep, indicating a less brittle structure than that observed in the absence of cupric ions. For the frequency sweep, a new batch of samples was prepared in this case, due to the complete destruction of the gel in the amplitude sweep.

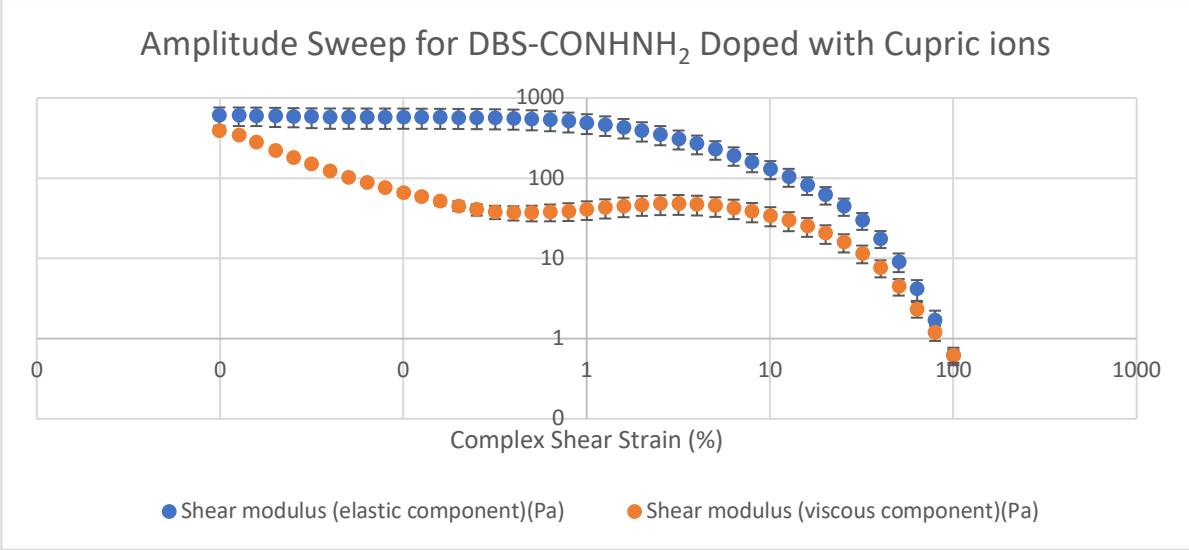

Figure 41: Amplitude sweep for DBS-CONHNH$_2$ doped with cupric ions.

The frequency sweep (see Figure 42) reveals more about the nature of DBS-CONHNH$_2$ once it has been doped with cupric ions. There is some frequency-dependency exhibited by the G', indicating some fluid-like behaviour of the structure. This is in line with experimental observations that DBS-CONHNH$_2$ is degraded to form more sludge-like structure when introduced to cupric ions. Furthermore, the size of the error bars indicates difficulty in achieving concordant results. The exact degree to which DBS-CONHNH$_2$ is degraded by cupric ions appears to be inconsistent, with some samples showing complete degradation and some samples showing only minor degradation. Regardless, the overarching conclusion from this set of data is that DBS-CONHNH$_2$ is weakened by the presence of cupric ions, indicating the disruption of supramolecular interactions and possibly some interaction between DBS-CONHNH$_2$ and these ions.

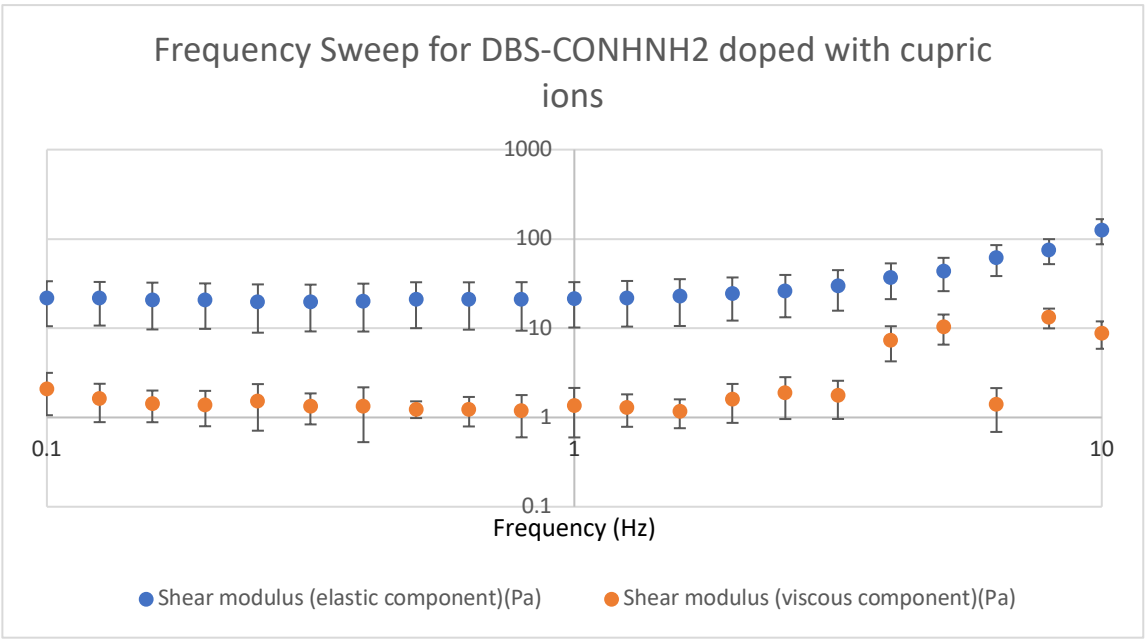

Figure 42: Frequency Sweep for DBS-CONHNH$_2$ doped with cupric ions.

Following this, the rheological properties of alginate both with and without the addition of cupric ions were investigated. Being a polymer gel, alginate should exhibit greater stiffness than DBS-$CONHNH_2$ and should not be weakened by the presence of the cupric ions. There may be the potential for some ion exchange with the calcium in the gel, but the ionic character of the calcium-carbon bond is far greater than copper-carbon due to the differences in electronegativity between the two, meaning calcium-carbon bonds are likely to be stronger than copper-carbon bonds, resulting in ion exchange being enthalpically unfavourable.

The calcium alginate gel was shown to be significantly stiffer than DBS-$CONHNH_2$ (see Figure 43). The same gentle break is observed once the linear viscoelastic region has been left, indicating that the gel is not brittle.

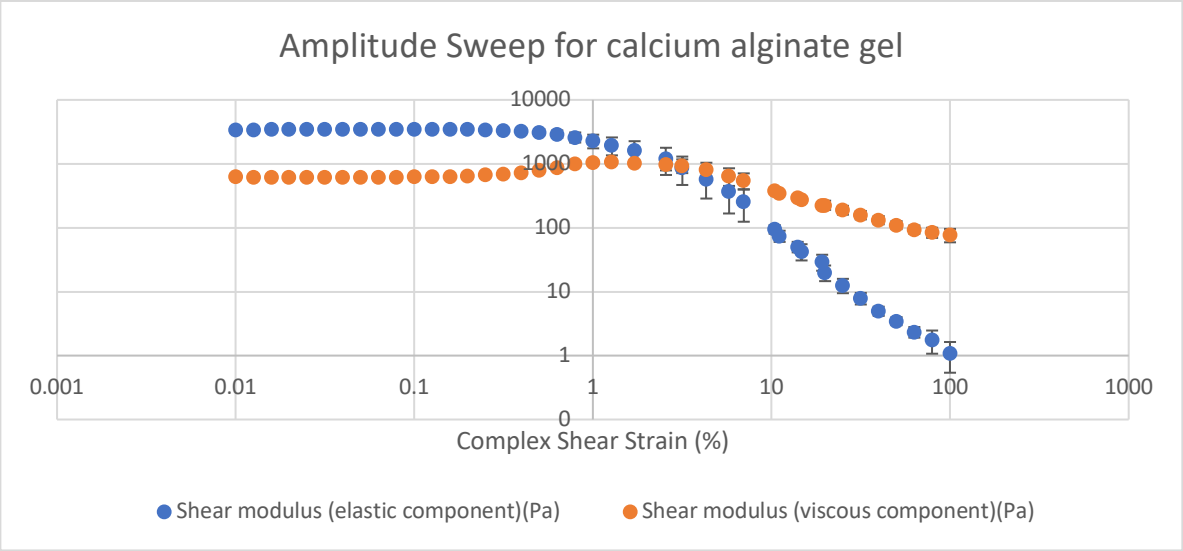

Figure 43: Amplitude sweep for calcium alginate gel.

Much like with DBS-$CONHNH_2$ gel, the G' is largely independent of frequency in calcium alginate gel, confirming that calcium alginate gel is gel-like in its rheological behaviour (see Figure 44). The slightly larger error bars reflect some difficulty in achieving uniform gelation across all three samples, but nonetheless the results are all in agreement that calcium alginate gel is gel-like. Following this, the behaviour of the gel after the addition of cupric ions was explored.

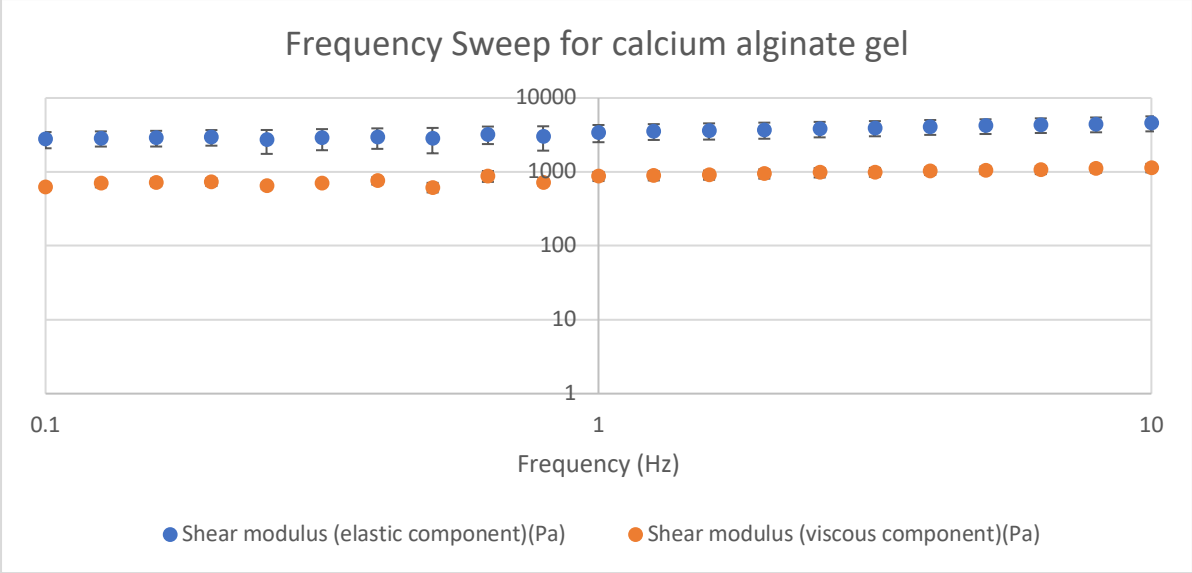

Figure 44: Frequency sweep for calcium alginate gel.

Calcium alginate gel was made slightly stiffer by the addition of these ions (see Figure 45), which is in line with previous studies in the Smith group involving silver ions.[124] The G' is higher than observed in pure calcium alginate gel, and this may be due to the copper nanoparticles which were observed by TEM analysis. They may be acting to increase the stiffness by forming metal precipitates which lower the overall internal viscosity of the gel, thus raising the G' value.

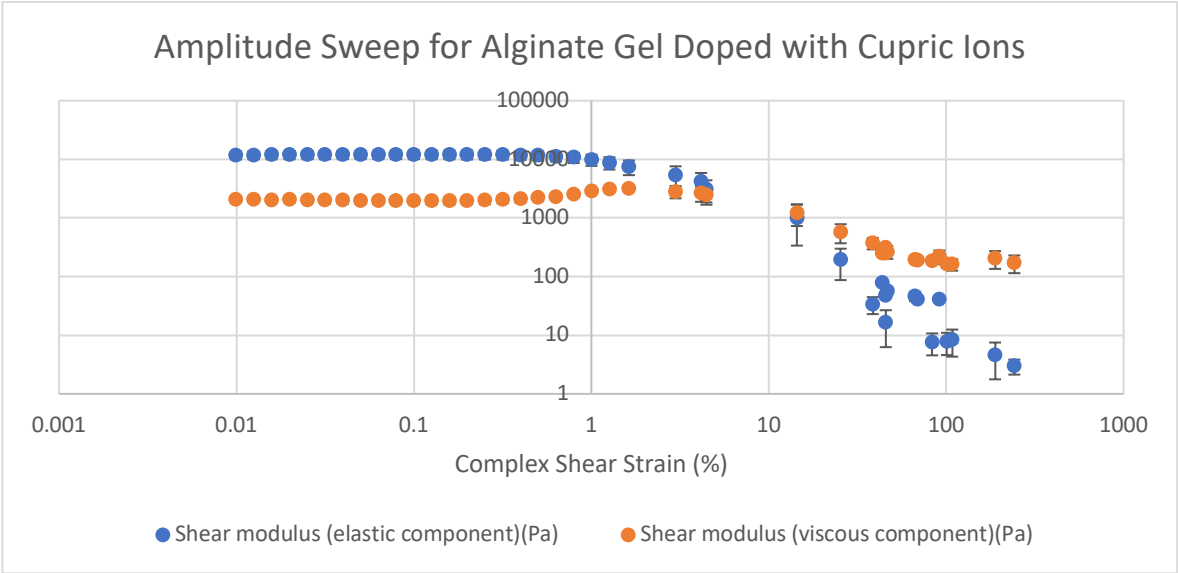

Figure 45: Amplitude Sweep for Calcium Alginate gel doped with cupric ions.

Importantly, the gel retained its frequency independent behaviour in the range tested once it had been doped with cupric ions (see Figure 46). This indicates that the gel retains its gel-like structure in these conditions and no breakdown to a fluid-like state is observed. Following the rheological observations of both DBS-$CONHNH_2$ and calcium alginate both with and without cupric ions, a multicomponent gel consisting of both DBS-$CONHNH_2$ and calcium alginate was formed, and its rheological properties were investigated. It was proposed that, physically, the gel should behave similarly to alginate in that it will retain its stiffness in the presence of cupric ions.

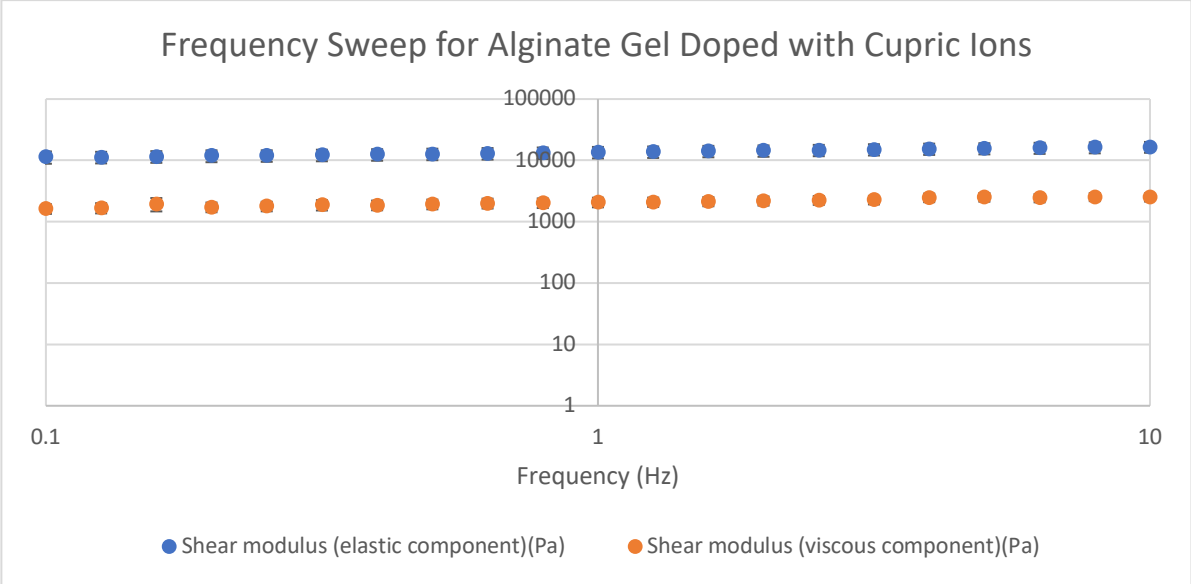

Figure 46: Frequency sweep for calcium alginate gel doped with cupric ions.

The amplitude sweep for the multicomponent gel (see Figure 47) reveals it is similar in stiffness to calcium alginate gel, which is promising for the idea that the gel carries the physical properties of alginate gel and should therefore not be destroyed by the cupric ions. This rheology data is in line with results previously reported in literature.[123]

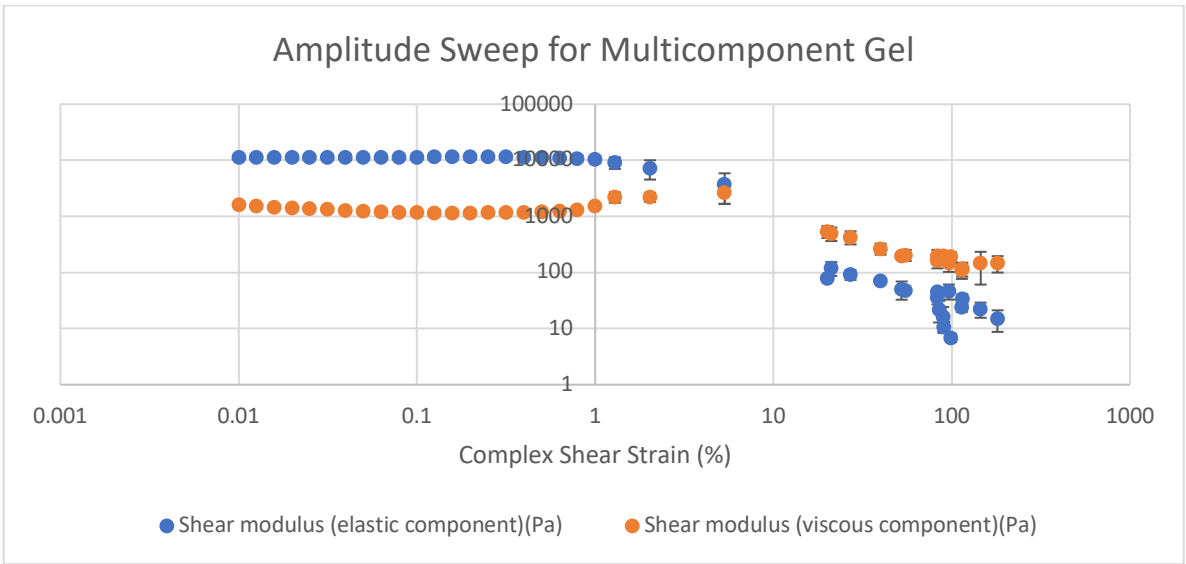

Figure 47: Amplitude Sweep for multicomponent gel.

The frequency sweep for the multicomponent gel (see Figure 48) is in agreement with the amplitude sweep that the gel retains the physical properties of alginate gel. This is promising, and further bolstered the hypothesis that the multicomponent gel should behave like alginate when introduced to cupric ions.

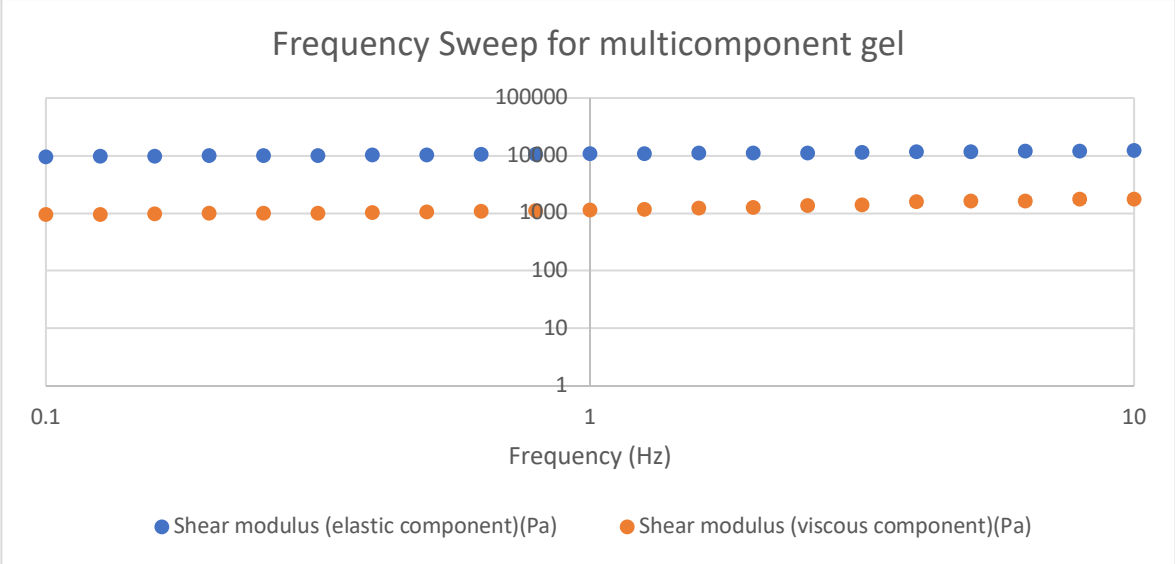

Figure 48: Frequency sweep for multicomponent gel.

The amplitude sweep shows that the multicomponent gel has retained its stiffness in the presence of cupric ions (see Figure 49) in the same nature as observed in calcium alginate gel. The G' has not increased in the same manner as with calcium alginate gel, so it may be that the viscous component of any DBS-$CONHNH_2$ gel which has been made less stiff by the cupric ions is counteracting any increased stiffness introduced by the precipitation of copper nanoparticles.

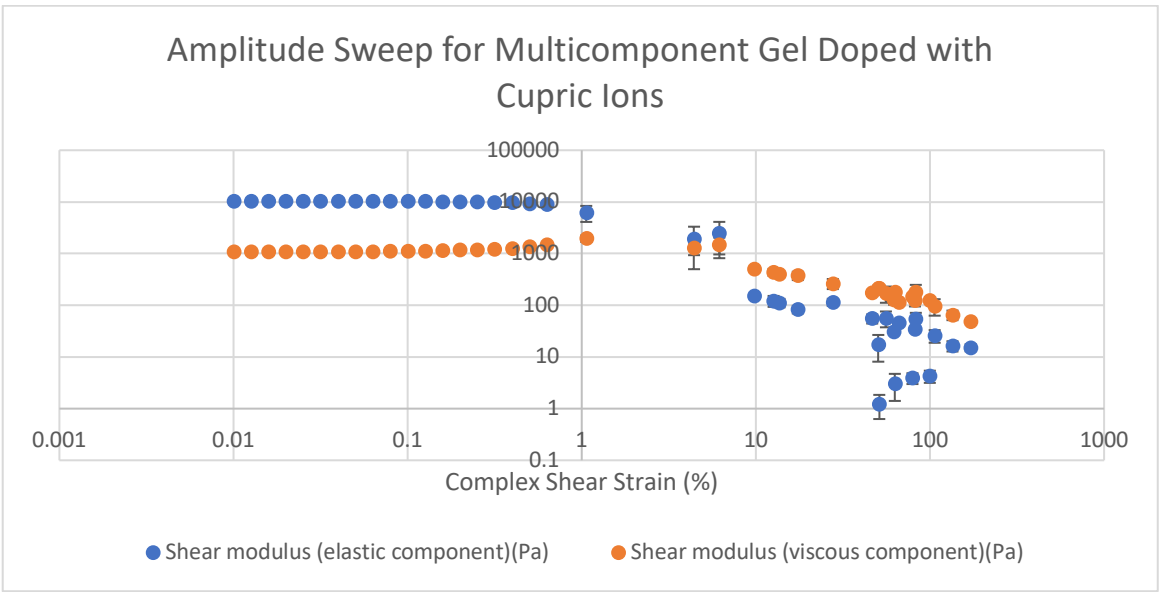

Figure 49: Amplitude sweep for multicomponent gel doped with cupric ions.

The storage modulus for the multicomponent gel doped with cupric ions was independent of the oscillation frequency (see Figure 50). This indicates that, after addition of the cupric ions, the multicomponent gel retains its gel-like structure and the viscous component does not dominate. This is important, as it shows that a multicomponent gel with the rheological properties of alginate gel and the chemical characteristics of DBS-$CONHNH_2$ is stable once it has been loaded with cupric ions and formed copper nanoparticles. This means that multicomponent gel beads should be stable for use in a number of applications.

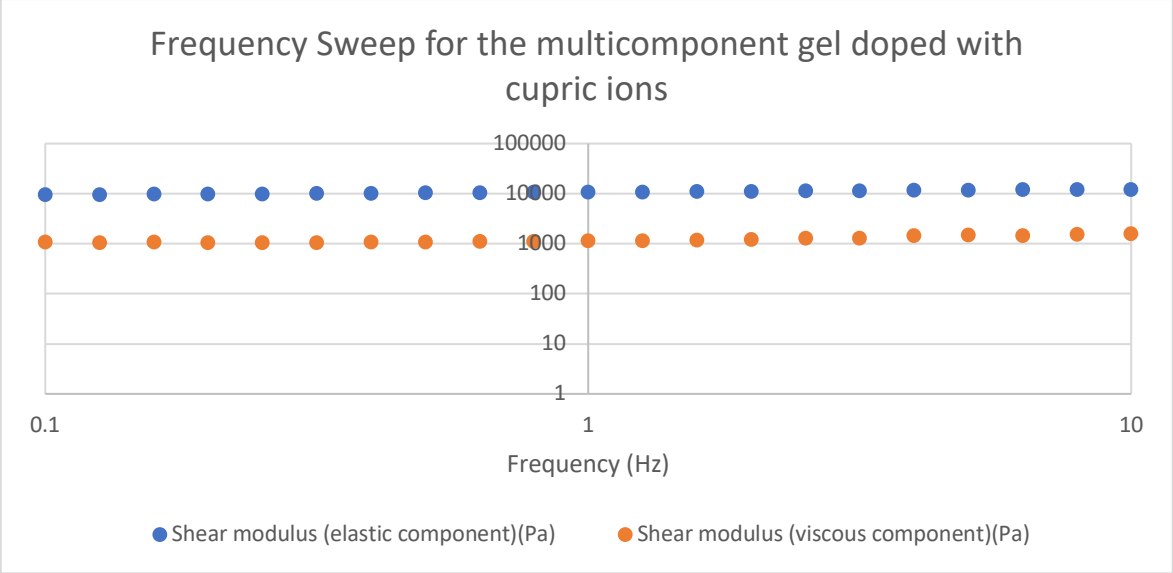

Figure 50: Frequency sweep for multicomponent gel doped with cupric ions.

3.4.3 CuAAC Catalysis with Copper-loaded Beads

Ultimately, catalysis was chosen as the possible application for copper-loaded multicomponent gel beads. To this end, the copper(I)-catalysed azide-alkyne cycloaddition (CuAAC) reaction was chosen as the reaction. This is a single step click reaction which is biologically relevant and finds use in medicinal chemistry, for example in the synthesis of the β-lactamase inhibitor tazobactam.[138] However, common problems with using copper salts such as copper sulfate include inability to remove the copper from the reaction mixture and subsequent copper contamination of the product. It was hypothesised that the beads could be added to a CuAAC reaction and catalyse the reaction without producing copper-contaminated product. The beads could ideally be removed from the system and re-used multiple times before catalytic activity was reduced. It should also be noted that, despite the reaction being termed 'copper(I)-catalysed', it is far more successful when using a copper(II) material in the presence of a reducing agent such as sodium ascorbate to produce copper(I) *in situ*, hence it was though that Cu(II) loaded beads could be an ideal source of copper for this type of reaction.

In this case, an adjustment of the CuAAC reaction first reported by Sharpless *et al.*[139] was proposed. Sodium hydrazide was replaced with 2-azido-2-deoxy-*D*-glucose due to safety concerns, and was reacted with phenylacetylene at a 1:1 molar ratio:

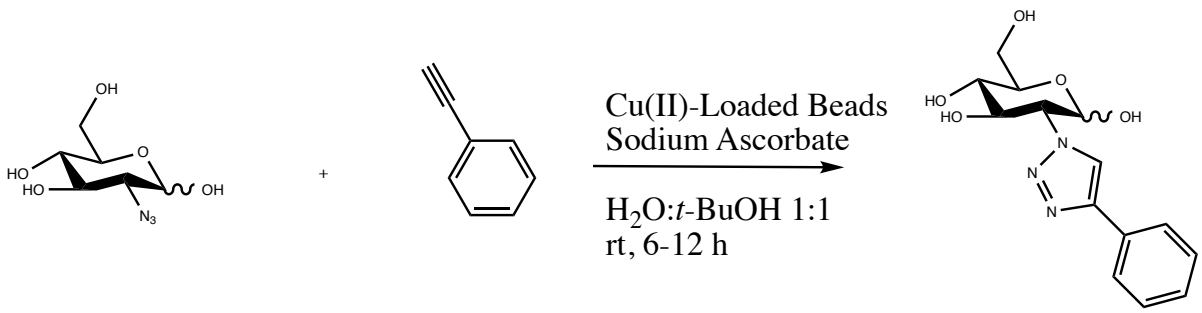

Figure 51: Proposed scheme for the CuAAC reaction.

For this reaction, multicomponent gel beads were formed on the millimetre scale. These beads were placed in copper chloride solution for 2 days before being washed and stored in water. It was noticed that the core of these beads had turned brown, while the shell remained light blue in colouration. This indicates that the cupric ions had precipitated as nanoparticles in the DBS-$CONHNH_2$ core and were stabilised within the gel bead. It was hoped that the reagents would enter the bead, perform the catalysed reaction, and then be flushed out of the bead to yield product with minimal copper contamination.

A control reaction was performed using copper sulfate solution in place of the copper-loaded beads to ensure the reaction did indeed proceed. No literature precedent using these exact reagents in a CuAAC reaction could be found, so this needed to be tested beforehand. The reaction was monitored by TLC analysis using a 1:1 mixture of hexane and ethyl acetate, imaging the phenylacetylene under UV light. Upon addition of the copper sulfate solution, the reaction changed from colourless to straw-yellow, indicating reduction of the copper. After being left to react overnight, the reaction was checked and complete consumption of phenylacetylene was confirmed by TLC analysis, indicating the reaction had taken place. The product itself, being novel, was difficult to isolate and purify. Once the product had been isolated as green crystals, it quickly forms a red sludge on exposure to air. It was extremely hygroscopic and insoluble in organic solvents. It was therefore decided that the identity of the product was not to be pursued, as the main focus was the catalysis of the reaction. Further investigation of the reaction would have been carried out. However, due to limited lab time, this was not conducted. Following this, the reaction was attempted in the absence of copper sulfate. After being allowed to react overnight, phenylacetylene was still observed in the reaction mixture in TLC. This confirms that, not only does the reaction proceed, but it only does so in the presence of a copper catalyst.

Copper-loaded multicomponent gel beads were added to the reaction process in place of copper sulfate. All other reaction conditions were kept the same. Upon addition of the beads, the core changed colour from a brown to a dark orange as in the ideal reaction. Over the period of an hour, the reaction mixture itself began to slowly change to the orange colouration observed within the bead, indicating the release of copper. Promisingly, after being allowed to react overnight, TLC analysis confirmed the consumption of phenylacetylene, and a reaction had therefore occurred. However, the beads had been destroyed in the process and were no longer present in the reaction mixture the following day. This observation would explain the release of copper into the reaction mixture.

In order to investigate the breakdown of the beads, a set of multicomponent gel beads were stirred in a 1:1 v/v mixture of water and *tert*-butanol overnight. It was not believed that the stirring action would destroy the beads, as alginate is a relatively stiff polymer gel and therefore resistant to destruction by physical means of the same strength as being stirred in solution. It was noticed that the beads were destroyed in this test, indicating that *tert*-butanol is causing the destruction of the beads. This was removed from the next attempt at the CuAAC reaction, which was performed in entirely aqueous conditions. This should not be a problem for the reaction itself, as reagents which are partially insoluble will be gradually dissolved as they are reacted to form product. Unfortunately, it was again noticed that the beads were destroyed in the reaction.

In a follow-up investigation, the beads were stirred in water with the reducing agent sodium-*L*-ascorbate. Here, it was noticed that the beads were destroyed. It is likely that sodium-*L*-ascorbate is scavenging calcium ions from the alginate gel, causing the ionic gelation model to breakdown and ultimately destroy the gel. This was a frustrating discovery, as many other reducing agents would likely interact with DBS-$CONHNH_2$, meaning there was little recourse to salvage this specific experiment. One manner in which this problem could be solved would be to use a different polymer gel which is not affected by sodium-*L*-ascorbate and would therefore be able to survive the experiment.

Nonetheless, this line of investigation has yielded some useful insights. Copper(II)-loaded multicomponent gel beads in which the supramolecular gel has formed nanoparticles have successfully been fabricated. These beads have been shown by rheological studies to possess the stiffness of calcium alginate, meaning they have the potential to be added to reactions and subsequently removed, washed, and reused. A lot more work could be done to optimise the use of Cu(II)-loaded hybrid hydrogel beads in click chemistry. Changing the polymer gelator to one such as agarose may prevent destruction of the beads. While a successful path may not be forged using cupric ions, other ions such as cobalt(II), nickel(II), or silver(II) may yield far greater results.

4. Conclusions and Further Work

Overall, the project may be described as a moderate success which still needs work in order to reach definite conclusions. Multicomponent gel beads were successful fabricated in sizes significantly smaller than prior to the project, and the controlling factor – the viscosity of the oil phase – was identified. This result alone is enough to state there is some success in the project, the correlation between oil-phase viscosity and bead size will allow for the fabrication of beads of specific sizes in future for different applications; beads between 200 – 1000 nm may find use in oral drug delivery. It must, of course, be remembered that this is just the beginning of the project, and that much work is still required before it can be concluded.

With the metal-doped gels, interesting observations were made, but no successful route of investigation was found. When copper was used, metal nanoparticles containing cupric ions were formed, but no application was found for these. Their use as catalysts in a CuAAC reaction was explored, but the multicomponent gel bead in which they were encapsulated was destroyed during the experiment due to the action of the reducing agent. The gels which contained iron were found to form iron oxide species, but a majority of the iron remained as molecular iron chloride bound to the gel, as shown by XPS.

There is clear scope for substantial further development of the methodology and application of multicomponent gel beads. Relatively, this work is still in its infancy; low yields of product and inability to produce electron microscopy images have hampered the progression of this work. There are possible solutions to this, which may potentially lead to further studies in uptake and release of pharmaceutical agents, and subsequent studies into the efficacy of the beads.

Initially, yields may be improved through greater centrifugation of the mixture obtained in the fabrication process. Unfortunately, the centrifuge available would not achieve rotation rates greater than 3990 rpm. By applying Stokes' Law of centrifugation, this would apply a gravitational force of 2580.81 m s^{-2} to the particles in the centrifuge tube. Spherical particles of 200 nm in diameter would reach of velocity of 2.84 nm s^{-1} in the medium used in this process. This means that, theoretically, the sample needs to be centrifuged for 4702.55 minutes – or 3.27 days – in order to achieve complete sedimentation of all particles 200 nm in diameter. If the rotation rate were increased to 15,000 rpm, this would be reduced to 5.55 hours. While not ideal, this is a drastic improvement on the current method. Furthermore, this would only be necessary if a 100 % yield is absolutely required; less time may be taken if a lower yield is acceptable. Further purification methods could also be explored, such as dialysis.

The main barrier to imaging the beads was the type of filter available for electron microscopy. The lowest size filter available was 400 nm, meaning that any beads with a lower diameter than this were simply lost in the washing process. Any methods which required the drying of the beads prior to imaging resulted in aggregation of the beads and a large mass of gel being observed. An ideal solution would be to use filters with pore sizes lower than the desired bead size, retaining the beads for imaging. Another possible solution may be to use atomic force microscopy (AFM) to image the beads in liquid medium. Successful imaging of the nanosized beads is essential evidence for the furthering of this project. This process would also need to

be conducted with the iron oxide nanoparticle-containing beads, to provide proof that the beads themselves contain magnetic nanoparticles.

Following this, the core-shell nature of the beads needs to be proven. On a larger (millimetre) scale, this can be shown by cutting a bead in half and observing an interface between the alginate shell and the DBS-$CONHNH_2$ core. On the nanometre scale, this is simply not possible. One way in which the core-shell nature may be shown would be through small-angle neutron scattering (SANS). This may possibly work by using a deuterated solution of calcium chloride when triggering the gelation of alginate, which would hopefully result in a deuterated shell. This would create contrast between the core and the shell when probing the structure with SANS, allowing for differentiation between the two.

Upon improving the yield and confirming the structure of the beads, the core:shell ratio should be confirmed. This should be done via elemental analysis in order to ascertain the amount of both alginate and DBS-$CONHNH_2$ in the bead. From this, the thickness of the shell could be calculated and tuned in subsequent fabrication methods by either using more or less alginate to induce a thicker or thinner shell, respectively. This may help to tune the physical properties of the bead. A thicker shell, for example, would likely result in greater stiffness and improved longevity of the beads but possibly at the loss of some drug loading into the DBS-$CONHNH_2$ core in a drug delivery scenario.

The magnetic properties of beads containing iron oxide nanoparticles would need to be determined. Ideally, a portion of a sample would be imaged to show iron oxide nanoparticles are embedded in the beads rather than in suspension around the beads. Following this, magnetometry measurements would be conducted to ascertain the magnetic susceptibility of the beads. This would be important for future applications such as targeted drug delivery, as knowing the magnetic susceptibility would allow for the determination of a minimum required strength of an applied magnetic field to induce movement in the beads.

Possible applications of the multicomponent gel beads would also be explored in future work. Chiefly, the ability of the beads to act as drug delivery vehicles would be explored with the use of an anti-cancer agent. The choice of drug would rely heavily on its hydrophilicity, with more hydrophilic drugs being favourable as they would be easier to load into the beads in the reverse-emulsion method. One possible drug which may be used for this investigation would be gemcitabine, a hydrophilic and low-cost anti-cancer agent used in the treatment of a wide range of carcinomas. Uptake and release studies would need to be conducted in order to ascertain the effectiveness of the beads as a drug delivery vehicle for this specific drug, as well as rheological studies to determine the effects gemcitabine would have on the gels at various concentrations. Once drug-loaded beads have been fabricated, *in vitro* studies would need to be conducted to study the cytotoxicity of the beads, before possible *in vivo* studies.

Once this has been done using non-magnetic beads as a ‘proof-of-concept’, iron oxide nanoparticles will be introduced to the procedure. Ideally, this would fabricate nanosized multicomponent gel beads containing magnetic nanoparticles and an anti-cancer drug. DLS, electron microscopy, rheology, and UV-vis measurements would be taken to determine the size, structure, stiffness, and drug loading, respectively, of the beads. After this, *in vitro* studies would be conducted to determine whether a magnetic field of suitable strength can

direct the nanosized beads through tissue to a target area. This would ideally reduce off-target effects by concentrating the release of the drug at a target area, or at least increasing the rate at which the beads reach a target area. By applying an alternating magnetic field to the beads, magnetic hyperthermia should be observed, raising the temperature around the target site to around 46℃ resulting in cell death. Concurrently, this increase in temperature may lower the stiffness of the DBS-$CONHNH_2$, releasing the anti-cancer agent at a higher rate than at a lower temperature. Summarily, this would hopefully result in a dual-action drug-delivery vehicle capable of targeted delivery, which is biocompatible and relatively simplistic to fabricate.

As a possible alternative project, the interaction between DBS-$CONHNH_2$ and metal salts could be studied further. The ability of copper-laden multicomponent gel beads to catalyse reactions such as the CuAAC reaction could be further investigated by using a polymer gel other than alginate, such as agarose. Ideally, these beads would not be destroyed by the presence of the reducing agent, and the reaction would proceed with minimal copper contamination of the product. However, as DBS-$CONHNH_2$ proved unable to reduce copper to its cuprous state, its presence in this system may be superfluous. If the catalytic ability of the copper nanoparticles formed by the gel is greater than a system using free solutions of copper, then DBS-$CONHNH_2$ would indeed be useful in this reaction, as it would concurrently reduce copper contamination and increase catalytic ability.

Overall, this project has opened up myriad possibilities for further investigation. DBS-$CONHNH_2$ is a versatile gelator which may have a future in biomedical research for drug delivery, or in catalysis chemistry owing to its interactions with metallic ions. There is, of course, a long way and a lot of research to go before this is realised, but the potential is undeniable.

5. Experimental Section

Dynamic light scattering (DLS) experiments were performed on a Malvern Zetasizer Nano Series from Malvern Instruments Ltd., UK, and results were processed using the Zetasizer software application V. 7.01. Sample measurements were performed at 25 ℃ using back-scattered light fluctuations at 173 °. Measurements were performed in triplicate, with sonication of the sample between measurements to counteract sedimentation. 13 runs were performed with each measurement and the mean values were calculated and graphed by the software. All bead samples were measured in water. When filtering, a 450 nm nylon filter was used.

UV-Vis measurements were performed using a Shimadzu UV-2401PC spectrophotometer with Standard Personal Spectroscopy Software installed. Samples were presented in a glass cuvette.

^{1}H NMR experiments were conducted using a JEOL JNM-ECS400a at a frequency of 400 MHz spectrometer and data was analysed using MestReNova software version 14.1.0-24037. Samples were presented in a Norrell S400 NMR tube.

Rheology was conducted using a Malvern Instruments Kinexus Pro+ rheometer from Malvern Panalytical. All measurements were performed at 25 ℃.

Samples for electron microscopy were submitted to the microscopy service in the Department of Biology at the University of York. TEM was performed using a FEI Tecnai 12 G2 equipped with CCD camera. SEM was performed using a JEOL JSM-6490LV electron microscope.

Samples for x-ray photoelectron spectroscopy were submitted to the XPS analysis service in the Cardiff Catalysis Institute at the University of Cardiff and analysed by a Shimadzu Kratos Axis Ultra-DLD.

Synthetic procedures were carried out without further purification of the materials used.

5.1 Synthesis of DBS-CONHNH$_2$

Synthesis of DBS-CO$_2$Me. D-Sorbitol (5.103 g, 28.01 mmol) was added to a cyclohexane (70 mL) and methanol (40 mL) mixture under stirring at 50 °C. 4-methylcarboxybenzaldehyde (7.497 g, 45.60 mmol) and *p*-Toluenesulfonic acid (*p*-TsOH) (1.037 g, 6.022 mmol) were added to methanol (50 mL) and stirred until complete dissolution was observed. This solution was then added dropwise to the *D*-Sorbitol solution under Dean-Stark conditions. Following complete addition, the temperature was raised to 70 °C and left for 2 hours. The product, a white paste, was filtered under vacuum and washed with ice cold methanol (2 x 60 mL), boiling water (3 x 100 mL), and dichloromethane (3 x 100 mL) before being dried and collected. Yield: 28% (3.552 g, 7.60 mmol). ^{1}H NMR (400 MHz, DMSO-d_6): δ 7.98-7.92 (m, 4H, aromatic *H*), 7.63-7.54 (m, 4H, aromatic *H*), 5.73 (s, 2H, aromatic C*H*), 4.93 (d, 1H, CHO*H*), 4.47 (br, 1H, CH$_2$O*H*), 4.23-4.14 (q, 3H, sugar (overlap)), 3.98 (s, 1H, sugar), 3.86 (d, 1H, sugar), 3.81 (s, 6H, OC*H*$_3$), 3.75 (br, 1H, sugar), 3.61-3.58 (m, 1H, sugar), 3.51-3.48 (m, 1H, sugar). ESI-MS (m/z) calculated for $C_{24}H_{26}O_{10}$ 474.152, found 475.160 (100% $[M+H]^+$). υ_{max} (cm^{-1}): 2956, 1724, 1435, 1399, 1276, 1167, 1094, 1018, 856, 835, 750, 709.

Synthesis of DBS-CONHNH$_2$. DBS CO_2Me (1.125 g, 2.373 mmol) was dissolved in THF (50 mL) followed by the addition of hydrazine monohydrate (8 mL, 164.9 mmol). This mixture was heated to 70 °C under reflux and allowed to react overnight. The resulting white paste was filtered under vacuum and washed with water (5 x 80 mL) before being dried and collected as a white powder. Yield: 64% (0.720 g, 1.52 mmol). ^{1}H NMR (400 MHz, DMSO-d_6): δ 9.77 (s, 2H, CON*H*NH$_2$), 7.80-7.77 (m, 4H, aromatic *H*), 7.50-7.46 (m, 4H, aromatic *H*), 5.68 (s, 2H, aromatic C*H*), 4.90-4.88 (d, 1H, CHO*H*), 4.45 (s, 2H, CONHN*H*$_2$), 4.45-4.41 (t, 1H, CH$_2$O*H*), 4.20-4.12 (q, 1H, sugar), 4.14 (s, 1H, sugar), 3.95 (s, 1H, sugar), 3.85-3.82 (d, 1H, sugar), 3.75-3.70 (m, 1H, sugar), 3.61-3.56 (m, 1H, sugar), 3.45-3.40 (m, 1H, sugar). ESI-MS (m/z) calculated for $C_{22}H_{27}N_4O_8$ 474.18, found 475.18 (100% $[M+H]^+$). υ_{max} (cm^{-1}): 3293, 2869, 1634, 1569, 1093.

5.2 Synthesis of Iron Oxide Nanoparticles

Ferrous chloride tetrahydrate (1.51 g, 7.6 mmol) and ferric chloride (3.02 g, 18.6 mmol) were added to distilled water (100 mL) and stirred under nitrogen for 3 hours at room temperature. Sodium *n*-dodecyl sulfate (0.226 g, 0.78 mmol) was dissolved in ammonium hydroxide (10 mL, 35%) by stirring vigorously for 1 hour. This solution was injected via syringe into the iron solution to immediately yield a black precipitate. The product was filtered under vacuum and washed with distilled water (5 x 50 mL) before being dried under vacuum and collected. Yield 97% (1.721 g, 7.4 mmol).

A 1mg/mL suspension of nanoparticles was produced by adding iron oxide (5 mg) to water (5 mL) and sonicating for 1 hour.

When poly(ethylene glycol) was used as the capping agent, ferrous chloride tetrahydrate (1.504 g, 7.565 mmol) and anhydrous ferric chloride (3.024 g, 18.64 mmol) were added to water (100 mL) and stirred under nitrogen at 60 °C for 4 hours. Poly(ethylene glycol) (0.094 g, 0.012 mmol) was dissolved in water (10 mL) before being injected into the hot solution. This was followed by injecting ammonium hydroxide (10 mL, 35%, 87.90 mmol) into the solution. The product was filtered under vacuum and washed with water (5 x 100 mL) before being allowed to air dry overnight. It was then washed with ethanol (200 mL) before being dried under vacuum and collected. Yield 97% (1.701 g, 7.347 mmol).

5.3 Fabrication of DBS-CONHNH$_2$/Alginate Multicomponent Gel Beads

5.3.1 Fabrication in Paraffin Oil

DBS-CONHNH$_2$ (3.00 mg, 0.006 mmol) was added to water (0.5 mL) and sonicated to form a uniform suspension. To this suspension, sodium alginate solution (1% wt/vol, 0.5 mL) was added, and the mixture was heated using a heat gun to form a colourless, transparent solution. This solution was dropped (20 µL/drop) over a 2-minute period into paraffin oil (40 mL) and Span80 non-ionic surfactant (0.8 mL) under vigorous stirring. This mixture was allowed to stir for 1 hour. Calcium chloride (5% wt/vol, 1 mL) was then dropped into the mixture to initiate the gelation of alginate and allowed to stir for a further 20 minutes. The mixture was centrifuged at 3990 rpm for 5 minutes, with the supernatant being discarded afterwards. This was repeated 3 times using petroleum ether, 3 times using ethanol, and 3 times using distilled water before storing the sample in water (1 mL) and sonicating for 30 minutes.

The beads were characterised using DLS analysis, IR spectroscopy, and ^{1}H NMR spectroscopy and imaged using electron microscopy.

When investigating the effect of the volume of the oil phase, the volume was increased to 200 mL of paraffin oil and 4 mL of Span80. The volume of gelator used was kept constant. Centrifugation in this case was repeated until the entirety of the paraffin oil had been centrifuged (10 times) before the regular washing procedure was conducted.

When the effect of temperature on the formation of the beads was investigated, paraffin oil (40 mL) was heated to 95 °C before the aforementioned method was carried out. The mixture was allowed to cool to room temperature after the 20-minute stirring step before centrifugation.

When investigating whether sonication induces the formation of smaller beads, the use of a magnetic stirrer was replaced with a sonic bath. All other parameters were kept constant.

5.3.2 Fabrication in lower viscosity oil phases

DBS-$CONHNH_2$ (3.00 mg, 0.006 mmol) was added to water (0.5 mL) and sonicated to form a uniform suspension. To this suspension, sodium alginate solution (1% wt/vol, 0.5 mL) was added, and the mixture was heated using a heat gun to form a colourless, transparent solution. This solution was dropped (20 µL/drop) over a 2-minute period into a mixture containing the oil phase (either ethyl acetate, *n*-butyl acetate, amyl acetate, heptane, or hexane, 40 mL) and the non-ionic surfactant Span80 (0.8 mL) under vigorous stirring using a cross-stirrer bar. To this mixture, glycerol (1 mL) was added and stirred for 10 minutes. Calcium chloride 5% wt/vol, 1 mL) was then dropped into the mixture to initiate the gelation of alginate and allowed to stir for a further 5 minutes. After being removed from the stirrer, the mixture was transferred to a separating funnel, and the glycerol layer was collected while the oil phase was discarded. The glycerol layer was transferred to a centrifuge tube and diluted to 10 mL with ethanol. The mixture was centrifuged at 3990 rpm for 10 minutes. The supernatant was discarded, and the centrifugation was repeated with ethanol twice more, and then three times with distilled water. After the final wash, the sample was stored in distilled water (1 mL) and sonicated for 30 minutes.

5.4 Metal ion uptake study

5.4.1 Ferric chloride

Ferric chloride (0.1640 g) was dissolved in water (10 mL) to form a 0.1 M stock solution which was stored in a sealed container.

Potassium thiocyanate (0.0973 g) was dissolved in water (10 mL) to form a 0.1 M stock solution.

A series of dilutions of ferric chloride (0.05 mL) of 0.1 M, 0.05 M, 0.025 M, 0.0125 M, and 0.0 M was prepared, to which an equal volume of equal concentration potassium thiocyanate was added. This blood-red complex was diluted to 2 mL and the absorbance at 450 nm was measured using a UV-vis spectrometer.

DBS-$CONHNH_2$ (4.00 mg, 0.008 mmol) was suspended in water (1 mL) and heated to form a colourless solution. This solution was allowed to cool to form a colourless gel. Ferric chloride solution (0.1 M, 1 mL) was gently layered on top of the gel. An aliquot of the solution (0.05 mL) was taken at regular time intervals and complexed with potassium thiocyanate (0.1 M, 0.05 mL) before being diluted to 2 mL with water. The absorbance of the solution was measured at 450 nm.

5.4.2 Cupric chloride

Cupric chloride (0.1340 g) was dissolved in water (10 mL) to form a 0.1 M stock solution.

A series of dilutions of cupric chloride (0.1 mL) of 0.1 M, 0.05 M, 0.025 M, 0.0125 M, and 0.0 M was prepared. These were diluted to 2 mL and the absorbance at 800 nm was measured.

DBS-$CONHNH_2$ (4.00 mg, 0.008 mmol) was suspended in water (1 mL) and heated to form a colourless solution. This solution was allowed to cool to form a colourless gel. Cupric chloride (0.1 M, 1 mL) was gently layered on top of the gel. An aliquot of the solution (0.1 mL) was taken at regular time intervals and diluted to 2 mL with water. The absorbance of the solution was measured at 800 nm.

5.5 Formation of metal nanoparticles in gels.

Ferric chloride (1.625 g) was dissolved in water (10 mL) to form a 1.0 M stock solution.

Cupric chloride (1.352 g) was dissolved in water (10 mL) to form a 1.0 M stock solution.

DBS-$CONHNH_2$ (4.00 mg, 0.008 mmol) was suspended in water (1 mL) and heated to form a colourless solution, which was then allowed to cool and form a gel. This was repeated 16 more times to produce a total of 17 individual vials of 0.4% wt/vol DBS-$CONHNH_2$ gel. The first of these served as a control. To 8 of these vials, ferric chloride solution (1 mL) of a series of concentrations (1.0 M, 0.5 M, 0.25 M, 0.1 M, 0.05 M, 0.025 M, 0.0125 M, and 0.005 M) was added. The vials were covered in foil and left for 48 hours. This was repeated with the remaining 8 vials using cupric chloride.

The most distinct colour change was observed in the 0.1 M and 0.05 M solutions of cupric chloride thus these were chosen as the most hopeful candidates in both series of metals for viewing under SEM and TEM. Excess liquid was removed using a glass pipette and the samples were submitted for electron microscopy with no further modification.

Calcium alginate gels were formed using sodium alginate (1%, 0.8 mL) and water (0.2 mL). To this, calcium chloride (5%, 1 mL) was added. After gelation, excess liquid was removed and replaced with either cupric chloride (0.1 M or 0.05 M, 1 mL) or ferric chloride (0.1 M or 0.05 M, 1 mL). These samples were left for 3 days before excess liquid was removed and the samples were submitted for SEM and TEM.

Multicomponent gels were formed using a both DBS-$CONHNH_2$ and alginate. For these gels, DBS-$CONHNH_2$ (3.00 mg, 0.006 mmol) was added to water (0.5 mL) and sonicated to form a uniform suspension. Sodium alginate (0.5 mL) was then added, and the mixture was heated using a heat gun before being allowed to cool and gelate. Calcium chloride (5%, 1 mL) was

then added. After one day, excess liquid was removed and replaced with either cupric chloride (0.1 M or 0.05 M, 1 mL) or ferric chloride (0.1 M or 0.05 M, 1 mL). These samples were left for 3 days before excess liquid was removed and the samples were submitted for SEM and TEM.

Twelve vials of DBS-$CONHNH_2$ gel (0.4% wt/vol, 1 mL) were prepared. To six of these, ferric chloride (0.1 M, 1 mL) was added. To the other six, cupric chloride (0.1 M, 1 mL) was added. These were wrapped in foil and left for 2 days before being dried under vacuum and collected for XPS analysis.

5.7 Preparation of Gels for Rheology

DBS-$CONHNH_2$, calcium alginate, and multicomponent gels were prepared in triplicate in 6 mL bottomless vials. The vials were sealed onto petri dishes using silicone sealant to prevent leakage before gel formation.

Nine vials of DBS-$CONHNH_2$ gel were formed through the previously described method. Three of these were left unaltered before rheology measurements were obtained. To the other six, cupric chloride (0.1 M, 1 mL) was added, and the vials were left for 2 days before rheology.

Nine vials of calcium alginate gel were formed by adding calcium chloride (5%, 1 mL) to sodium alginate (1%, 0.8 mL) and water (0.2 mL). These nine were separated and treated in the same manner as the DBS-$CONHNH_2$.

Nine vials of multicomponent gels were formed with DBS-$CONHNH_2$ (3.00 mg, 0.006 mmol) in water (0.5 mL). This suspension was sonicated before sodium alginate (1%, 0.5 mL) was added. This solution was heated and allowed to cool before calcium chloride (5%, 1 mL) was added. These nine vials were treated in the same manner as the previous two sets of gels.

5.8 CuAAC Reaction

A stock solution of sodium ascorbate (1 M) was produced by adding sodium-*L*-ascorbate (198.37 mg, 1.00 mmol) to water (1 mL). The solution was stored in a sealed vessel and was replaced every two days.

A stock solution of copper sulfate (0.3 M) was produced by dissolving anhydrous copper sulfate (48.76 mg, 0.306 mmol) to water (1 mL) and sonicating for 5 minutes to ensure complete dissolution.

Copper-doped multicomponent gel beads were formed by adding DBS-$CONHNH_2$ (3.00 mg, 0.006 mmol) to water (0.5 mL) and sonicating to form a homogenous suspension. To this, sodium alginate (1%, 0.5 mL) was added. The mixture was heated and added dropwise while hot into calcium chloride (5%). These millimetre-sized beads were washed in distilled water before being added to a cupric chloride solution (0.1 M, 4 mL) and stored for 2 days. Following this, the beads were stored in distilled water until used.

Copper-doped alginate beads were formed by adding sodium alginate (1%, 1 mL) dropwise into calcium chloride (5%). These beads were washed in distilled water before being added

to a cupric chloride solution (0.1 M, 4 mL) and stored for 2 days. Following this, the beads were transferred to distilled water where they were kept until they were used.

In a set up for a control reaction, 2-azido-2-deoxy-D-glucose (20.39 mg, 0.01 mmol) and phenylacetylene (10 μL, 0.01 mmol) were added to water and *tert*-butanol (10 mL, 1:1) under stirring. Sodium ascorbate solution (1 M, 300 μL) was added, followed by copper sulfate solution (0.3 M, 100 μL). The reaction was stirred overnight without heating. TLC analysis was performed the following morning using a 1:1 mixture of hexane and ethyl acetate. The reaction mixture was diluted with water (50 mL) and cooled in an ice bath for 2 hours. The solution was then concentrated using a Rotavap rotary evaporator to afford crude product (29.01 mg, 98%).

A reaction using multicomponent gel beads was carried out by adding 2-azido-2-deoxy-D-glucose (20.22 mg, 0.01 mmol) and phenylacetylene (10 μL, 0.01 mmol) to a mixture of water and *tert*-butanol (10 mL, 1:1) under stirring. Sodium ascorbate solution (1 M, 300 μL) was added, followed by 10 millimetre-sized copper-doped multicomponent gel beads (c. 1 mL). The reaction was stirred overnight without heating. TLC analysis was performed the following morning using a 1:1 mixture of hexane and ethyl acetate. The reaction mixture was diluted with water (50 mL) and cooled in an ice bath for 2 hours. The solution was then concentrated using a Rotavap rotary evaporator to afford crude product (28.61 mg, 97%).

This reaction was repeated using copper-doped alginate gel beads in place of the multicomponent gel beads.

The effect of *tert*-butanol on the gel beads was investigated by adding 10 multicomponent gel beads to a mixture of water and *tert*-butanol (10 mL, 1:1) and stirring overnight. A second reaction vessel was set up with the same reagents but was not stirred.

For the reactions in water, 2-azido-2-deoxy-D-glucose (20.00 mg, 0.01 mmol) and phenylacetylene (10 μL, 0.01 mmol) were added to water (10 mL) under stirring. This reaction was set up in two reaction vessels. To one flask, sodium ascorbate solution (1 M, 300 μL) and copper sulfate solution (0.3 M, 100 μL) were added. To the other, sodium ascorbate solution (1 M, 300 μL) and 10 millimetre-sized copper-doped beads (c. 1 mL) were added. The reaction was allowed to stir overnight. TLC analysis was performed before the reaction mixture was diluted in water (50 mL) and cooled in an ice bath.

The effect of sodium ascorbate on the beads was investigated by stirring 10 multicomponent gel beads (c. 1 mL) in water (10 mL) and sodium ascorbate solution (1 M, 300 μL) overnight.

6. Bibliography

1. J. Fu and M. in het Panhuis, *J. Mater. Chem. B*, 2019, **7**, 1523-1525.
2. C. L. Esposito, P. Kirilov and V. G. Roullin, *J. Control. Release*, 2018, **271**, 1-20.
3. T. Linhares, M. T. P. de Amorim and L. Duraes, *J Mater Chem A*, 2019, **7**, 22768-22802.
4. H. Shah, A. B. Nair, J. Shah, P. Bharadia and B. E. Al-Dhubiab, *DARU J. Pharm. Sci.*, 2019, **27**, 59-70.
5. G. Feuillade and P. Perche, *J. Appl. Electrochem.*, 1975, **5**, 63-69.
6. S. Banerjee and S. Bhattacharya, *Crit. Rev. Food Sci. Nutr.*, 2012, **52**, 334-346.
7. J. M. Bemmelen, *Zeitschr. f. Chem. und Ind. der Kolloide*, 1907, **1**, 213-214.
8. O. Wichterle and D. LÍM, *Nature*, 1960, **185**, 117-118.
9. S. Daniele, M. F. Refojo, C. L. Schepens and H. M. Freeman, *Arch. Ophthalmol.*, 1968, **80**, 120-127.
10. K. F. Mueller and S. J. Heiber, *J. Appl. Polym. Sci*, 1982, **27**, 4043-4064.
11. K. Y. Lee and D. J. Mooney, *Prog. Polym. Sci.*, 2012, **37**, 106-126.
12. L. Fan, H. Yang, J. Yang, M. Peng and J. Hu, *Carbohydr. Polym.*, 2016, **146**, 427-434.
13. C. Shao, M. Wang, L. Meng, H. Chang, B. Wang, F. Xu, J. Yang and P. Wan, *Chem. Mater.*, 2018, **30**, 3110-3121.
14. J. A. Burdick and K. S. Anseth, *Biomaterials*, 2002, **23**, 4315-4323.
15. M. Yoshida, M. Asano, I. Kaetsu, H. Yamanaka, K. Nakai, H. Yasuda and K. Shida, *Kobunshi Ronbunshu*, 1984, **41**, 145-150.
16. J. Senior, C. Delgado, D. Fisher, C. Tilcock and G. Gregoriadis, *Biochim Biophys Acta Biomembr*, 1991, **1062**, 77-82.
17. J. S. Suk, Q. Xu, N. Kim, J. Hanes and L. M. Ensign, *Adv. Drug Deliv. Rev*, 2016, **99**, 28-51.
18. Q. Chen, H. Chen, L. Zhu and J. Zheng, *J. Mater. Chem. B*, 2015, **3**, 3654-3676.
19. X. Zhang, Z. Yin, Y. Guo, H. Huang, J. Zhou, L. Wang, J. Bai and Z. Fan, *New J. Chem*, 2020, DOI: 10.1039/D0NJ04016A.
20. A. Lipowitz, *Justus Liebigs Ann. Chem.*, 1841, **38**, 348-355.
21. P. Terech and R. G. Weiss, *Chem. Rev.*, 1997, **97**, 3133-3160.
22. L. A. Estroff and A. D. Hamilton, *Chem. Rev.*, 2004, **104**, 1201-1218.
23. J. Zhong, H. Fu, X. Jia, H. Lou, T. Wan, H. Luo, H. Liu, D. Zhong and X. Luo, *RSC Adv.*, 2019, **9**, 11824-11832.
24. J. Hoque, N. Sangaj and S. Varghese, *Macromol. Biosci.*, 2019, **19**, 1800259.
25. E. S. Gil and S. M. Hudson, *Prog. Polym. Sci.*, 2004, **29**, 1173-1222.
26. A. Friggeri, B. L. Feringa and J. van Esch, *J. Control. Release*, 2004, **97**, 241-248.
27. M. Suzuki, M. Yumoto, M. Kimura, H. Shirai and K. Hanabusa, *Chem. Eur. J.*, 2003, **9**, 348-354.
28. N. Yan, G. He, H. Zhang, L. Ding and Y. Fang, *Langmuir*, 2010, **26**, 5909-5917.
29. N. Sreenivasachary and J.-M. Lehn, *Proc. Natl. Acad. Sci. U.S.A*, 2005, **102**, 5938-5943.
30. D. J. Cosgrove, *Nat. Rev. Mol. Cell Biol*, 2005, **6**, 850-861.
31. J. S. Maciel, L. S. Chaves, B. W. S. Souza, D. I. A. Teixeira, A. L. P. Freitas, J. P. A. Feitosa and R. C. M. de Paula, *Carbohydr. Polym.*, 2008, **71**, 559-565.
32. M. Rinaudo, *Prog. Polym. Sci.*, 2006, **31**, 603-632.

33. M. Hosseinnejad and S. M. Jafari, *Int. J. Biol. Macromol.*, 2016, **85**, 467-475.
34. N. Rhein-Knudsen, M. T. Ale, F. Ajalloueian and A. S. Meyer, *Food Hydrocoll.*, 2017, **71**, 236-244.
35. J. Millis and F. B. Reed, *Biochem. J.*, 1947, **41**, 273-275.
36. H. Daemi and M. Barikani, *Sci. Iran.*, 2012, **19**, 2023-2028.
37. Y. Fang, S. Al-Assaf, G. O. Phillips, K. Nishinari, T. Funami, P. A. Williams and L. Li, *J. Phys. Chem. B*, 2007, **111**, 2456-2462.
38. I. Donati, S. Holtan, Y. A. Mørch, M. Borgogna and M. Dentini, *Biomacromolecules*, 2005, **6**, 1031-1040.
39. A. Jimenez-Escrig and F. J. Sanchez-Muniz, *Nutr. Res.*, 2000, **20**, 585-598.
40. T. Y. Lin and W. Z. Hassid, *J Biol Chem*, 1966, **241**, 5284-5297.
41. D. F. Pindar and C. Bucke, *Biochem. J.*, 1975, **152**, 617-622.
42. M. L. Torres, J. M. Fernandez, F. G. Dellatorre, A. M. Cortizo and T. G. Oberti, *Algal Res.*, 2019, **40**, 101499.
43. D. Slavin, *Nature*, 1950, **165**, 115-116.
44. M. Kierstan and C. Bucke, *Biotechnol Bioeng*, 1977, **19**, 387-397.
45. P. S. J. Cheetham, K. W. Blunt and C. Bocke, *Biotechnol. Bioeng*, 1979, **21**, 2155-2168.
46. T. Gilchrist and A. M. Martin, *Biomaterials*, 1983, **4**, 317-320.
47. A. Moroz, S. Kataev, I. Samoilenko, A. Komissarova and V. Iakubovich, *Antibiotiki*, 1981, **26**, 92-96.
48. A. A. Badwan, A. Abumalooh, E. Sallam, A. Abukalaf and O. Jawan, *Drug Dev. Ind. Pharm*, 1985, **11**, 239-256.
49. G. R. Seely and R. L. Hart, *Environ. Sci. Technol.*, 1977, **11**, 623-625.
50. Ø. Holte, E. Onsøyen, R. Myrvold and J. Karlsen, *Eur. J. Pharm. Sci*, 2003, **20**, 403-407.
51. C.-H. Niu and Y.-Y. Chiu, *J. Pharm. Sci*, 1998, **87**, 1331-1334.
52. H. Tomida, C. Nakamura, H. Yoshitomi and S. Kiryu, *Chem. Pharm. Bull.*, 1993, **41**, 2161-2165.
53. Y. Murata, N. Sasaki, E. Miyamoto and S. Kawashima, *Eur. J. Pharm. Biopharm*, 2000, **50**, 221-226.
54. K. Kaneko, K. Kanada, T. Yamada, M. Miyagi, N. Saito, T. Ozeki, H. Yuasa and Y. Kanaya, *Chem. Pharm. Bull.*, 1997, **45**, 1063-1068.
55. N. Jerry, Y. Anitha, C. P. Sharma and P. Sony, *Drug Deliv.*, 2001, **8**, 19-23.
56. I. Joseph and S. Venkataram, *Int. J. Pharm*, 1995, **126**, 161-168.
57. K. Rajpoot and S. K. Jain, *Int. J. Biol. Macromol.*, 2020, **151**, 830-844.
58. S. Mandal, A. K. Puniya and K. Singh, *Int. Dairy J.*, 2006, **16**, 1190-1195.
59. L. Corvaglia, A. Aceti, E. Mariani, M. De Giorgi, M. G. Capretti and G. Faldella, *Aliment. Pharmacol. Ther.*, 2011, **33**, 466-470.
60. J. Herrmann, E. H. Yang, C. A. Iliescu, M. Cilingiroglu, K. Charitakis, A. Hakeem, K. Toutouzas, M. A. Leesar, C. L. Grines and K. Marmagkiolis, *Circulation*, 2016, **133**, 1272-1289.
61. I. Kola and J. Landis, *Nat. Rev. Drug Discov.*, 2004, **3**, 711-716.
62. Y. Matsumura and H. Maeda, *Cancer Res*, 1986, **46**, 6387-6392.
63. A. Noguchi, T. Takahashi, T. Yamaguchi, K. Kitamura, A. Noguchi, H. Tsurumi, K.-i. Takashina and H. Maeda, *Jpn J. Cancer Res*, 1992, **83**, 240-243.
64. J. W. Nichols and Y. H. Bae, *J. Control. Release*, 2014, **190**, 451-464.

65. M. Najlah, A. Said Suliman, I. Tolaymat, S. Kurusamy, V. Kannappan, A. M. A. Elhissi and W. Wang, *Pharmaceutics*, 2019, **11**, 610.
66. A. Paavola, I. Kilpeläinen, J. Yliruusi and P. Rosenberg, *Int. J. Pharm*, 2000, **199**, 85-93.
67. J.-H. Cui, J.-S. Goh, P.-H. Kim, S.-H. Choi and B.-J. Lee, *Int. J. Pharm*, 2000, **210**, 51-59.
68. M. Rajaonarivony, C. Vauthier, G. Couarraze, F. Puisieux and P. Couvreur, *J. Pharm. Sci*, 1993, **82**, 912-917.
69. S. De and D. Robinson, *J. Control. Release*, 2003, **89**, 101-112.
70. A. Zahoor, S. Sharma and G. K. Khuller, *Int. J. Antimicrob. Agents*, 2005, **26**, 298-303.
71. H. Zhang, E. Tumarkin, R. M. A. Sullan, G. C. Walker and E. Kumacheva, *Macromol. Rapid Commun*, 2007, **28**, 527-538.
72. P. Lertsutthiwong, K. Noomun, N. Jongaroonngamsang, P. Rojsitthisak and U. Nimmannit, *Carbohydr. Polym.*, 2008, **74**, 209-214.
73. Y. Chen, X. Lin, H. Park and R. Greever, *Nanomedicine*, 2009, **5**, 316-322.
74. J. Guo, J. Jiang, X. Gu, X. Li and T. Liu, *Colloids Surf. A Physiochem Eng Asp*, 2021, **608**, 125548.
75. Y.-M. Yi, T.-Y. Yang and W.-M. Pan, *World J. Gastroenterol.*, 1999, **5**, 57-60.
76. A. H. E. Machado, D. Lundberg, A. J. Ribeiro, F. J. Veiga, B. Lindman, M. G. Miguel and U. Olsson, *Langmuir*, 2012, **28**, 4131-4141.
77. J.-O. You, Y.-C. Liu and C.-A. Peng, *Int. J. Nanomed.*, 2006, **1**, 173-180.
78. T. Wang, Z. Feng, N. He, Z. Wang, S. Li, Y. Guo and L. Xu, *J. Nanosci. Nanotechnol.*, 2007, **7**, 4571-4574.
79. J.-O. You and C.-A. Peng, *Macromol. Symp.*, 2005, **219**, 147-153.
80. S. Wilhelm, A. J. Tavares, Q. Dai, S. Ohta, J. Audet, H. F. Dvorak and W. C. W. Chan, *Nat. Rev. Mater.*, 2016, **1**, 16014.
81. D. E. Owens and N. A. Peppas, *Int. J. Pharm*, 2006, **307**, 93-102.
82. N. Sahatsapan, T. Ngawhirunpat, T. Rojanarata, P. Opanasopit and P. Patrojanasophon, *AAPS PharmSciTech*, 2020, **21**, 212.
83. R. R. Arvizo, O. R. Miranda, D. F. Moyano, C. A. Walden, K. Giri, R. Bhattacharya, J. D. Robertson, V. M. Rotello, J. M. Reid and P. Mukherjee, *PLoS One*, 2011, **6**, e24374.
84. M. G. V. Heiden, L. C. Cantley and C. B. Thompson, *Science*, 2009, **324**, 1029-1033.
85. K. Na, E. Seong Lee and Y. H. Bae, *J. Control. Release*, 2003, **87**, 3-13.
86. T. Neuberger, B. Schöpf, H. Hofmann, M. Hofmann and B. von Rechenberg, *J. Magn. Magn. Mater.*, 2005, **293**, 483-496.
87. R. J. Griffitt, J. Luo, J. Gao, J.-C. Bonzongo and D. S. Barber, *Environ. Toxicol. Chem.*, 2008, **27**, 1972-1978.
88. E. Hee Kim, H. Sook Lee, B. Kook Kwak and B.-K. Kim, *J. Magn. Magn. Mater.*, 2005, **289**, 328-330.
89. H. Jin and K. A. Kang, *Adv Exp Med Biol*, 2007, **599**, 45-52.
90. M. Johannsen, U. Gneveckow, L. Eckelt, A. Feussner, N. WaldÖFner, R. Scholz, S. Deger, P. Wust, S. A. Loening and A. Jordan, *Int. J. Hyperth.*, 2005, **21**, 637-647.
91. S.-H. Liao, C.-H. Liu, B. P. Bastakoti, N. Suzuki, Y. Chang, Y. Yamauchi, F.-H. Lin and K. C. W. Wu, *Int. J. Nanomed.*, 2015, **10**, 3315-3327.

92. M. Ramazanov, A. Karimova and H. Shirinova, *Biointerface Res. Appl. Chem.*, 2021, **11**, 8654-8668.
93. Q. A. Pankhurst, J. Connolly, S. K. Jones and J. Dobson, *J. Phys. D: Appl. Phys.*, 2003, **36**, R167-R181.
94. M. Nerantzaki, A. Michel, E. Briot, J. M. Siaugue, C. Ménager, C. Wilhelm and N. Griffete, *ChemComm*, 2020, **56**, 10255-10258.
95. K. A. Court, H. Hatakeyama, S. Y. Wu, M. S. Lingegowda, C. Rodríguez-Aguayo, G. López-Berestein, L. Ju-Seog, C. Rinaldi, E. J. Juan, A. K. Sood and M. Torres-Lugo, *Mol. Cancer Ther.*, 2017, **16**, 966.
96. M. M. Gottesman, T. Fojo and S. E. Bates, *Nat. Rev. Cancer.*, 2002, **2**, 48-58.
97. S. Mancarella, V. Greco, F. Baldassarre, D. Vergara, M. Maffia and S. Leporatti, *Macromol. Biosci.*, 2015, **15**, 1365-1374.
98. W. Song, X. Su, D. A. Gregory, W. Li, Z. Cai and X. Zhao, *Nanomaterials (Basel)*, 2018, **8**.
99. C. Gianni, R. Vittoria, O. Yosuke, M. Arianna, D. Paolo and T. Shinji, *Curr. Nanosci.*, 2008, **4**, 212-218.
100. T. Chen, Q. P. Yan, F. R. Li and S. Q. Tang, *Adv Mat Res*, 2012, **535-537**, 2381-2384.
101. E. E. Connor, J. Mwamuka, A. Gole, C. J. Murphy and M. D. Wyatt, *Small*, 2005, **1**, 325-327.
102. A. Radomski, P. Jurasz, D. Alonso-Escolano, M. Drews, M. Morandi, T. Malinski and M. W. Radomski, *Br. J. Pharmacol.*, 2005, **146**, 882-893.
103. E. Pawelczyk, A. S. Arbab, A. Chaudhry, A. Balakumaran, P. G. Robey and J. A. Frank, *STEM CELLS*, 2008, **26**, 1366-1375.
104. L. Yang, H. Kuang, W. Zhang, Z. P. Aguilar, Y. Xiong, W. Lai, H. Xu and H. Wei, *Nanoscale*, 2015, **7**, 625-636.
105. M. J. Meunier, *Ann. Chim. Phys.*, 1891, **22**, 412.
106. R. L. Mahaffey Jr, *US Patent, US4371645A*, 1981.
107. J. K. Wolfe, R. M. Hann and C. S. Hudson, *J. Am. Chem. Soc*, 1942, **64**, 1493-1497.
108. S. J. Angyal and J. V. Lawler, *J. Am. Chem. Soc*, 1944, **66**, 837-838.
109. R. Feng, L. Chen, Z. Hou and J. Song, *Trans. Tianjin Univ.*, 2007, **13**, 35-41.
110. S. Raluca, S. Rosca, C. Ott, S. Roşca, E. Perez, I. Rico-Lattes and A. Lattes, *Rev Roum Chim*, 2006, **51**.
111. J. Li, K. Fan, X. Guan, Y. Yu and J. Song, *Langmuir*, 2014, **30**, 13422-13429.
112. D. J. Cornwell, B. O. Okesola and D. K. Smith, *Soft Matter*, 2013, **9**, 8730-8736.
113. B. O. Okesola and D. K. Smith, *ChemComm*, 2013, **49**, 11164-11166.
114. F. Rodríguez-Llansola, B. Escuder, J. F. Miravet, D. Hermida-Merino, I. W. Hamley, C. J. Cardin and W. Hayes, *ChemComm*, 2010, **46**, 7960-7962.
115. P. Slavík, D. W. Kurka and D. K. Smith, *Chem. Sci.*, 2018, **9**, 8673-8681.
116. P. Slavik and D. K. Smith, *Tetrahedron*, 2020, **76**, 131344.
117. V. M. P. Vieira, A. C. Lima, M. de Jong and D. K. Smith, *Chem. Eur. J.*, 2018, **24**, 15112-15118.
118. S. J. Beckers, S. Parkinson, E. Wheeldon and D. K. Smith, *ChemComm*, 2019, **55**, 1947-1950.
119. E. J. Howe, B. O. Okesola and D. K. Smith, *ChemComm*, 2015, **51**, 7451-7454.
120. N. Bhala, J. Emberson, A. Merhi, S. Abramson, N. Arber, J. A. Baron, C. Bombardier, C. Cannon, M. E. Farkouh, G. A. FitzGerald, P. Goss,

H. Halls, E. Hawk, C. Hawkey, C. Hennekens, M. Hochberg, L. E. Holland, P. M. Kearney, L. Laine, A. Lanas, P. Lance, A. Laupacis, J. Oates, C. Patrono, T. J. Schnitzer, S. Solomon, P. Tugwell, K. Wilson, J. Wittes and C. Baigent, *Lancet*, 2013, **382**, 769-779.

121. P. R. A. Chivers and D. K. Smith, *Chem. Sci.*, 2017, **8**, 7218-7227.
122. S. Lin-Gibson, S. Bencherif, J. A. Cooper, S. J. Wetzel, J. M. Antonucci, B. M. Vogel, F. Horkay and N. R. Washburn, *Biomacromolecules*, 2004, **5**, 1280-1287.
123. C. C. Piras, P. Slavik and D. K. Smith, *Angew. Chem. Int. Ed.*, 2020, **59**, 853-859.
124. C. C. Piras, C. S. Mahon and D. K. Smith, *Chem. Eur. J.*, 2020, **26**, 8452-8457.
125. K. Petcharoen and A. Sirivat, *Mater. Sci. Eng. B*, 2012, **177**, 421-427.
126. H. Namduri and S. Nasrazadani, *Corros. Sci.*, 2008, **50**, 2493-2497.
127. B. Ajitha, Y. A. Kumar Reddy, P. S. Reddy, H.-J. Jeon and C. W. Ahn, *RSC Adv.*, 2016, **6**, 36171-36179.
128. G. Karunakaran, E.-B. Cho, G. S. Kumar, E. Kolesnikov, D. Y. Karpenkov, J. Gopinathan, M. M. Pillai, R. Selvakumar, S. Boobalan and M. V. Gorshenkov, *Ceram. Int.*, 2019, **45**, 15143-15155.
129. J. Tang, M. Myers, K. A. Bosnick and L. E. Brus, *J. Phys. Chem. B*, 2003, **107**, 7501-7506.
130. D. Liu, A. Mori and L. Huang, *Biochim Biophys Acta*, 1992, **1104**, 95-101.
131. B. Bhowmik, B. Sa and A. Mukherjee, *Acta Pharm.*, 2006, **56**, 417-429.
132. V. Rocher, J.-M. Siaugue, V. Cabuil and A. Bee, *Water Res.*, 2008, **42**, 1290-1298.
133. A. G. Shard, *Surf. Interface Anal*, 2014, **46**, 175-185.
134. N. Usha, B. Viswanathan, V. R. K. Murthy and J. Sobhanadri, *Spectrochim. Acta A*, 1997, **53**, 1761-1765.
135. T. Radu, C. Iacovita, D. Benea and R. Turcu, *Appl. Surf. Sci.*, 2017, **405**, 337-343.
136. X. Zhou, B. Brzostowski, A. Durajski, M. Liu, J. Xiang, T. Jiang, Z. Wang, S. Chen, P. Li, Z. Zhong, A. Drzewiński, M. Jarosik, R. Szczęśniak, T. Lai, D. Guo and D. Zhong, *J. Phys. Chem. C*, 2020, **124**, 9416-9423.
137. S. Shrestha and S. Maharjan, *J. Nepal Chem. Soc.*, 2013, **29**, 11-17.
138. R. G. Micetich, S. N. Maiti, P. Spevak, T. W. Hall, S. Yamabe, N. Ishida, M. Tanaka, T. Yamazaki, A. Nakai and K. Ogawa, *J. Med. Chem.*, 1987, **30**, 1469-1474.
139. F. Himo, T. Lovell, R. Hilgraf, V. V. Rostovtsev, L. Noodleman, K. B. Sharpless and V. V. Fokin, *J. Am. Chem. Soc*, 2005, **127**, 210-216.

7. Appendices

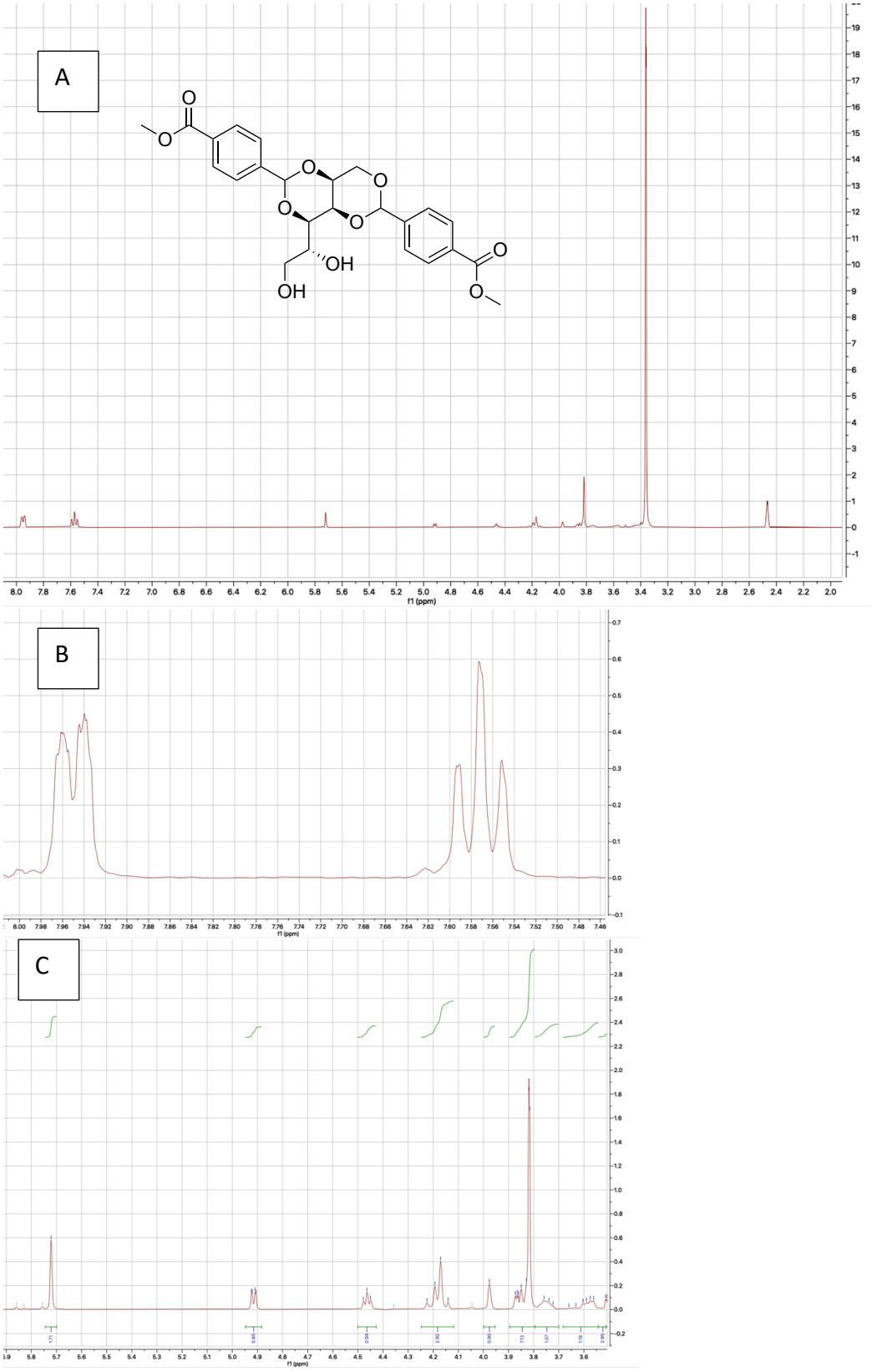

Appendix 1: Proton NMR spectrum of DBS-CO_2Me. 'A' shows the full spectrum, 'B' shows a close-up of the aromatic region, and 'C' depicts the complex sugar backbone region.

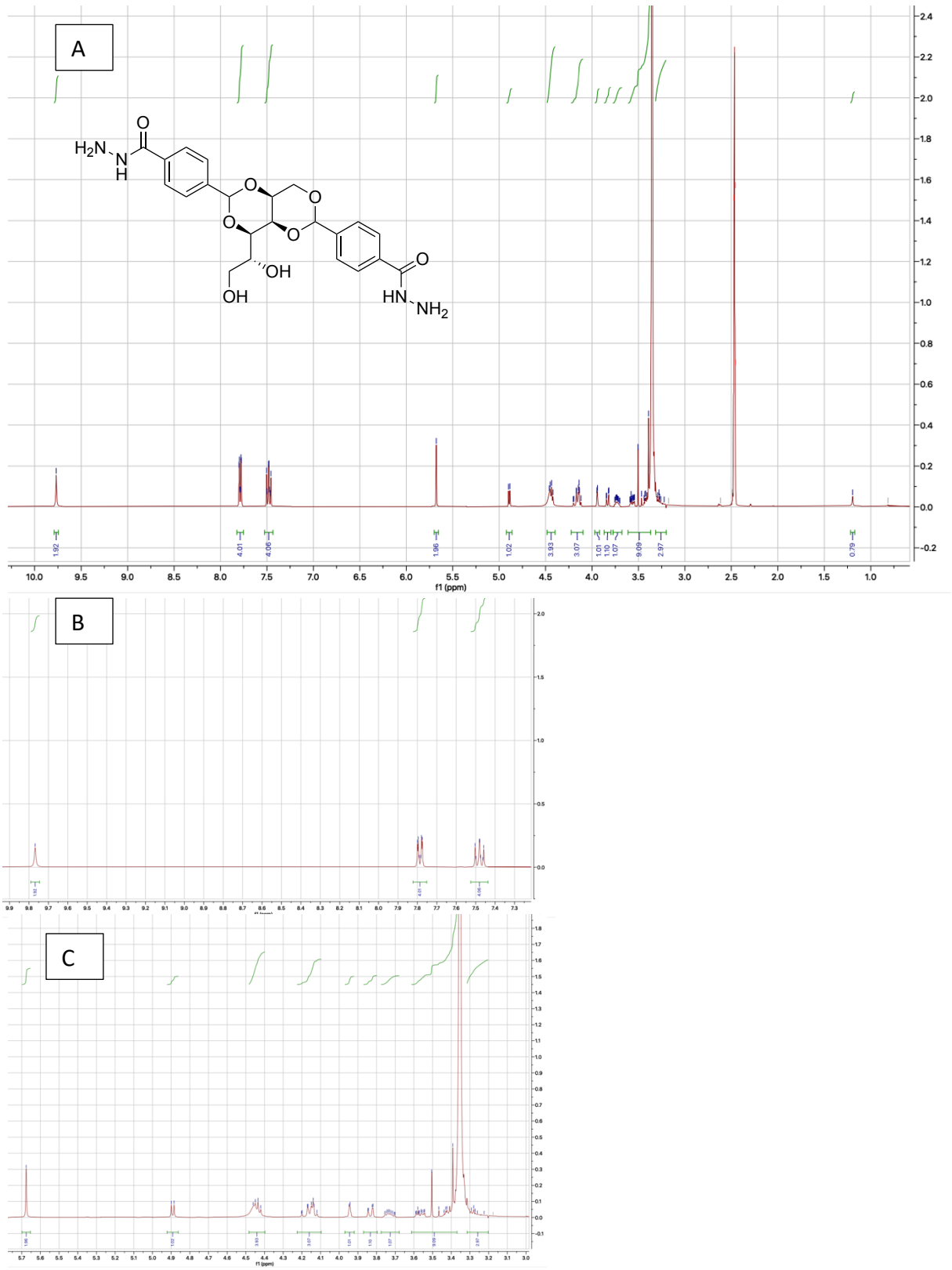

Appendix 2: Proton NMR spectrum of DBS-CONHNH$_2$. 'A' depicts the entire spectrum, while 'B' depicts the aromatic and amine region, and 'C' depicts the complex sugar backbone region.